Научном већу
Института за физику
Београд

Предмет:
Покретање поступка за реизбор у звање истраживач сарадник

МОЛБА

Молим Научно веће Института за физику да покрене поступак за мој реизбор у звање истраживач сарадник.

У прилогу достављам:

1. Мишљење руководиоца пројекта;

2. Кратку стручну биографију;

3. Кратак преглед научне активности;

4. Списак објављених радова и других публикација;

5. Копије објављених радова и других публикација;

6. Уверење о последњем овереном и уписаном семестру на докторским студијама;

7. Одлуку Већа научних области природно-математичких наука Универзитета у Београду о прихватању предлога теме докторске дисертације.

У Београду
15. 05. 2019. г.

С поштовањем,

Владимир Вељић

Научном већу Института за физику у Београду

Београд, 15. мај 2019. године

Предмет: **Мишљење руководиоца пројекта о реизбору Владимира Вељића у звање истраживач сарадник**

Владимир Вељић је запослен у Лабораторији за примену рачунара у науци, у оквиру Центра изузетних вредности за изучавање комплексних система Института за физику у Београду и ангажован је на пројекту основних истраживања Министарства просвете, науке и технолошког развоја Републике Србије ОН171017, под називом "Моделирање и нумеричке симулације сложених вишечестичних физичких система". На поменутом пројекту ради на темама из физике ултрахладних диполних фермионских гасова под руководством др Антуна Балажа. С обзиром да испуњава све предвиђене услове у складу са Правилником о поступку, начину вредновања и квантитативном исказивању научноистраживачких резултата истраживача МПНТР, сагласан сам са покретањем поступка за реизбор Владимира Вељића у звање истраживач сарадник.

За састав комисије за реизбор Владимира Вељића у звање истраживач сарадник предлажем:

(1) др Антун Балаж, научни саветник, Институт за физику у Београду
(2) др Ивана Васић, виши научни сарадник, Институт за физику у Београду
(3) академик Милан Дамњановић, редовни професор Физичког факултета Универзитета у Београду

Руководилац пројекта

др Антун Балаж
научни саветник

Биографија Владимира Вељића

Владимир Вељић рођен је 30. 12. 1987. године у Брусу. Основну школу "Јован Јовановић Змај" завршио је у Брусу као ђак генерације. Гимназију "9. мај" у Нишу, одељење специјализовано за физику, такође је завршио као ђак генерације. Основне студије на Универзитету у Београду похађао је паралелно на Физичком факултету на смеру Теоријска и експериментална физика у периоду од 2007. до 2011. године и на Машинском факултету у периоду од 2007. до 2010. године. На Физичком факултету дипломирао је као студент генерације са просечном оценом 9,90, а на Машинском факултету је дипломирао са просечном оценом 9,97. Мастер студије на Машинском факултету похађао је у периоду од 2010. до 2012. године и завршио са просечном оценом 9,90, док је мастер студије на Физичком факултету похађао у периоду од 2011. до 2012. године и завршио са просечном оценом 10,00.

Током студија боравио је на двомесечним студентским праксама у ЦЕРН-у, током лета 2011. године, и у Кларендон лабораторији на Оксфорду, током лета 2012. године. Школске 2008/2009 године Владимир Вељић је био стипендиста Српског пословног клуба Привредник, а од 2009. до 2012. године био је стипендиста Фонда за младе таленте Републике Србије.

Студент је докторских студија на Физичком факултету Универзитета у Београду, а његова ужа научна област је физика кондензоване материје и статистичка физика. Израда докторске тезе под насловом Quantum kinetic theory for ultracold dipolar fermi gases (Квантна кинетичка теорија за ултрахладне диполне Ферми гасове) одобрена је, а за ментора тезе именован је др Антун Балаж.

Владимир Вељић је запослен у Институту за физику у Београду као истраживач сарадник у Лабораторији за примену рачунара у науци, у оквиру Националног центра изузетних вредности за изучавање комплексних система. Поред пројекта основних истраживања ОН171017 којим руководи др Антун Балаж, учествује и на билатералном пројекту QDDB са Немачком. До сада је похађао више школа за докторанте, нпр. Anyon Physics of Ultracold Atomic Gases - Freie Universität Berlin (2013), International Conference on Atomic Physics Summer School -The College of William and Mary (2014), International School Probing Macrosopic Quantum Phenomena-Königstein (2014), Cold-Atoms PreDoc School Exploring new quantum gases - Les Houches (2015), Okinawa School in Physics: Coherent Quantum Dynamics - Okinawa (2015).

У току школске 2012/13. године, као и током школске 2015/16 и 2016/17. године, учествује у раду Државне комисије за такмичења ученика средњих школа из физике као аутор задатака на свим нивоима такмичења, а од 2017. један је од и организатора Турнира младих физичара, новог формата средњошколског такмичења у Србији. Био је један од вођа тима Србије на Интеранциналном турниру младих физичара два пута, у Сингапуру у јулу 2017. године, и у Кини у јулу 2018. године.

До сада, Владимир Вељић има 16 саопштења са међународних скупова штампаних у изводу (М34) и 2 рада објављена у врхунским међународним часописима (М21).

Кратак преглед научне активности Владимира Вељића

Владимир Вељић је започео свој истраживачки рад 2013. године на Институту за физику Београд у Лабораторији за примену рачунара у науци, под менторством др Антуна Балажа. У свом научном раду бави се темама везаним за ултра хладне квантне гасове са диполном интеракцијом.

Из теоријског, односно аналитичког и нумеричког угла, особине ултрахладних диполних Ферми гасова могу да се проучавају користећи неколико приступа, од којих сваки има одређени број предности и мана. У свом научном раду Владимир развија и уопштава квантну кинетичку теорију (односно постојећи Болцман-Власов формализам), за коју је раније показано да успешно описује основне карактеристике реалне динамике Ферми гасова са јаком диполном интеракцијом. Поред тога, овај приступ је успешно коришћен за теоријски опис деформације Ферми површи која је експериментално измерена за фермионски гас. Ова теорија била је развијена и могла да се примени само у у случају када су диполи оријентисани дуж једне од оса замке и то у два посебна гранична сударна режима: у режиму када су судари између атома занемарљиви и када се систем налази у хидродинамичком режиму, у којем су судари доминантни. Владимир Вељић је ту постојећу теорију током свог досадашњег научно-истраживачког рада проширио у више различитих праваца.

У првој фази истраживања Владимир Вељић је проширио постојећу теорију примењујући апроксимацију релаксационог времена која омогућава да се систем опише у различитим сударним режимима, односно у свим режимима између два претходно поменута гранична случаја. Такође, релаксационо време је моделирано на самоусаглашен начин, за разлику од претходних радова где је оно третирано као феноменолошки параметар. Важно је истаћи да је поређење теоријских предвиђања са мерењима базираним на времену лета (time-of-flight) омогућава проверу таквог модела.

У експерименту са ербијумовим атомима је примећено да деформација Ферми сфере прати промену правца спољашњег магнетног поља, односно да се Ферми сфера увек издужује у правцу атомских диполних момената, који се оријентишу у правцу спољашњег магнетног поља. У другој фази истраживања, са аналитичке стране, раније развијена квантна кинетичка теорија је уопштена тако да може да опише било коју геометрију система, односно произвољну оријентацију дипола, што је посебно од значаја за интерпретацију експерименталних резултата. Полазна тачка овог рачуна је облик Вигнерове функције којом се систем описује у глобалној равнотежи, док је гас заробљен у замци. С обзиром на то да је теорија развијена за ултрахладне квантне гасове ($T = 0\,\mathrm{K}$), претпоставка је да се Вигнерова функција може добро описати Хевисајдовом степ функцијом, која за аргумент има збир елипсоида у реалном простору и елипсоида у моментном простору, при чему главна оса овог елипсоида има правац дипола.

I. Списак објављених радова и других публикација

У овој секцији представљен је списак објављених радова и других публикација по важећој категоризацији Министарства просвете, науке и технолошког развоја:

- **Радови објављени у врхунским међународним часописима (M21):**

1. **V. Veljić**, A. R. P. Lima, S. Baier, M. J. Mark, L. Chomaz, F. Ferlaino, A. Pelster, and A. Balaž, *Ground state of an ultracold Fermi gas of tilted dipoles in elongated traps*,
New J. Phys. **20**, 093016 (2018)
2. **V. Veljić**, A. Balaž, and A. Pelster, *Time-of-flight expansion of trapped dipolar Fermi gases: From the collisionless to the hydrodynamic regime*,
Phys. Rev. A **95**, 053635 (2017)

- **Саопштења са међународног скупа штампана у изводу (M34):**

1. **V. Veljić**, A. Pelster, and A. Balaž, *Degenerate Fermi gases of polar molecules with tilted dipoles*, DPG Spring Meeting, 10 - 15 March 2019, Rostock, Germany
2. **V. Veljić**, A. Pelster, and A. Balaž, *Stability diagram of degenerate Fermi gases of polar molecules with tilted dipoles*, Research Frontiers in Ultracold Qunatum Gases, 17 - 21 December 2018, Bad Honnef, Germany
3. **V. Veljić**, A. P. R. Lima, L. Chomaz, S. Baier, M. J. Mark, F. Ferlaino, A. Pelster, A. Balaž, *Ground state of an ultracold Fermi gas of tilted dipoles* SuperFluctuations 2018 - Fluctuations and Highly Nonlinear Phenomena in Superfluids and Superconductors, 5 - 7 September 2018, San Benedetto del Tronto, Italy
4. **V. Veljić**, A. R. P. Lima, S. Baier, L. Chomaz, F. Ferlaino, A. Pelster, and A. Balaž, *Ground State of a Fermi Gas with Tilted Dipoles*, 5th International Workshop on long-range interactions in the ultracold, 25 - 28 June 2018, Hannover, Germany
5. A. Balaž, **V. Veljić**, A. R. P. Lima, S. Baier, L. Chomaz, F. Ferlaino, and A. Pelster, *Ground State of a Fermi Gas with Tilted Dipoles*, 49th Annual DAMOP Meeting, 28 May – 1 June 2018, Ft. Lauderdale, Florida, USA,
6. **V. Veljić**, A. R. P. Lima, S. Baier, L. Chomaz, F. Ferlaino, A. Pelster, and A. Balaž, *Ground State of a Fermi Gas with Tilted Dipoles*, DPG Spring Meeting, 4 - 9 March 2018, Erlangen, Germany
7. **V. Veljić**, A.R.P.Lima, A. Balaž, and A. Pelster, *Ground State of a Fermi Gas with Tilted Dipoles*, 651. WE-Heraeus-Seminar: Longrange interactions, 22 - 25 October 2017, Bad Honnef, Germany
8. **V. Veljić**, A. Balaž, and A. Pelster, *Deformation of the Fermi Surface*, The 6th International School and Conference on Photonics, 28 August - 1 September 2017, Belgrade, Serbia
9. **V. Veljić**, A. Balaž, and A. Pelster, *Fermi Surface Deformation in Dipolar Fermi Gases*, DPG Spring Meeting, 6 - 10 March 2017, Mainz, Germany

10. **V. Veljić**, A. Balaž, and A. Pelster, *Cloud Shape of Dipolar Fermi Gases*, Ultracold Quantum Gases - Current Trends and Future Perspectives, 9 - 13 May 2016, Bad Honnef, Germany
11. **V. Veljić**, A. Balaž, A. R. P. Lima, and A. Pelster, *Cloud Shape of Dipolar Fermi Gases*, DPG Spring Meeting, 29 February 2016 - 4 March 2016, Hannover, Germany
12. **V. Veljić**, A. Balaž, and A. Pelster, *Dynamics of Trapped Dipolar Fermi Gases: From Collisionless to Hydrodynamic Regime*, DPG Spring Meeting, 29 February - 4 March 2016, Hannover, Germany
13. **V. Veljić**, A. Balaž, and A. Pelster, *Collective Modes of Dipolar Fermi Gas from Collisionless to Hydrodynamic Regime*, The 19th Symposium on Condensed Matter Physics, 7 - 11 September 2015, Belgrade, Serbia
14. **V. Veljić**, A. Balaž, and A. Pelster, *Quench Dynamics for Trapped Dipolar Fermi Gases*, The 5th International School and Conference on Photonics, 24 - 28 August 2015, Belgrade, Serbia
15. **V. Veljić**, A. Balaž, and A. Pelster, *Time-of-Flight Expansion for Trapped Dipolar Fermi Gases: From Collisionless to Hydrodynamic Regime*, DPG Spring Meeting, 23 - 27 March 2015, Heidelberg, Germany
16. **V. Veljić**, A. Balaž, and A. Pelster, *ZNG-Theory for Dipolar Quantum Gases*, The 24th International Conference on Atomic Physics, 3 - 8 August 2014, Washington, USA

PAPER • OPEN ACCESS

Ground state of an ultracold Fermi gas of tilted dipoles in elongated traps

New Journal of Physics
The open access journal at the forefront of physics

Deutsche Physikalische Gesellschaft DPG
IOP Institute of Physics

Published in partnership with: Deutsche Physikalische Gesellschaft and the Institute of Physics

OPEN ACCESS

RECEIVED
13 June 2018

REVISED
27 July 2018

ACCEPTED FOR PUBLICATION
31 August 2018

PUBLISHED
13 September 2018

PAPER

Ground state of an ultracold Fermi gas of tilted dipoles in elongated traps

Vladimir Veljić[1], Aristeu R P Lima[2], Lauriane Chomaz[3], Simon Baier[3], Manfred J Mark[3,4], Francesca Ferlaino[3,4], Axel Pelster[5] and Antun Balaž[1]

[1] Scientific Computing Laboratory, Center for the Study of Complex Systems, Institute of Physics Belgrade, University of Belgrade, Serbia
[2] Universidade da Integração Internacional da Lusofonia Afro-Brasileira, Campus das Auroras, Acarape-Ceará, Brazil
[3] Institute for Experimental Physics, University of Innsbruck, Innsbruck, Austria
[4] Institute for Quantum Optics and Quantum Information, Austrian Academy of Sciences, Innsbruck, Austria
[5] Physics Department and Research Center OPTIMAS, Technische Universität Kaiserslautern, Germany

E-mail: vladimir.veljic@ipb.ac.rs

Keywords: Fermi surface, dipole–dipole interaction, ultracold quantum gases, fermions

Abstract

Many-body dipolar effects in Fermi gases are quite subtle as they energetically compete with the large kinetic energy at and below the Fermi surface (FS). Recently it was experimentally observed in a sample of erbium atoms that its FS is deformed from a sphere to an ellipsoid due to the presence of the anisotropic and long-range dipole–dipole interaction Aikawa *et al* (2014 *Science* **345** 1484). Moreover, it was suggested that, when the dipoles are rotated by means of an external field, the FS follows their rotation, thereby keeping the major axis of the momentum-space ellipsoid parallel to the dipoles. Here we generalise a previous Hartree–Fock mean-field theory to systems confined in an elongated triaxial trap with an arbitrary orientation of the dipoles relative to the trap. With this we study for the first time the effects of the dipoles' arbitrary orientation on the ground-state properties of the system. Furthermore, taking into account the geometry of the system, we show how the ellipsoidal FS deformation can be reconstructed, assuming ballistic expansion, from the experimentally measurable real-space aspect ratio after a free expansion. We compare our theoretical results with new experimental data measured with erbium Fermi gas for various trap parameters and dipole orientations. The observed remarkable agreement demonstrates the ability of our model to capture the full angular dependence of the FS deformation. Moreover, for systems with even higher dipole moment, our theory predicts an additional unexpected effect: the FS does not simply follow rigidly the orientation of the dipoles, but softens showing a change in the aspect ratio depending on the dipoles' orientation relative to the trap geometry, as well as on the trap anisotropy itself. Our theory provides the basis for understanding and interpreting phenomena in which the investigated physics depends on the underlying structure of the FS, such as fermionic pairing and superfluidity.

1. Introduction

Since the first experimental realisation of a dipolar Bose–Einstein condensate (BEC) of chromium atoms [1] and the subsequent demonstration of the presence of the anisotropic and long-range dipole–dipole interaction (DDI) in the laboratory [2], dipolar quantum gases have developed into a vast and fast-growing research field. Indeed, the interplay of the DDI and the isotropic and short-range contact interaction between the particles in these systems makes them particularly intriguing from both the experimental and the theoretical point of view [3–5].

More recently, BECs of even more magnetic species, i.e., dysprosium ($m = 10\mu_B$) [6] and erbium ($m = 7\mu_B$) [7] have been created. Here, μ_B denotes the Bohr magneton. Such species exhibit fascinating phenomena, such as the Rosensweig instability [8], the emergence of quantum-stabilised droplets [9–11] and roton quasiparticles [12]. Correspondingly, all these developments triggered much theoretical work, including,

but not limited to, the numerical effort to simulate dipolar quantum gases in fully anisotropic traps [13–17], the roton instability in pancake-shaped condensates [18–20], the investigation of beyond-mean-field effects in one-component [21, 22] and two-component [23] gases, the formation of the previously observed droplets [24–26], their ground-state properties and elementary excitations [27–29], the role of three-body interactions [30], and the self-bounded nature of the droplets [26].

In parallel, quantum-degenerate dipolar Fermi gases of dysprosium [31], erbium [32] and chromium [33] became also available in experiments. Remarkably, identical fermions of dipolar character do interact even in the low-energy limit because of the peculiar form of dipolar scattering [34]. Few-body scattering experiments have indeed confirmed universal scaling in dipolar scattering among fermions [32, 35, 36]. Many-body dipolar effects in Fermi gases are much more subtle to observe because of the competition with the large kinetic energy stored in the Fermi sphere, which leads to the Fermi pressure. Recently, the key observation of the Fermi surface (FS) deformation was made [37], confirming previous theoretical predictions [38].

It is well known that in the case of a single-component Fermi gas, the isotropic and short-range contact interaction is suppressed by the Pauli exclusion principle. Also, we know that the FS is a sphere, as a consequence of the symmetry of the Pauli pressure. Theoretical predictions which take the DDI into account, however, have shown that the antisymmetry of the wave function leads to the deformation of the FS into an ellipsoid [38]. The ground-state [39, 40] and the dynamic properties of such systems have been systematically investigated theoretically and numerically in the collisionless regime [41–43], in the hydrodynamic regime [44, 45], as well as in the whole collisional range from one limiting case to the other [46, 47]. The FS deformation was also recently theoretically studied in mixtures of dipolar and non-dipolar fermions [48], as well as in the presence of a weak lattice confinement [49].

Within the Hartree–Fock mean-field theory for a many-body system, the interaction energy of the system is expressed by means of the Hartree direct term, which gives rise to a deformation of the atomic cloud in real space [50], and the Fock exchange term, which leads to a deformation of the FS in momentum space [38]. The Hartree–Fock mean-field approximation, which includes energy terms up to first-order in the DDI, is sufficiently accurate to qualitatively explain and quantitatively describe results of ongoing experiments. However, up to now, existing theories are limited to a fixed orientation of the dipoles, which has to coincide with one of the trap axes [38, 46, 47, 50]. Such a restriction greatly simplified theoretical considerations, but, on the other hand, limited their scope since the anisotropy of the DDI is best controlled by the dipoles' orientation with respect to the trap axes.

Motivated by this, we develop a general theory to describe the ground state of a dipolar Fermi gas for an arbitrary orientation of the dipoles and trap geometry. Our full theoretical description provides a substantial advance in understanding dipolar phenomena and in describing experimental observations in a very broad parameter range, see e.g. [37]. Our theory captures both the cloud shape in real space and the FS in momentum space. To test our theory, we have performed new measurements of the FS deformation in an erbium Fermi gas for various traps and dipole orientations. The comparison between the theory and the experiment shows a remarkable agreement, demonstrating the predictive power of our newly developed theory to calculate the system's behaviour. Moreover, whereas in the Er case the deformed FS rigidly rotates with the dipole orientation, our theory also predicts a softening of the FS in systems with larger DDI. There the degree of deformation also changes depending on the dipoles' orientation.

The approach presented here is very general and can be applied to both fermionic atoms and molecules with electric [51–54] or magnetic [55] dipole moments, and any triaxial trap geometry. Our calculation provides a starting point to address more complex dipolar phenomena. Indeed, many physical properties depend on the shape of the FS and on its deformation, as the FS is directly connected to the density distribution in momentum space. For instance, one can revisit a pairing problem within a one-component dipolar Fermi gas, where in a previous work by Baranov *et al* [56] it was assumed that the FS is spherically symmetric. A relevant question for future investigations is whether one can instead have both a deformation of the Fermi sphere and a pairing of fermions at the same time, and if a critical deformation exists for which the pairing mechanism breaks down.

The paper is structured as follows. In section 2 we introduce our theoretical model and several suitable ansätze for the form of the system's Wigner function. Considering the Hartree–Fock total energy of the system, we identify the ansatz that yields minimal energy for the ground state and use it for all further calculations. In section 3 we present the generalised theory and our main results for the FS deformation and real-space magnetostriction. In particular, we discuss the behaviour of the variational parameters and their impact upon the Hartree–Fock total energy for the considered system. We also study in detail the ground-state properties for an arbitrary orientation of the dipoles, as well as for different parameters of the system, e.g., trap frequencies, number of particles, and dipolar species. Afterwards, in section 4 we directly compare our theoretical predictions with the novel experimental data. Finally, section 5 gathers our concluding remarks and gives an outlook for future research.

2. Theoretical model

We consider an ultracold quantum-degenerate dipolar gas at zero temperature consisting of N identical spin-polarised fermions of mass M. The fermions have a strong dipolar character, arising from either a large magnetic or an electric dipole moment $\mathbf{m}$. Moreover, as is usual in the experiments, we assume that all dipoles are polarised along a single direction, as their orientation can be controlled by an external field, see, e.g., [10, 37, 53, 57]. To account for the influence of the dipoles' orientation, we will consider the most general possible orientation of an external field, as depicted in figure 1, where, e.g., the magnetic field $\mathbf{B} = B\mathbf{e}$ is oriented along the unit vector $\mathbf{e}$. The trap axes set the reference frame. Additionally, we account for a possible off-axis imaging and consider the case of an imaging beam forming an angle α with the y axis, as shown in figure 1.

Since the Pauli exclusion principle inhibits short-range contact interaction, the long-range DDI between the particles dominates the interaction behaviour of the system. If the polarisation direction of the dipoles is defined by a unit vector $\mathbf{e}$, the DDI is described by

$$V_{\mathrm{dd}}(\mathbf{r}) = -\frac{C_{\mathrm{dd}}}{4\pi}\frac{3(\mathbf{r}\cdot\mathbf{e})^2 - \mathbf{r}^2}{r^5}, \tag{1}$$

where $\mathbf{r}$ denotes the relative position of two dipoles and C_{dd} is the dipolar interaction strength. For electric dipoles, it is given by $C_{\mathrm{dd}} = m^2/\varepsilon_0$ with ε_0 being the vacuum permittivity, while for magnetic dipoles $C_{\mathrm{dd}} = \mu_0 m^2$, where μ_0 is the vacuum permeability. In this context, an important role is played by the Fourier transform of the DDI potential [58]

$$\tilde{V}_{\mathrm{dd}}(\mathbf{k}) = \frac{C_{\mathrm{dd}}}{3}\left[3\frac{(\mathbf{e}\cdot\mathbf{k})^2}{k^2} - 1\right], \tag{2}$$

as it simplifies the evaluation of the Hartree–Fock mean-field energy of the system. We also assume that the system is trapped by a triaxial anisotropic harmonic potential given by

$$V_{\mathrm{trap}}(\mathbf{r}) = \frac{M}{2}(\omega_x^2 x^2 + \omega_y^2 y^2 + \omega_z^2 z^2), \tag{3}$$

where ω_i with $i = x, y, z$ denote the respective trap frequencies.

2.1. Wigner function in equilibrium

The physical properties of the above described system can be captured by means of the semiclassical Wigner function [50]. Indeed, the quantum-mechanical expectation values of the system observables, which are required for the calculation of the properties of nonrelativistic quantum systems based on exact diagonalization, can be obtained as their phase-space averages, weighted by the Wigner function. In the case where the dipolar orientation axis lies along one of the trapping axes, an accurate ansatz for the Wigner function takes the simple form [38–47]

$$\Theta\left(1 - \sum_i \frac{r_i^2}{R_i^2} - \sum_i \frac{k_i^2}{K_i^2}\right), \tag{4}$$

where Θ represents the Heaviside step function, while the variational parameters R_i and K_i stand for the Thomas–Fermi radius and the Fermi momentum in the direction $i = x, y, z$, respectively. This ansatz is motivated by the Fermi–Dirac distribution of a noninteracting Fermi gas at zero temperature, whose Wigner function has the above form. A theory based on the above ansatz [38, 47] was successfully used to determine the deformation of the FS, while its extension [46] enabled a detailed analysis of the ground state and the time-of-flight (TOF) expansion dynamics of the system for different collisional regimes. Furthermore, numerical comparisons [59, 60] have confirmed that, even in the case of polar molecules with masses of the order of 100 atomic units and an electric dipole moment as large as 1D, the above variational ansatz yields highly accurate results, within a fraction of per mille. This indicates that the general ansatz (4), first introduced in a slightly different manner in [38], is indeed very well suited to describe dipolar Fermi gases.

However, the experiment of [37] was performed for an arbitrary angle θ, and therefore the comparison of the theory [46, 47] was only possible for the special case of dipoles oriented along the z axis, i.e., for $\theta = 0°$. Therefore, in order to model the global equilibrium distribution of the dipolar Fermi gas for arbitrarily oriented dipoles and to provide an accurate description of the experiment, it is necessary to generalise the ansatz (4). This is done in the present paper, where we apply an analogous reasoning and introduce the following ansatz for the Wigner distribution

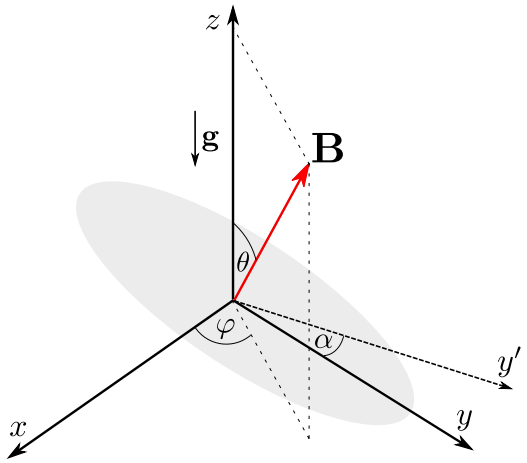

Figure 1. Schematic illustration of the most general arbitrary geometry of a dipolar Fermi gas, which corresponds to the one used in the Innsbruck experiment with erbium atoms, see later and also [37]. Axes x, y, z indicate the harmonic trap axes. The external magnetic field $\mathbf{B} = B\mathbf{e}$ defines the orientation of the atomic dipoles, which is given by the spherical coordinates θ and φ. Earth's gravitational field is parallel to the z axis. The imaging axis, denoted by y', lies in the xy plane, and forms an angle α with the y axis.

$$\nu(\mathbf{r}, \mathbf{k}) = \Theta\left(1 - \sum_{i,j} r_i \mathbb{A}_{ij} r_j - \sum_{i,j} k_i \mathbb{B}_{ij} k_j\right), \tag{5}$$

where $\mathbb{A}_{ij}$ and $\mathbb{B}_{ij}$ are matrix elements that account for the generalised geometry of the system and determine the shape of the cloud in real space and of the FS in momentum space, respectively.

The particle density distribution in real space is determined by the trapping potential and the Hartree direct energy. Therefore, one expects that the matrix $\mathbb{A}$ can be well approximated by a diagonal matrix in the coordinate system S, which is defined by the harmonic trap axes

$$\mathbb{A} = \begin{pmatrix} 1/R_x^2 & 0 & 0 \\ 0 & 1/R_y^2 & 0 \\ 0 & 0 & 1/R_z^2 \end{pmatrix}. \tag{6}$$

In this way, we neglect off-diagonal elements, which may arise due to the dipoles' arbitrary orientation. However, this is certainly justified for elongated traps, for which the cloud shape in the ground state is well determined by the trap. Therefore, we will consider here trap configurations that satisfy this condition.

On the other side, the momentum distribution is dominated by the interplay between the Pauli pressure, which is isotropic, and the Fock exchange energy, which is responsible for the deformation of the FS [38]. The experiment of [37] suggested that the FS follows the rotation of the external field, keeping the major axis of the FS always parallel to the direction of the maximum attraction of the DDI. Motivated by this, we will consider several possible scenarios for a detailed theoretical description, in order to verify the above hypothesis.

For the sake of completeness, we start with a simple spherical scenario, in which the FS remains a sphere, as displayed in figure 2(a). In that case all Fermi momenta are equal ($K_i = K_\mathrm{F}$) and the matrix $\mathbb{B}$ is given by $\mathbb{B}_1 = \mathbb{I}/K_\mathrm{F}^2$, where $\mathbb{I}$ is the 3×3 identity matrix. We also consider a second, on-axis scenario, which includes the FS deformation such that it is an ellipsoid with fixed major axes coinciding with the trap axes, as shown in figure 2(b). Here the matrix $\mathbb{B}$ has a diagonal form

$$\mathbb{B}_2 = \begin{pmatrix} 1/K_x^2 & 0 & 0 \\ 0 & 1/K_y^2 & 0 \\ 0 & 0 & 1/K_z^2 \end{pmatrix}, \tag{7}$$

in a similar way as the matrix $\mathbb{A}$, which recovers the old ansatz given by (4). We note that the first, spherically-symmetric scenario is a special case of the second ansatz, obtained by restricting the Fermi momenta to be equal. Finally, as a third and more general possibility, we consider the off-axis hypothesis of [37] and assume that the matrix $\mathbb{B}$ has a diagonal form $\mathbb{B}_3'$ in a rotated coordinate system S', which is defined by the axes q_x, q_y and q_z, where the q_z axis remains parallel to the dipole moments, as depicted in figure 2(c)

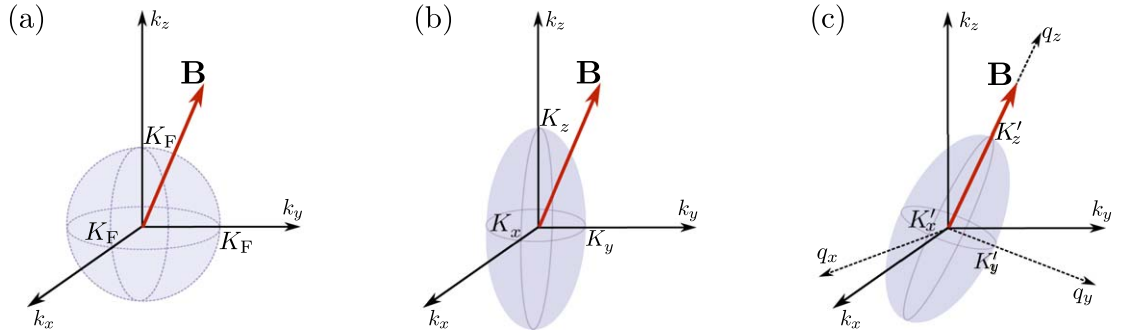

Figure 2. Schematic illustration of possible FS configurations in the presence of an external field **B**, described by spherical coordinates $\mathbf{B} = (B, \theta, \varphi)$. (a) Spherical scenario: FS remains spherical. (b) On-axis scenario: FS is deformed into an ellipsoid whose axes coincide with the trap axes. (c) Off-axis scenario: FS is deformed into an ellipsoid stretched in the direction of **B**.

$$\mathbb{B}_3' = \begin{pmatrix} 1/K_x'^2 & 0 & 0 \\ 0 & 1/K_y'^2 & 0 \\ 0 & 0 & 1/K_z'^2 \end{pmatrix}. \tag{8}$$

Here the parameters K_i' represent the Fermi momenta in the rotated coordinate system S'. In order to describe the rotation from S to S', we introduce a rotation matrix $\mathbb{R}$,

$$\mathbb{R} = \begin{pmatrix} \cos\theta\cos\varphi & -\sin\varphi & \sin\theta\cos\varphi \\ \cos\theta\sin\varphi & \cos\varphi & \sin\theta\sin\varphi \\ -\sin\theta & 0 & \cos\theta \end{pmatrix}, \tag{9}$$

such that $\mathbb{B}_3' = \mathbb{R}^T\mathbb{B}_3\mathbb{R}$ and $\mathbf{q} = \mathbb{R}^T\mathbf{k}$, where the angles θ and φ are defined in figure 1. We again note that the on-axis scenario is a special case of the off-axis one when the dipoles are parallel to one of the trap axes. For example, for $\theta = \varphi = 0°$ the matrix $\mathbb{B}_3$ is already diagonal, i.e., $K_i' = K_i$. We also note that, for all considered ansätze, the normalisation of the Wigner distribution $\nu(\mathbf{r}, \mathbf{k})$ is given by

$$N = \int\int \frac{\mathrm{d}^3r\mathrm{d}^3k}{(2\pi)^3}\nu(\mathbf{r}, \mathbf{k}) = \frac{\bar{R}^3\bar{K}'^3}{48}, \tag{10}$$

where the bar denotes the geometric averaging: $\bar{R} = (R_xR_yR_z)^{1/3}$ and $\bar{K}' = (K_x'K_y'K_z')^{1/3}$.

To determine the values of the variational parameters for each scenario, as usual, we require that they minimise the total Hartree–Fock energy of the system. This leads, together with the particle number conservation (10), to algebraically self-consistent equations that determine the Thomas–Fermi radii and momenta. In section 2.2 we calculate the total energy of the system for each of the outlined scenarios and then in section 3.1 we proceed to determine the one that yields a minimal energy and that will be used in the rest of the paper. We note that one can certainly consider even more general ansätze, however, as we will see from the comparison with the experimental data, the proposed approach is fully suitable for describing our system not only qualitatively, but also quantitatively.

2.2. Total energy

Now that we have identified several relevant ansätze for describing the Wigner function of a dipolar Fermi gas of tilted dipoles, we proceed to determine the optimal values of the variational parameters. In order to do so, we have to minimise the total energy of the many-body Fermi system, which is in the Hartree–Fock mean-field theory given by the sum of the kinetic energy E_{kin}, the trapping energy E_{trap}, the Hartree direct energy $E_{\mathrm{dd}}^{\mathrm{D}}$, and the Fock exchange energy $E_{\mathrm{dd}}^{\mathrm{E}}$. Within a semiclassical theory, they can be written in terms of the Wigner function according to [50]

$$E_{\mathrm{kin}} = \int\int \frac{\mathrm{d}^3r\mathrm{d}^3k}{(2\pi)^3}\frac{\hbar^2\mathbf{k}^2}{2M}\nu(\mathbf{r}, \mathbf{k}), \tag{11}$$

$$E_{\mathrm{trap}} = \int\int \frac{\mathrm{d}^3r\mathrm{d}^3k}{(2\pi)^3}V_{\mathrm{trap}}(\mathbf{r})\nu(\mathbf{r}, \mathbf{k}), \tag{12}$$

$$E_{\mathrm{dd}}^{\mathrm{D}} = \frac{1}{2}\int\int\int\int \frac{\mathrm{d}^3r\mathrm{d}^3r'\mathrm{d}^3k\mathrm{d}^3k'}{(2\pi)^6}V_{\mathrm{dd}}(\mathbf{r}-\mathbf{r}')\nu(\mathbf{r}, \mathbf{k})\nu(\mathbf{r}', \mathbf{k}'), \tag{13}$$

$$E_{\rm dd}^{\rm E} = -\frac{1}{2}\int\int\int\int \frac{{\rm d}^3r{\rm d}^3r'{\rm d}^3k{\rm d}^3k'}{(2\pi)^6} V_{\rm dd}(\mathbf{r}')\,{\rm e}^{{\rm i}(\mathbf{k}-\mathbf{k}')\cdot\mathbf{r}'}\nu(\mathbf{r},\,\mathbf{k})\nu(\mathbf{r},\,\mathbf{k}'), \tag{14}$$

and have already been calculated before with an ansatz (4) for the case when the dipoles are parallel to one of the trap axes [38, 44–47]. Whereas both the kinetic energy (11) and the trapping energy (12) yield simple integrals, the computation of the integrals in the Hartree term (13) and the Fock term (14) is nontrivial and is therefore presented for the most general case in appendices A and B, respectively.

In the spherical scenario, depicted in figure 2(a), the total energy of the system can be calculated using $K_i = K_{\rm F}$ in ansatz (5), where the Fock exchange term turns out to give no contribution, yielding

$$E_{\rm tot}^{(1)} = \frac{N}{8}\left(\frac{3\hbar^2K_{\rm F}^2}{2M} + \sum_j \frac{M\omega_j^2R_j^2}{2}\right) - \frac{6N^2c_0}{\bar{R}^3} f_{\rm A}\left(\frac{R_x}{R_z},\,\frac{R_y}{R_z},\,\theta,\,\varphi\right). \tag{15}$$

Here $c_0 = 2^{10}C_{\rm dd}/(3^4\cdot 5\cdot 7\cdot \pi^3)$ is a constant related to the dipolar strength, while the features of the DDI are embodied into the generalised anisotropy function $f_{\rm A}(x,\,y,\,\theta,\,\phi)$, which includes explicitly the angular dependence of the DDI. It is defined as

$$f_{\rm A}(x,\,y,\,\theta,\,\varphi) = \sin^2\theta\cos^2\varphi\, f\left(\frac{y}{x},\,\frac{1}{x}\right) + \sin^2\theta\sin^2\varphi\, f\left(\frac{x}{y},\,\frac{1}{y}\right) + \cos^2\theta\, f(x,\,y), \tag{16}$$

where $f(x,y)$ stands for the well-known anisotropy function derived, at first, for dipolar BECs [61]. Note that $f(x,\,y) = f_{\rm A}(x,\,y,\,0,\,0)$. This function has been encountered also in previous studies of fermionic dipolar systems [45] in the hydrodynamic collisional regime, as well as in the transition from the collisionless to the hydrodynamic regime in both the TOF expansion dynamics [46] and collective excitations [47]. More details on the anisotropy and the generalised anisotropy function are given in appendix C.

In the on-axis scenario, the FS is deformed to an ellipsoid whose axes are taken to be parallel to the trap axes, as shown in figure 2(b). This ansatz leads to the total energy of the system given by

$$E_{\rm tot}^{(2)} = \frac{N}{8}\sum_j\left(\frac{\hbar^2K_j^2}{2M} + \frac{M\omega_j^2R_j^2}{2}\right) - \frac{6N^2c_0}{\bar{R}^3}\left[f_{\rm A}\left(\frac{R_x}{R_z},\,\frac{R_y}{R_z},\,\theta,\,\varphi\right) - f_{\rm A}\left(\frac{K_z}{K_x},\,\frac{K_z}{K_y},\,\theta,\,\varphi\right)\right]. \tag{17}$$

Note that (17) reduces, indeed, to (15) for the special case of $K_x = K_y = K_z$, since $f_{\rm A}(1,\,1,\,\theta,\,\varphi) = 0$.

Finally, in the most-general considered off-axis scenario displayed in figure 2(c), we allow for both the FS deformation and its rotation so that one of its axes is parallel to the external field. In this case, the total energy of the system reads as

$$E_{\rm tot}^{(3)} = \frac{N}{8}\sum_j\left(\frac{\hbar^2K_j'^2}{2M} + \frac{M\omega_j^2R_j^2}{2}\right) - \frac{6N^2c_0}{\bar{R}^3}\left[f_{\rm A}\left(\frac{R_x}{R_z},\,\frac{R_y}{R_z},\,\theta,\,\varphi\right) - f\left(\frac{K_z'}{K_x'},\,\frac{K_z'}{K_y'}\right)\right]. \tag{18}$$

Note that the above form of the Fock energy in the last term is not surprising if we bear in mind the form of equation (16). Namely, in the rotated coordinate system S', the axis q_z coincides with the direction of the external field, so the generalised anisotropy function $f_{\rm A}$ reduces to the standard anisotropy function f, just with the arguments K_i' from the rotated system.

3. Ground-state properties

Having obtained the total energy for all three scenarios, we now determine which configuration minimises the system's total energy for a fixed particle number and, hence, can be considered as the most physically suitable ansatz for the ground state of the system of dipolar fermions. Afterwards, we use it to numerically calculate the FS and atomic cloud deformation, and discuss the obtained results.

In practical terms, we start from (15), (17) and (18), and minimise the energy of the system for each scenario under the constraint (10) that the particle number N is fixed to a given value. Therefore, the corresponding equations are obtained by extremizing the grand-canonical potential $\Omega^{(k)} = E_{\rm tot}^{(k)} - \mu N$ for $k = 1, 2, 3$ with respect to the variational parameters, where μ is the chemical potential of the system, and the particle number N in the last term is replaced by the expression (10) when $\Omega^{(k)}$ is evaluated. In this way, the chemical potential acts as a Lagrange multiplier and fixes the particle number through the condition $N = -\partial\Omega^{(k)}/\partial\mu$.

In the spherical scenario, there are five variational parameters, $(K_{\rm F}, R_i, \mu)$, where $i = x, y, z$. The corresponding five equations are obtained by setting the first derivatives of $\Omega^{(1)}$ with respect to $K_{\rm F}$ and R_i to zero, plus the particle-number fixing equation, i.e., $N = -\partial\Omega^{(1)}/\partial\mu$. In both the on-axis and the off-axis scenario we have seven variational parameters: (K_i, R_i, μ) and (K_i', R_i, μ), respectively. The sets of seven equations for both

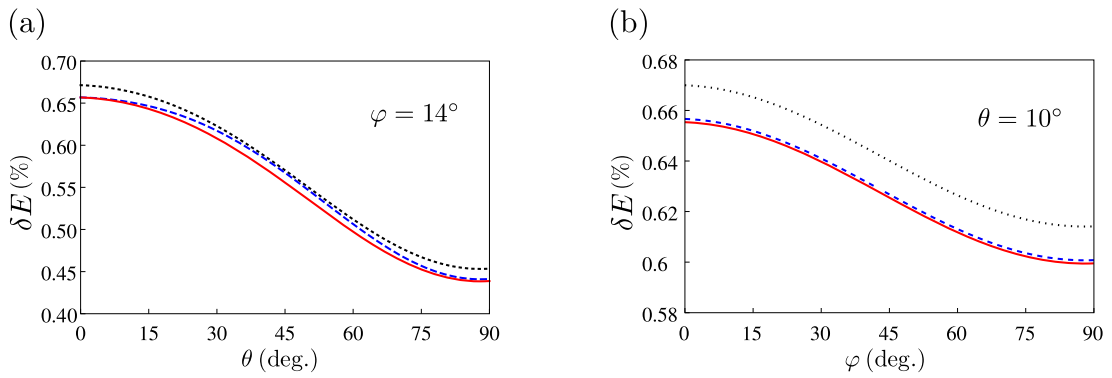

Figure 3. Relative total energy shift (19) for experimental parameters of [37] as a function of: (a) angle θ, for fixed $\varphi = 14°$; (b) angle φ for fixed $\theta = 10°$. The three curves, correspond to $\delta E^{(1)}$ (black dotted line, spherical scenario), $\delta E^{(2)}$ (blue dashed line, on-axis scenario), and $\delta E^{(3)}$ (red solid line, off-axis scenario).

cases are obtained similarly as in the previous case. The complete sets of equations for the respective variational parameters for all cases are given in appendix D.

3.1. Minimisation of total energy

In order to compare the three ansätze, we solve the corresponding sets of equations and calculate the total energy of the system in each case. As a model system, we consider the case of a dipolar Fermi gas of atomic ^{167}Er, using the typical values from the Innsbruck experiments (see below and also [37]), $N = 6.6 \times 10^4$, $(\omega_x, \omega_y, \omega_z) = (579, 91, 611) \times 2\pi$ Hz, unless otherwise specified. The underlying geometry of the experimental setup is depicted in figure 1.

In figure 3 we compare the total energy of the system as a function of angles θ and φ for all three different scenarios. The comparison is done in terms of the relative total energy shift

$$\delta E = \frac{E_{\text{tot}}}{E_0} - 1, \tag{19}$$

where $E_0 = \frac{3}{4} N E_{\text{F}}$ stands for the total energy of the ideal Fermi gas confined into a harmonic trap (3), and $E_{\text{F}} = \hbar\bar{\omega}(6N)^{1/3}$ denotes its Fermi energy, where $\bar{\omega} = (\omega_x \omega_y \omega_z)^{1/3}$. Figure 3(a) presents the relative total energy shifts as functions of the angle θ for a fixed value of the angle $\varphi = 14°$, corresponding to the typical experimental configuration (see below). The three curves, from top to bottom, correspond to $\delta E^{(1)}$, $\delta E^{(2)}$, and $\delta E^{(3)}$, respectively. As a cross-check, we note that the total energies $E^{(2)}_{\text{tot}}$ and $E^{(3)}_{\text{tot}}$ coincide for $\theta = 0°$. This is expected, since the on-axis scenario is a special case of the off-axis one for $\theta = 0°$. From this figure we immediately see that there are no intersections between the curves, and that it always holds $E^{(1)}_{\text{tot}} \geqslant E^{(2)}_{\text{tot}} \geqslant E^{(3)}_{\text{tot}}$. As a consequence, we conclude that the off-axis scenario, in which the FS is deformed into an ellipsoid that follows the orientation of the dipoles, is favoured among the considered cases as it has the minimal energy. The same conclusion is obtained if we consider the φ-dependence of the relative total energy shifts, depicted in figure 3(b) for a fixed value of the angle $\theta = 10°$. More exhaustive numerical calculations show that this remains to be true even for arbitrary values of the angles θ and φ.

Comparing figures 3(a) and (b) we see that the relative total energy shift always remains small, of the order of 0.4%–0.7%, due to a relatively weak DDI between the erbium atoms compared to the energy scale set by the Fermi energy. We also see that the θ-dependence of the total energy is much stronger than the corresponding φ-dependence. We note that the shift would certainly be more significant for atomic and molecular species with a stronger DDI.

The above conclusion is valid not only for the parameters used in figure 3, but, in fact, we have numerically verified that the off-axis scenario for the ansatz (5) for the Wigner function in global equilibrium always yields a minimal energy given by (18) and, thus, we will use it throughout the rest of the paper. The corresponding equations determining all seven variational parameters are given in appendix D as (D.13)–(D.19). A closer examination of those equations reveals that the FS is always a cylindrically symmetric ellipsoid, where $K'_x = K'_y$ holds. This is expected, since the orientation of the dipoles in the rotated coordinate system coincides with the q_z axis and singles this particular direction out, leaving the perpendicular plane perfectly symmetric in momentum space. Therefore, as shown in appendix D, the equations for the seven variational parameters can be rewritten in a more convenient form as (D.16)–(D.22).

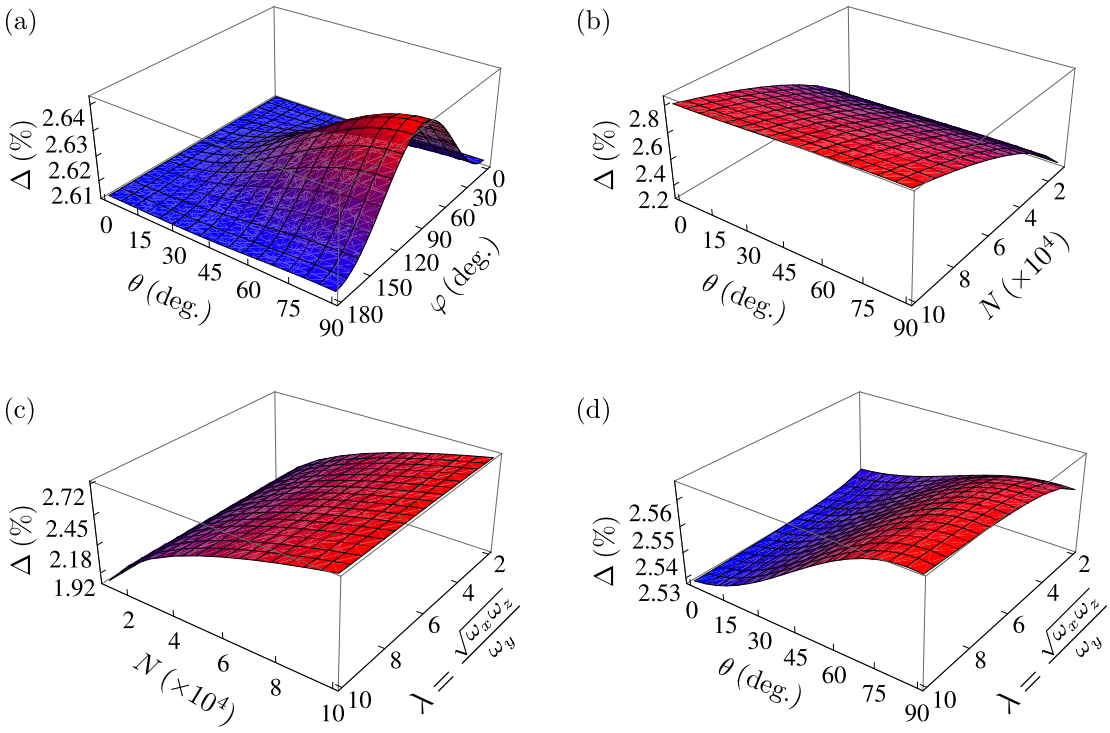

Figure 4. FS deformation Δ for ^{167}Er atoms with magnetic dipole moment $m = 7\mu_B$ as a function of: (a) dipoles' orientation angles θ and φ, for parameters of [37]; (b) particle number N and angle θ, for $\varphi = 90°$ and trap frequencies of [37]; (c) particle number N and trap anisotropy λ, for $\theta = \varphi = 90°$; (d) angle θ and trap anisotropy λ, for $\varphi = 90°$ and $N = 6.6 \times 10^4$. Trap anisotropy λ in (c) and (d) was varied by changing the frequencies $\omega_x = \omega_z$ and ω_y, while keeping the mean frequency $\bar{\omega} = 300 \times 2\pi$ Hz constant.

3.2. FS deformation

Now that we have shown that the FS is, indeed, deformed by the DDI into an ellipsoid, which follows the orientation of the dipoles, we study the angular dependence of this deformation in more detail. To that end, and taking into account the cylindrical symmetry of the FS, we define the FS deformation as the difference between the momentum-space aspect ratio for the dipolar and the noninteracting Fermi gas in the rotated system S' according to

$$\Delta = \frac{K'_z}{K'_x} - 1. \tag{20}$$

This quantity measures the degree of deformation, which emerges purely due to the DDI. In particular, we investigate how the deformation Δ depends on the trap geometry, the orientation of the dipoles, the DDI strength, and the number of particles. The DDI strength is usually expressed in terms of a dimensionless relative strength ε_{dd}, defined as

$$\varepsilon_{dd} = \frac{C_{dd}}{4\pi}\sqrt{\frac{M^3\bar{\omega}}{\hbar^5}}N^{1/6}, \tag{21}$$

which gives a rough estimate of the ratio between the mean dipolar interaction energy and the Fermi energy. We will use it to characterise the strength of the DDI when comparing its effects for different species.

We now calculate the FS deformation of ^{167}Er for the parameters of [37], yielding the relative interaction strength $\varepsilon_{dd} = 0.15$. In figure 4(a) we present the angular dependence of Δ on θ and φ, whose values turn out to be around 2.6%, consistent with earlier experimental results [37]. We observe that there is a maximum deformation of the FS at $\theta = \varphi = 90°$, which corresponds to the direction of the smallest trapping frequency ω_y (y axis). This can be understood heuristically, if one recalls that the DDI is attractive for dipoles oriented head-to-tail. Thus, a weaker trapping frequency favours the stretching of the gas in that direction so that, in turn, this cigar-shaped configuration enhances the relative contribution of the DDI to the total energy.

Another aspect relevant for experiments is the influence of the particle number N and the trap geometry on the deformation of the FS. Tuning these parameters and the direction of the dipoles might lead to an enhancement of the DDI effects, and therefore to a stronger deformation of the FS. This is investigated in figures 4(b)–(d), where the FS deformation is given as a function of parameters N, θ and the trap anisotropy $\lambda = \sqrt{\omega_x\omega_z}/\omega_y$ for a fixed value of the angle $\varphi = 90°$. Figures 4(c) and (d) explore the FS deformation as a

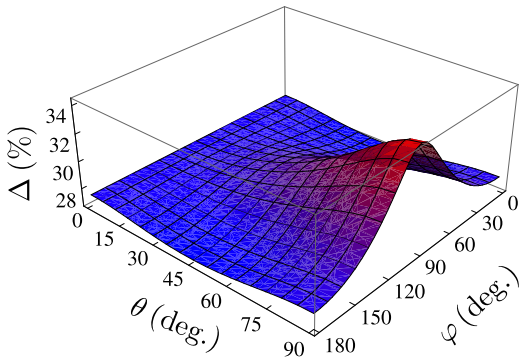

Figure 5. Angular dependence of FS deformation Δ for polar molecules with electric dipole moment $m = 0.25$ D and relative DDI strength $\varepsilon_{dd} = 1.51$ for parameters of [37].

function of the trap anisotropy λ, which was varied by changing the frequencies $\omega_x = \omega_z$ and ω_y, while keeping the mean frequency $\bar{\omega} = 300 \times 2\pi$ Hz constant. From all these figures we conclude that the increase in the particle number yields a dominant increase in Δ compared to all other parameters. We note that, in fact, Δ also depends on $\bar{\omega}$, which we do not show here, since it can be directly connected to the particle number dependence. Indeed, the FS deformation depends on ε_{dd} [37], yielding a dependence of Δ on $N^{1/6}\bar{\omega}^{1/2}$. As the trap frequencies can be more easily tuned than the particle number, $\bar{\omega}$ can be considered as a predominant control knob in the experiment. However, a precise control of the angles and the anisotropy, which is experimentally easy to realise, may help to achieve an even larger increase in the deformation of the FS. We also note that the λ-dependence is the weakest one, and therefore the formalism for calculating the angular dependence presented here is significant for a systematic study of the influence of the relevant parameters.

Finally, we study the role of the DDI strength and explore whether qualitative changes of the system's behaviour emerge by increasing the value of the dipole moment. To this aim, we compare the erbium case with a molecular Fermi gas of ^{40}K^{87}Rb, assuming that the same gas characteristics can be achieved in the same trap with this species [54]. The latter possesses an electric dipole moment of strength $m = 0.56$ D, yielding a much larger relative interaction strength $\varepsilon_{dd} = 7.76$ for the same parameters. Since the critical value of ε_{dd}, for which the system is stable, amounts to $\varepsilon_{dd}^{crit} = 2.5$ [46], the molecular ^{40}K^{87}Rb gas in such a geometry and with the maximal strength of the DDI would in fact not be stable and would collapse under the attractive action of the DDI. For the sake of simplicity and comparison between the systems, we consider a molecular sample of similar geometry and atom number but in which the dipole moment has been tuned to $m = 0.25$ D by means of an external field [34]. This leads to the relative DDI strength $\varepsilon_{dd} = 1.51$, which we use in the following.

As we see, the FS deformation Δ has a much stronger angular dependence in figure 5 than in figure 4(a) for the erbium case. Furthermore, in figure 5 we see that Δ has a local minimum for $\varphi = 0°$ around $\theta = 40°$, while no such minimum exists in figure 4(a). Only a detailed numerical study based on the formalism developed here can provide a precise landscape of the FS deformation behaviour for a concrete experimental setup.

Although the shapes of both angular dependencies in figures 4(a) and 5 are quite similar, the main difference is that the deformation of the FS for polar molecules is an order of magnitude larger than for erbium and has a value of around 30%. However, we also observe that the variation in the values of Δ for different angles θ and φ is around 0.03% in the case of an atomic erbium gas, while for the molecules it amounts to around 5%, i.e., the variations of Δ are two orders of magnitude larger for the molecular case. The reason for this increase in both the maximal FS deformation and its angular variation is the same, namely the increase in the relative DDI strength ε_{dd}, which is one order of magnitude larger for our molecules compared to ^{167}Er. While the FS deformation is proportional to ε_{dd}, as expected [46] and as evidenced by our results above, our findings suggest that its maximal angular variation is proportional to ε_{dd}^2.

The calculated angular dependence of the FS deformation on the DDI strength has the following important physical consequence. For erbium atoms, where ε_{dd} is small, the angular variation of the FS deformation is even smaller, since it is proportional to ε_{dd}^2, and it would be difficult to observe in experiments. Therefore, one could say that the FS behaves as a rigid ellipsoid, which just rotates following the orientation of the dipoles, without changing its shape [37], as illustrated in figure 6(a). This also implies that the atomic cloud shape in real space is practically disentangled from the FS, and is mainly determined by the trap shape. On the other hand, when ε_{dd} is large enough, as in the case of ^{40}K^{87}Rb, the FS not only rotates, but also significantly changes its shape, since the angular variation can be as high as 5%, which is experimentally observable. This is schematically shown in figure 6(b), where the FS behaves as a soft ellipsoid, whose axes are stretched as it rotates. Although we know that the phase-space volume is preserved, according to the particle number conservation (10), figure 6(b) illustrates

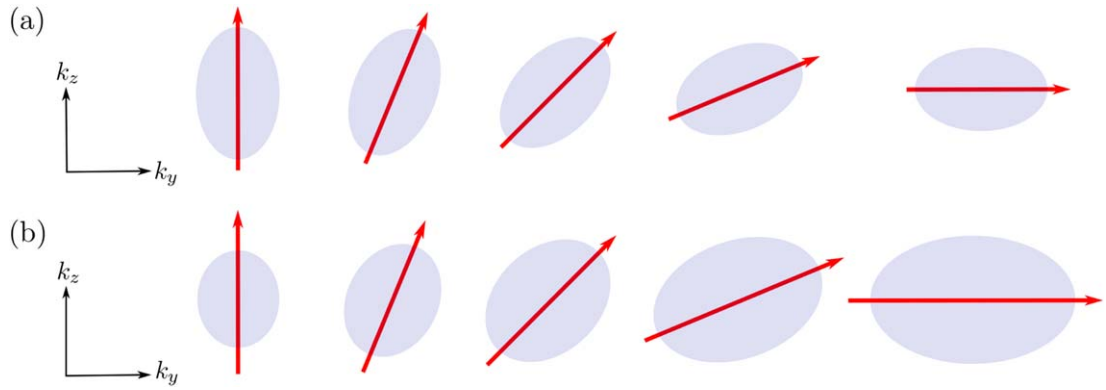

Figure 6. Illustration of the angular dependence of the FS deformation in momentum space for system in an anisotropic trap elongated along the horizontal y axis (see figure 1): (a) for weak DDI, when the FS ellipsoid just rotates like a rigid object; (b) for strong DDI, when the FS ellipsoid stretches in all directions and its deformation strongly depends on the dipoles' orientation.

that the FS, i.e., the momentum-space volume increases (K_i' increase), while in real space the volume of the cloud shape decreases (R_i decrease). From this we see that the real-space atomic cloud shape is indeed coupled to the FS, and this effect can become measurable in future dipolar fermion experiments, with sufficiently large values of $\varepsilon_{\rm dd}$.

3.3. Real-space magnetostriction

The presence of the DDI in both bosonic [62] and fermionic [50] quantum gases has been predicted and evidenced in experiment by detailed TOF expansion measurements [63] to induce magnetostriction in real space, i.e., a stretching of the gas cloud along the direction of the dipoles. In this section we investigate the dependence of this effect on the orientation of the dipoles for the fermionic case. To this end, we first define real-space aspect ratios $A_{ij} = R_i/R_j$ of the corresponding Thomas–Fermi radii, as well as their noninteracting counterparts $A_{ij}^0 = R_i^0/R_j^0 = \omega_j/\omega_i$. The magnetostriction can now be studied in terms of the relative cloud deformations:

$$\delta_{xz} = A_{xz}/A_{xz}^0 - 1, \quad \delta_{yz} = A_{yz}/A_{yz}^0 - 1. \tag{22}$$

Here the anisotropies due to the harmonic trap are already taken into account and eliminated, so that only effects of the DDI contribute to the nontrivial value of δ_{xz} and δ_{yz}. This is in close analogy to the definition of the relative total energy shift of the system in (19), or the FS deformation in (20).

In figure 7 we present the angular dependence of the relative cloud deformations for the Fermi gas of erbium with the same parameters as in figure 4(a). We see that both deformations for a fixed angle $\theta > 0$ turn out to possess a minimum for $\varphi = 90°$, while along the φ direction the FS deformation monotonously increases. If we compare this to the behaviour in momentum space, see figure 4(b), we see that along the φ direction we have qualitatively the same type of increasing dependence, while the behaviour in the θ direction is markedly different. Indeed, in momentum space it exhibits a maximum for $\varphi = 90°$, while in real space we observe a minimum value in that direction for $\varphi = 90°$. A related effect has been previously found, showing that the Bose gas momentum becomes distorted in the opposite sense to that of the Fermi gas [40]. There, the effect can be traced back to the differences in the statistical nature of bosons and fermions. Here, however, the different behaviour is due to the anisotropic nature of the DDI and its interplay with the direction of the dipoles and the trap geometry.

4. Comparison with the experiment

Having developed a general theoretical framework and having numerically studied the ground-state properties of dipolar Fermi gases with arbitrary oriented dipoles in the two previous sections, we now compare those results with experimental data obtained in our experimental setup in Innsbruck, producing degenerate Fermi gases of erbium [32]. The FS deformation was first observed with this setup and reported in reference [37]. Here we performed additional measurements, using different trapping configurations to test our theoretical understanding developed above. In these experiments the FS deformation is probed by the TOF expansion measurements. Starting from a degenerate Fermi gas with $N \sim 6$–7×10^4 atoms and at the temperature $T/T_{\rm F} \sim 0.2$, we slowly set the cloud geometry and dipole orientation to the one of interest, let the cloud

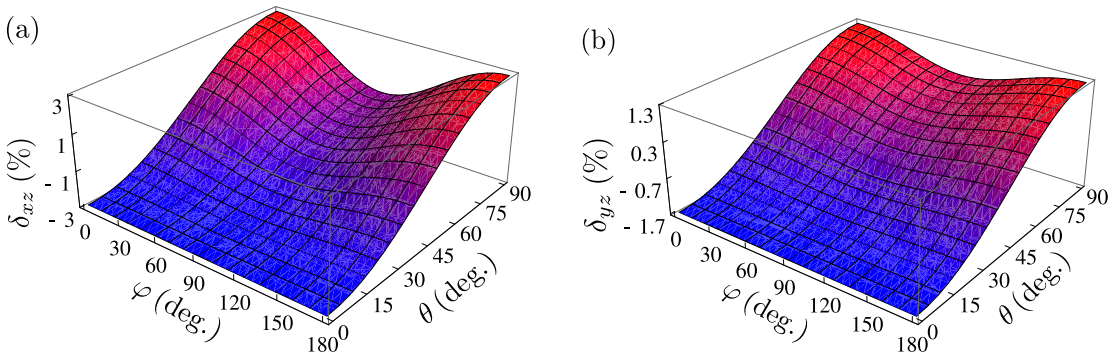

Figure 7. Angular dependence of relative cloud deformation (22) for ^{167}Er, with parameters as in figure 4(a): (a) δ_{xz}; (b) δ_{yz}.

equilibrate for several hundreds of milliseconds and then suddenly remove the trapping potential. After a free expansion of duration t, we perform standard absorption imaging along a fixed direction, see figure 1.

Before we compare theory and experiment, let us note again that our theoretical results are only valid for $T = 0$. For finite temperatures the isotropic thermal fluctuations have already been shown to work against any directional dependence stemming from either the harmonic confinement or the DDI, thus they diminish the FS deformation. The thermal corrections to the total energy are known to be proportional to $(T/T_F)^2$ at low T [64]. The corresponding effect on the FS deformation was also previously theoretically [65] and experimentally [37] investigated, showing similar scalings. However, for the low temperatures of our experiments, this would yield only a few percent correction to the zero-temperature results, which lies within the experimental error bars. Therefore, we can neglect the thermal corrections here. Generally speaking, the value of $(T/T_F)^2$ can be used to estimate the relevance of the finite-temperature effects for $T/T_F < 0.5$, while $(T/T_F)^{-5/2}$ should be considered for larger temperatures [65].

4.1. Aspect ratios and FS deformation

The TOF images are taken in the plane perpendicular to the imaging axis and the deformation of the atomic cloud is described in terms of the time-dependent cloud aspect ratio A_R, which is defined as a ratio of vertical and horizontal radii of the cloud in the imaging plane. As depicted in figure 1, the imaging axis y' is in the xy plane, rotated by an angle α to the y axis, and the aspect ratio A_R is given by [46]

$$A_R(t) = \sqrt{\frac{\langle r_z^2(t)\rangle}{\langle r_x^2(t)\rangle \cos^2\alpha + \langle r_y^2(t)\rangle \sin^2\alpha}}, \tag{23}$$

where $\langle r_i^2(t)\rangle$ is the average size of the cloud in the direction $i = x, y, z$ after TOF. These quantities are directly measurable in the experiment, and we use them to extract the value of the deformation of the FS, which is connected to the aspect ratio in momentum space. It is defined similarly as A_R [46], according to

$$A_K = \sqrt{\frac{\langle k_z^2\rangle}{\langle k_x^2\rangle \cos^2\alpha + \langle k_y^2\rangle \sin^2\alpha}}, \tag{24}$$

where $\langle k_i^2\rangle$ is the average size of the FS in the direction $i = x, y, z$ in global equilibrium, before the trap is released. Using the definition (24), a straightforward but lengthy calculation yields the following expression for the aspect ratio in momentum space in terms of the Fermi momenta K_i' in the rotated coordinate system:

$$A_K = \sqrt{\frac{K_x'^2 \sin^2\theta + K_z'^2 \cos^2\theta}{K_x'^2[1 - \sin^2\theta(\cos^2\varphi\cos^2\alpha + \sin^2\varphi\sin^2\alpha)] + K_z'^2 \sin^2\theta(\cos^2\varphi\cos^2\alpha + \sin^2\varphi\sin^2\alpha)}}. \tag{25}$$

Please note that only for $\theta = 0°$, when the dipoles are parallel to the z axis, the above momentum-space aspect ratio coincides with the ratio between the Fermi momenta, $A_K = K_z'/K_x' = 1 + \Delta$, where Δ denotes the previously introduced deformation of the FS. In general, however, the relation between A_K and Δ is nonlinear and can be obtained from (25), as follows:

$$\Delta = \sqrt{\frac{A_K^2[1 - \sin^2\theta(\cos^2\varphi\cos^2\alpha + \sin^2\varphi\sin^2\alpha)] - \sin^2\theta}{\cos^2\theta - A_K^2 \sin^2\theta(\cos^2\varphi\cos^2\alpha + \sin^2\varphi\sin^2\alpha)}} - 1. \tag{26}$$

Table 1. Number of atoms N, trap frequencies ω_i, mean frequencies $\bar{\omega}$ and anisotropies λ for three sets of experimental parameters used throughout this paper. Case 1 corresponds to [37], while Case 2 and Case 3 are new results.

^{167}Er	N ($\times 10^4$)	ω_x(Hz)	ω_y(Hz)	ω_z(Hz)	$\bar{\omega}$ (Hz)	λ
Case 1	6.6	$579 \times 2\pi$	$91 \times 2\pi$	$611 \times 2\pi$	$318 \times 2\pi$	6.54
Case 2	6.3	$428 \times 2\pi$	$91 \times 2\pi$	$459 \times 2\pi$	$261 \times 2\pi$	4.87
Case 3	6.1	$408 \times 2\pi$	$212 \times 2\pi$	$349 \times 2\pi$	$311 \times 2\pi$	1.78

In order to extract the value of the deformation of the FS from the experimental data using the above equation, we still need to calculate the momentum-space aspect ratio A_K. This is done by using the fact that the long-time expansion is mainly dominated by the velocity distribution right after the release from the trap. Here we rely on the ballistic approximation, which assumes that the TOF images, that show the shape of the atomic cloud in real space, purely reflect the momentum distribution in the global equilibrium, i.e.

$$A_K \approx \lim_{t\to\infty} A_R^{\mathrm{bal}}(t). \tag{27}$$

In principle, this is true just in the case of ballistic expansion, when the effects of the DDI can safely be neglected during the TOF. However, since the DDI is long-range, it should be taken into account, rendering the TOF results always non-ballistic. A general theory that would allow such a treatment is not yet available and is beyond the scope of the present ground-state study. Nevertheless, if the DDI is weak enough, as in the case of erbium atomic gases, the difference between the ballistic (free) and non-ballistic expansion is small, as already shown in [46]. Thus, (27) can approximately be used in our case and the value of A_K in global equilibrium can be extracted from the long-time limit of A_R, which is available from the experimental data. We highlight that in some limiting cases it is still possible to take into account a non-ballistic expansion by using the previously developed dynamical theory [46]. This is expected to yield a more precise value of the aspect ratio, as will be illustrated in the next section.

With those cautionary remarks in mind, we complete the algorithm for analysing our experimental data by calculating the FS deformation from the extracted aspect ratio using (26), which enables its comparison with our numerical results.

4.2. Experimental and theoretical results

Here we consider three different datasets corresponding to the experimental parameters listed in table 1. Case 1 corresponds to the experimental results published in [37], while Case 2 and Case 3 are new results reported here. Table 1 also gives the mean frequency of the trap $\bar{\omega}$ and the trap anisotropy λ for each case. While Cases 1 and 2 represent cigar-shaped traps, Case 2 is selected so that it has the same value of ω_y as Case 1, but a smaller anisotropy λ. On the other hand, Case 3 is chosen so that its mean frequency $\bar{\omega}$ is approximately the same as for Case 1, but its anisotropy λ is much reduced. For each dataset, we probe the FS deformation for various angles θ and a fixed angle $\varphi = 14^\circ$. The measurement for each experimental configuration is repeated a large number of times, typically twenty, so that the mean value can be reliably estimated and the statistical error is reduced below 0.2%.

Figure 8 shows a direct comparison between our experimental and theoretical results without any free parameters. Experimentally we measure the mean value of the aspect ratio A_R in free expansion using the TOF $t = 12$ ms, which is taken to be sufficiently long so that the approximation (27) can be used, and yet not too long so that the cloud does not get too dilute and a reliable fit of the density distribution from the absorption images is possible. In figure 8(a) we show the θ dependence of the measured quantity A_R(12 ms) for the parameters of Case 1 (red circles), Case 2 (blue squares) and Case 3 (black triangles), as well as the corresponding theoretical curves (solid red, dashed blue and dotted black line, respectively) for A_K at global equilibrium, calculated according to (25). We see that the agreement is generally very good, and that the experimental data are closely matched by the shape predicted by theory. At the same time, this figure also presents an *a posteriori* justification for using the ballistic approximation in those three cases.

The discrepancies observed in the figure can be accredited to the effects of the DDI, which are neglected during the TOF by using the ballistic approximation. Even better agreement between the experiment and the theory can be expected if a non-ballistic expansion would be taken into account. Although a theory for this is not yet available for an arbitrary orientation of the dipoles, [46] allows us to perform a non-ballistic expansion calculation for the special case $\theta = 0^\circ$ in the collisionless regime. The comparison of the results is given in table 2, where we see that accounting for the DDI during the TOF yields theoretical values of the TOF real-space aspect ratio equal to the experimental ones, within the error bars of the order of 0.1%. Table 2 also shows that non-ballistic effects amount to 0.7% for Case 1, which has the largest anisotropy, and becomes smaller as the

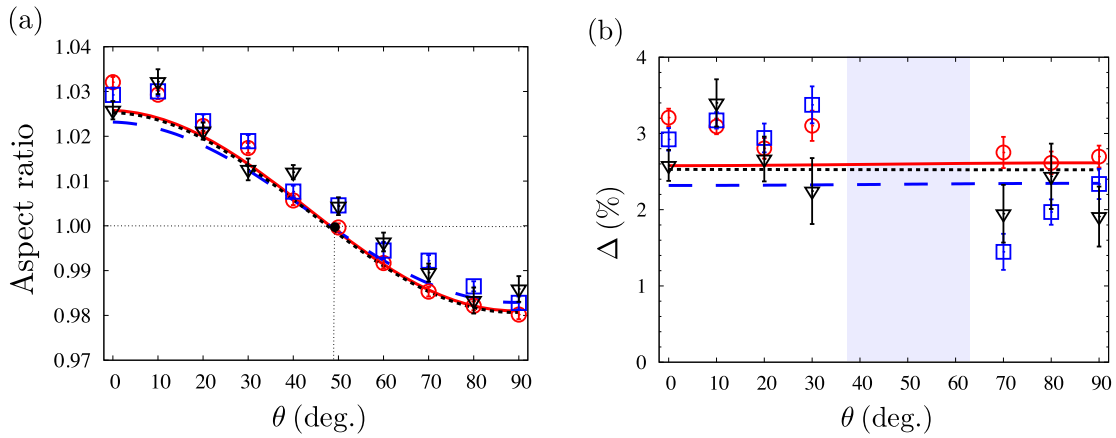

Figure 8. Comparison of our results for θ dependence of: (a) theoretical value of aspect ratio A_K and its experimental estimate $A_R^{exp}(t = 12$ ms) according to (27); (b) theoretical value of the FS deformation Δ and its experimental estimate (see main text). Red solid lines and circles correspond to Case 1, blue dashed lines and squares correspond to Case 2, and black dotted lines and triangles correspond to Case 3. Vertical bars for experimental results correspond to statistical errors. Angle $\varphi = 14°$ was kept constant during the experiment. Intersection point of three curves in panel (a) corresponds to $(\theta^*, A_K^*) = (49.16°, 1)$, while shaded area in panel (b) is excluded due to a pole in (28); see main text for further details.

Table 2. Comparison of theoretical values of aspect ratios in momentum space A_K in global equilibrium and TOF aspect ratios in real space: theoretical value of A_R^{nbal} and experimental value of A_R^{exp}, with corresponding statistical errors ΔA_R^{exp}. Real-space aspect ratios correspond to TOF of $t = 12$ ms and $\theta = 0°$. Last two columns give trap mean frequency $\bar{\omega}$ and anisotropy λ for each case.

^{167}Er	A_K	A_R^{nbal}	A_R^{exp}	ΔA_R^{exp}	$\bar{\omega}$ (Hz)	λ
Case 1	1.0258	1.0324	1.0321	0.0012	$318 \times 2\pi$	6.54
Case 2	1.0232	1.0282	1.0292	0.0015	$261 \times 2\pi$	4.87
Case 3	1.0253	1.0270	1.0258	0.0020	$311 \times 2\pi$	1.78

trap is closer to a spherical shape, i.e., as the trap anisotropy approaches the value of 1. Therefore, we conclude that the agreement of experimental data and theoretical results in figure 8(a) can be further improved by developing a theory for a non-ballistic expansion for a general experiment geometry, which is out of the scope of the present study.

Figure 8(b) shows a comparison of our theoretical and experimental results for the deformation Δ of the FS for the three considered cases, where the experimental values are calculated according to (26), assuming ballistic expansion (27) and using the real-space aspect ratios shown in figure 8(a). Although the statistical error bars ΔA_R^{exp} for the experimentally measured values of the real-space aspect ratios are small and almost constant, the corresponding errors for the FS deformation, calculated as

$$\Delta A_R^{exp} \left| \frac{\partial \Delta}{\partial A_K} \right|_{A_K = A_R^{exp}}, \tag{28}$$

show a strong angular dependence, due to the presence of a pole in the function $\partial\Delta/\partial A_K$. For the parameters of figure 8, the pole emerges at around $\theta = 50°$. Therefore, the error bars appear significantly larger in the neighbouring region, which justifies to drop the data points around $\theta = 50°$ (shaded area in the graph).

As can be seen in figure 8(b), for all three cases the deformation of the FS is almost constant for all angles θ. Therefore, from the experimental point of view, it would be enough just to measure the aspect ratio for one value of θ, e.g., $\theta = 0°$ in order to determine the deformation of the FS. However, this is only true for a weak enough DDI. Nevertheless, even if this is the case, the measurement of the angular dependence of A_R is an indispensable tool for a full verification of the developed theory, as demonstrated in figures 8(a) and (b).

4.3. Universal consequences of geometry

As already observed in figure 8(a), the A_K curves for all three considered cases intersect at a special point $(\theta^*, A_K^* = 1)$. Figure 9 reveals that this is not just a coincidence. It shows the θ-dependence of the momentum-space aspect ratio A_K for several trapping geometries for erbium atomic gases, ranging from a cigar-shaped trap, through a spherical, to a pancake-shaped trap. The azimuthal angle is kept constant at the value $\varphi = 0°$, as well

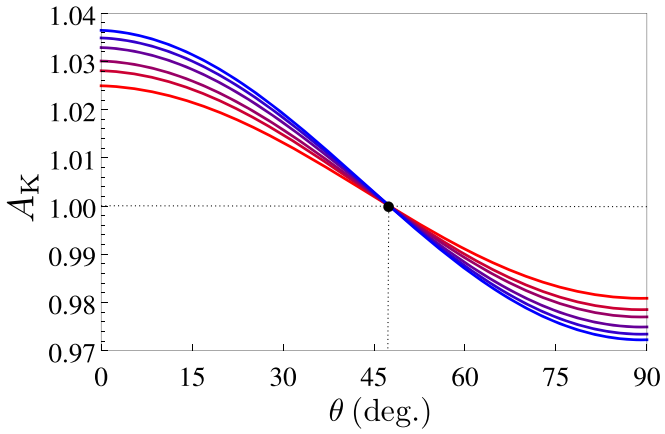

Figure 9. θ dependence of aspect ratio A_K for ^{167}Er for $\varphi = 0°, \alpha = 28°, N = 7 \times 10^4$ and $\omega_x = \omega_z = 500 \times 2\pi$ Hz. Different curves correspond to varying $\omega_y = n \times 100 \times 2\pi$ Hz, where $n \in \{1, 2, 3, 5, 7, 9\}$, bottom to top on the left hand side of the intersection, respectively. Intersection point is at $(\theta^*, A_K^*) = (48.56°, 1)$.

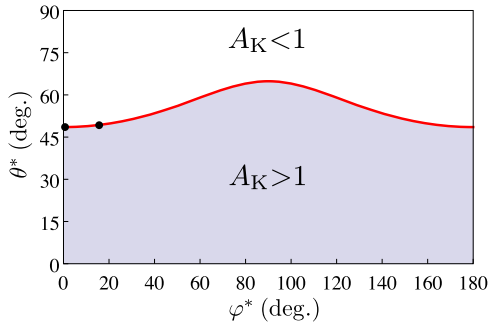

Figure 10. Relation between intersection angles θ^* and φ^* for $\alpha = 28°$, determined by (29): red solid line corresponds to $A_K^* = 1$, region below to $A_K > 1$, and region above to $A_K < 1$. Black dots correspond to intersection points identified in figures 9 and 8(a) for $\varphi = 0°$ and 14°, respectively.

as the trapping frequencies $\omega_x = \omega_z = 500 \times 2\pi$ Hz, while the frequency $\omega_y = n \times 100 \times 2\pi$ Hz is varied by changing the value $n \in \{1, 2, 3, 5, 7, 9\}$, which corresponds to the trap anisotropy $\lambda = 5/n$. The number of particles was fixed at $N = 7 \times 10^4$. We observe again that all curves intersect for $A_K^* = 1$, which suggests that this is a general rule. Indeed, if we take into account that $K_z' \geqslant K_x' > 0$, for $A_K^* = 1$ we can show from (25) that the following relation holds, which connects the intersection angles θ^* and φ^*:

$$\sin^2\theta^* = \frac{1}{1 + \cos^2\varphi^* \cos^2\alpha + \sin^2\varphi^* \sin^2\alpha}. \tag{29}$$

This result is universal, i.e., it is independent on other system parameters as the trap geometry, the number of particles, and the DDI strength. In other words, this intersection point is purely a consequence of the geometry, and for any orientation of the dipoles there exists an imaging angle such that the aspect ratio is given by $A_K = 1$, while the FS deformation Δ can be nontrivial and even can have a significant value. We note that for larger ε_{dd} values additional parameter-specific intersection points may appear for some geometries, but the intersection point for $A_K = 1$ is universal and always present.

To further illustrate this, in figure 10 we plot a diagram in the (θ^*, φ^*)-plane for $\alpha = 28°$, where the regions with $A_K > 1$ and $A_K < 1$ are delineated by a solid line defined by (29). The two black dots correspond to intersection points from figure 9 for $\varphi = 0°$ and from figure 8(a) for $\varphi = 14°$, respectively.

5. Conclusions

In conclusion, we have explored the ground-state properties of dipolar Fermi gases in elongated traps at zero temperature for an arbitrary orientation of the dipoles. By means of a Hartree–Fock mean-field theory with an appropriate ansatz for the Wigner function, we have shown that the ground-state FS is deformed into an ellipsoid, the main axis of which coincides with the orientation of the dipoles. We have then used this theory to

study effects of the dipoles' orientation, the particle number and the trap anisotropy on the deformation of the FS. We have found that the FS deformation is maximal when the dipoles point along the axis with the smallest trapping frequency and demonstrated this for two samples of different dipolar strengths, values of which are achievable with atomic erbium in one case and with polar molecules in the other case. Furthermore, for the erbium case we have observed that the angular dependence of the FS deformation is larger than the corresponding dependence on the trap anisotropy, and that both are less pronounced than the corresponding effect when the number of particles is varied. Note, however, that a stronger DDI may modify this behaviour.

We have established a relationship between the FS deformation and the momentum-space aspect ratio for a general system geometry, which is experimentally accessible by measuring the real-space aspect ratio during the TOF, if we assume ballistic expansion. We have performed new measurements on degenerate gases of atomic ^{167}Er in different trap geometries and found very good agreement, without any free fitting parameters. As an extension, using pure geometric considerations, we have shown that the FS deformation can have a nontrivial value even when the measured TOF real-space aspect ratio equals one. Furthermore, we have derived a relation between the orientation of the dipoles and the imaging direction for which the aspect ratio is always equal to one.

The theory for the ground-state properties of trapped Fermi gases of tilted dipoles presented here may be relevant for a precise calculation of the critical temperature for BCS pairing of dipolar fermions [56]. Furthermore, it can also serve as a basis for a further study of the system's dynamics, such as the TOF analysis and the low-lying excitations. Indeed, a proper comparison between theory and experiment for the finite-time real-space aspect ratio, to the best of our knowledge, is still lacking for an arbitrary geometry. These aspects of dipolar Fermi gases, whose understanding is highly relevant for current and future experiments, will be studied in a forthcoming publication.

Acknowledgments

We thank A Patscheider and D Petter for their help in the experimental measurements and for fruitful discussions. This work was supported in part by the Ministry of Education, Science and Technological Development of the Republic of Serbia under projects ON171017, BEC-L and DUDFG, by the German Academic and Exchange Service (DAAD) under project BEC-L, by the German Research Foundation (DFG) via the project PE 530/5-1 as well as the Collaborative Research Centers SFB/TR49 and SFB/TR185, and by the Austrian Agency for International Mobility and Cooperation in Education, Science and Research (OeAD) under project DUDFG. ARPL acknowledges financial support from the Brazilian Fundação Cearense de Apoio ao Desenvolvimento Científico e Tecnológico (Grant No. BP2-0107-00 129.02.00/15). The Innsbruck team gratefully acknowledges financial support from the European Research Council through the ERC Consolidator Grant RARE (Grant No. 681432), from the Austrian Science Fund (FWF): project I2790, and from the German Research Foundation (DFG) Research Unit FOR 2247. LC is supported within the Marie Curie project DipPhase (Grant No. 706809) of the EU H2020 programme. Numerical simulations were run on the PARADOX supercomputing facility at the Scientific Computing Laboratory of the Institute of Physics Belgrade.

Appendix A. Hartree energy

The Hartree term (13) can be written in terms of the Fourier transform of the potential according to

$$E_{\mathrm{dd}}^{\mathrm{D}} = \frac{1}{2}\int \frac{\mathrm{d}^3k''}{(2\pi)^3}\tilde{V}_{\mathrm{dd}}(\mathbf{k}'')\int \frac{\mathrm{d}^3k}{(2\pi)^3}\tilde{\nu}(-\mathbf{k}'',\,\mathbf{k})\int \frac{\mathrm{d}^3k'}{(2\pi)^3}\tilde{\nu}(\mathbf{k}'',\,\mathbf{k}'). \tag{A.1}$$

Defining $h(\mathbf{k}) = 1 - \sum_{ij} k_i \mathbb{B}_{ij} k_j$ as a suitable abbreviation for the momentum part of the argument of the Wigner function (5), the Fourier-transformed distribution function yields

$$\tilde{\nu}(-\mathbf{k}'',\,\mathbf{k}) = \frac{(2\pi)^{\frac{3}{2}}\bar{R}^3 h(\mathbf{k})^{\frac{3}{4}}\Theta[h(\mathbf{k})]}{(k_x''^2R_x^2 + k_y''^2R_y^2 + k_z''^2R_z^2)^{\frac{3}{4}}} J_{\frac{3}{2}}[h(\mathbf{k})^{\frac{1}{2}}(k_x''^2R_x^2 + k_y''^2R_y^2 + k_z''^2R_z^2)^{\frac{1}{2}}], \tag{A.2}$$

where J_a represents the Bessel function of the first kind. Then, after an algebraic substitution and switching into spherical coordinates, the integral yields

$$E_{\mathrm{dd}}^{\mathrm{D}} = \frac{\mu_0 m^2 \bar{R}^3 \bar{K}'^6}{48\pi^3} \int_0^{\pi} \mathrm{d}\vartheta \int_0^{2\pi} \mathrm{d}\phi \sin\vartheta \int_0^{\infty} \mathrm{d}u\, u^{-4} J_3^2(u)$$
$$\times \left[\frac{3\sin^2\theta\cos^2\varphi\sin^3\vartheta\cos^2\phi}{\cos^2\phi\sin^2\vartheta + (R_x/R_y)^2\sin^2\phi\sin^2\vartheta + (R_x/R_z)^2\cos^2\vartheta} \right.$$
$$+ \frac{3\sin^2\theta\sin^2\varphi\sin^3\vartheta\sin^2\phi}{(R_y/R_x)^2\cos^2\phi\sin^2\vartheta + \sin^2\phi\sin^2\vartheta + (R_y/R_z)^2\cos^2\vartheta}$$
$$\left. + \frac{3\cos^2\theta\cos^2\vartheta\sin\vartheta}{(R_z/R_x)^2\cos^2\phi\sin^2\vartheta + (R_z/R_y)^2\sin^2\phi\sin^2\vartheta + \cos^2\vartheta} - 1 \right]. \tag{A.3}$$

Subsequently, we apply [66, (6.574.2)] for the radial integral and make use of the anisotropy function described in appendix C, equations (C.3)–(C.5), so that the Hartree energy $E_{\mathrm{dd}}^{\mathrm{D}}$ yields

$$E_{\mathrm{dd}}^{\mathrm{D}} = -\frac{6N^2c_0}{\bar{R}^3}\left[1 - 3\sin^2\theta\cos^2\varphi f_{A1}\left(\frac{R_x}{R_z}, \frac{R_y}{R_z}\right)\right.$$
$$\left. - 3\sin^2\theta\sin^2\varphi f_{A2}\left(\frac{R_x}{R_z}, \frac{R_y}{R_z}\right) - 3\cos^2\theta f_{A3}\left(\frac{R_x}{R_z}, \frac{R_y}{R_z}\right)\right]. \tag{A.4}$$

Finally, the identities (C.9) lead to

$$E_{\mathrm{dd}}^{\mathrm{D}} = -\frac{6N^2c_0}{\bar{R}^3} f_{\mathrm{A}}\left(\frac{R_x}{R_z}, \frac{R_y}{R_z}, \theta, \varphi\right), \tag{A.5}$$

with the definition (16) for the generalised anisotropy function.

Appendix B. Fock energy

The Fock term can be rewritten in the following form

$$E_{\mathrm{dd}}^{\mathrm{E}} = -\frac{1}{2}\int \mathrm{d}^3x' \int \frac{\mathrm{d}^3k'}{(2\pi)^3} \int \frac{\mathrm{d}^3k''}{(2\pi)^3} \tilde{\bar{\nu}}(\mathbf{k}'', \mathbf{x}')\tilde{\nu}(-\mathbf{k}'', -\mathbf{x}')\tilde{V}_{\mathrm{dd}}(\mathbf{k}')\mathrm{e}^{\mathrm{i}\mathbf{x}'\cdot\mathbf{k}'}, \tag{B.1}$$

where $\bar{\nu}(\mathbf{k}', \mathbf{k})$ and $\tilde{\nu}(\mathbf{x}, \mathbf{x}')$ denote the Fourier transforms of $\nu(\mathbf{x}, \mathbf{k})$ with respect to the first and second variable, respectively. The first step is to calculate these two Fourier transforms of the Wigner function. The first of these two transforms has already been obtained in (A.2). Using this result, one gets

$$\tilde{\bar{\nu}}(-\mathbf{k}'', \mathbf{x}) = \int \frac{\mathrm{d}^3k}{(2\pi)^3}\mathrm{e}^{\mathrm{i}\mathbf{k}\cdot\mathbf{x}}\tilde{\nu}(-\mathbf{k}'', \mathbf{k}) = \int \frac{\mathrm{d}^3q}{(2\pi)^3}\mathrm{e}^{\mathrm{i}\mathbf{q}\cdot(\mathbb{R}^T\mathbf{x})}\tilde{\nu}(-\mathbf{k}'', \mathbb{R}\mathbf{q})$$
$$= \int \frac{\mathrm{d}^3q}{(2\pi)^{\frac{3}{2}}}\mathrm{e}^{\mathrm{i}\mathbf{q}\cdot\mathbf{c}} \frac{\bar{R}^3\Theta\left(1 - \sum_j \frac{q_j^2}{K_j'^2}\right)^{\frac{3}{4}}}{g(\mathbf{k}'')^{\frac{3}{4}}} \left(1 - \sum_l \frac{q_l^2}{K_l'^2}\right)^{\frac{3}{4}} J_{\frac{3}{2}}\left[\left(1 - \sum_m \frac{q_m^2}{K_m'^2}\right)^{\frac{1}{2}} g(\mathbf{k}'')^{\frac{1}{2}}\right], \tag{B.2}$$

where $g(\mathbf{k}'') = k_x''^2R_x^2 + k_y''^2R_y^2 + k_z''^2R_z^2$ and $\mathbf{c} = \mathbb{R}^T\mathbf{x}$. The three q-integrals will be treated separately, yet all in the same way. Hence, it is only necessary to compute one of them. With the use of the substitution $q_z = K_z'\sqrt{1 - \frac{q_x^2}{K_x'^2} - \frac{q_y^2}{K_y'^2}}\cos\vartheta$, one can rewrite (B.2) as

$$\tilde{\bar{\nu}}(-\mathbf{k}'', \mathbf{x}) = \frac{\bar{R}^3}{(2\pi)^{\frac{3}{2}}}\frac{2}{g(\mathbf{k})''^{\frac{3}{4}}} \int \mathrm{d}q_x\mathrm{d}q_y \mathrm{e}^{\mathrm{i}c_xq_x + \mathrm{i}c_yq_y}\Theta\left(1 - \frac{q_x^2}{K_x'^2} - \frac{q_y^2}{K_y'^2}\right)\left(1 - \frac{q_x^2}{K_x'^2} - \frac{q_y^2}{K_y'^2}\right)^{\frac{5}{4}}$$
$$\times \int_0^{\frac{\pi}{2}} \mathrm{d}\vartheta \sin^{\frac{5}{2}}\vartheta K_z' \cos\left(c_zK_z'\sqrt{1 - \frac{q_x^2}{K_x'^2} - \frac{q_y^2}{K_y'^2}}\cos\vartheta\right)$$
$$\times J_{\frac{3}{2}}\left[g(\mathbf{k}'')^{\frac{1}{2}}\left(1 - \frac{q_x^2}{K_x'^2} - \frac{q_y^2}{K_y'^2}\right)^{\frac{1}{2}}\sin\vartheta\right]. \tag{B.3}$$

After this substitution, the ϑ-integral can be calculated using [66, (6.688.2)]. The other two k-integrals can be treated in the same way. Then, the Fourier transform reads

$$\bar{\tilde{\nu}}(-\mathbf{k}'',\mathbf{x})=\frac{\bar{R}^3\bar{K}'^3}{[g(\mathbf{k}'')+c_z^2K_z'^2+c_y^2K_y'^2+c_x^2K_x'^2]^{\frac{3}{2}}}J_3\{[g(\mathbf{k}'')+c_z^2K_z'^2+c_y^2K_y'^2+c_x^2K_x'^2]^{\frac{1}{2}}\}. \tag{B.4}$$

It is clear that $\bar{\tilde{\nu}}(\mathbf{k}'',\mathbf{x})$ is an even function, which further simplifies the calculations. The next step is to calculate the $\mathbf{x}'$-integral in (B.1). To avoid a quadratic Bessel function, one can use the integral representation [66, (6.519.2.2)], which leads to an integral over a Bessel function

$$\begin{aligned}&J_3^2\{[c_x^2K_x'^2+c_y^2K_y'^2+c_z^2K_z'^2+g(\mathbf{k}'')]^{\frac{1}{2}}\}\\&=\frac{2}{\pi}\int_0^{\frac{\pi}{2}}\mathrm{d}tJ_6\{2\sin t[c_x^2K_x'^2+c_y^2K_y'^2+c_z^2K_z'^2+g(\mathbf{k}'')]^{\frac{1}{2}}\}.\end{aligned} \tag{B.5}$$

With this the $\mathbf{x}'$-integral becomes

$$\begin{aligned}&\int\mathrm{d}^3x'\bar{\tilde{\nu}}(\mathbf{k}'',\mathbf{x}')^2\mathrm{e}^{\mathrm{i}\mathbf{k}'\cdot\mathbf{x}'}=\int\mathrm{d}^3x''\bar{\tilde{\nu}}(\mathbf{k}'',\mathbb{R}\mathbf{x}'')^2\mathrm{e}^{\mathrm{i}\mathbf{k}'\cdot(\mathbb{R}\mathbf{x}'')}=\int\mathrm{d}^3x''\bar{\tilde{\nu}}(\mathbf{k}'',\mathbb{R}\mathbf{x}'')^2\mathrm{e}^{\mathrm{i}(\mathbb{R}^T\mathbf{k}')^T\cdot\mathbf{x}''}\\&=\int\mathrm{d}^3x''\frac{\bar{R}^6\bar{K}'^6\mathrm{e}^{\mathrm{i}\boldsymbol{\kappa}\cdot\mathbf{x}''}}{[x''^2K_x'^2+y''^2K_y'^2+z''^2K_z'^2+g(\mathbf{k}'')]^3}J_3^2\{[x''^2K_x'^2+y''^2K_y'^2+z''^2K_z'^2+g(\mathbf{k}'')]^{\frac{1}{2}}\}\\&=\int\mathrm{d}^3x''\frac{\bar{R}^6\bar{K}'^6\mathrm{e}^{\mathrm{i}\boldsymbol{\kappa}\cdot\mathbf{x}''}}{[x''^2K_x'^2+y''^2K_y'^2+z''^2K_z'^2+g(\mathbf{k}'')]^3}\\&\times\frac{2}{\pi}\int_0^{\frac{\pi}{2}}\mathrm{d}tJ_6\{2\sin t[x''^2K_x'^2+y''^2K_y'^2+z''^2K_z'^2+g(\mathbf{k}'')]^{\frac{1}{2}}\},\end{aligned}$$

where $\boldsymbol{\kappa}=\mathbb{R}^T\mathbf{k}'$. We treat the three integrals separately, starting with the z''-integral. After the substitution $u_z=z''K_z'$, we can use [66, (6.726.2)] to evaluate the integral over z''

$$\begin{aligned}&\bar{R}^6\bar{K}'^6\int\mathrm{d}x''\mathrm{d}y''\mathrm{e}^{\mathrm{i}\kappa_xx''+\mathrm{i}\kappa_yy''}\frac{4}{\pi K_z'}\int_0^{\frac{\pi}{2}}\mathrm{d}t\frac{\left(4\sin^2t-\frac{\kappa_z^2}{K_z'^2}\right)^{\frac{11}{4}}\Theta\left(2\sin t-\sqrt{\frac{\kappa_z^2}{K_z'^2}}\right)}{(2\sin t)^6[x''^2K_x'^2+y''^2K_y'^2+g(\mathbf{k}'')]^{\frac{11}{4}}}\\&\times\sqrt{\frac{\pi}{2}}J_{\frac{11}{2}}\left\{\left(4\sin^2t-\frac{\kappa_z^2}{K_z'^2}\right)^{\frac{1}{2}}[x''^2K_x'^2+y''^2K_y'^2+g(\mathbf{k}'')]^{\frac{1}{2}}\right\}.\end{aligned} \tag{B.6}$$

The other two integrals will be calculated in the same way. The solution of the $\mathbf{x}'$-integral reads

$$\begin{aligned}&\int\mathrm{d}^3x'\bar{\tilde{\nu}}(\mathbf{k}'',\mathbf{x}')^2\mathrm{e}^{\mathrm{i}\mathbf{k}'\cdot\mathbf{x}'}=\left(\frac{\pi}{2^7}\right)^{\frac{1}{2}}\bar{R}^6\bar{K}'^3\int_0^{\frac{\pi}{2}}\frac{\mathrm{d}t}{\sin^6t}\frac{\left(4\sin^2t-\frac{\kappa_z^2}{K_z'^2}-\frac{\kappa_y^2}{K_y'^2}-\frac{\kappa_x^2}{K_x'^2}\right)^{\frac{9}{4}}}{g(\mathbf{k}'')^{\frac{9}{4}}}\\&\times J_{\frac{9}{2}}\left[g(\mathbf{k}'')^{\frac{1}{2}}\left(4\sin^2t-\frac{\kappa_z^2}{K_z'^2}-\frac{\kappa_y^2}{K_y'^2}-\frac{\kappa_x^2}{K_x'^2}\right)^{\frac{1}{2}}\right]\Theta\left(2\sin t-\sqrt{\frac{\kappa_z^2}{K_z'^2}+\frac{\kappa_y^2}{K_y'^2}+\frac{\kappa_x^2}{K_x'^2}}\right).\end{aligned} \tag{B.7}$$

The next step is to integrate the $\mathbf{k}''$-integral. Using the underlying spherical symmetry, the calculation of this integral becomes relatively short. Indeed, substituting $u_i=k_i''R_i$ and then transforming these new integration variables into spherical coordinates, one can use [66, (6.561.17)], which leads to

$$\begin{aligned}&I(\mathbf{k}')=\int\mathrm{d}^3k''\int\mathrm{d}^3x'\bar{\tilde{\nu}}(\mathbf{k}'',\mathbf{x}')^2\mathrm{e}^{\mathrm{i}\mathbf{k}'\cdot\mathbf{x}'}=\frac{\pi^2\bar{R}^3\bar{K}'^3}{192}\int_0^{\frac{\pi}{2}}\frac{\mathrm{d}t}{\sin^6t}\\&\times\left(4\sin^2t-\frac{\kappa_z^2}{K_z'^2}-\frac{\kappa_y^2}{K_y'^2}-\frac{\kappa_x^2}{K_x'^2}\right)^3\Theta\left(2\sin t-\sqrt{\frac{\kappa_z^2}{K_z'^2}+\frac{\kappa_y^2}{K_y'^2}+\frac{\kappa_x^2}{K_x'^2}}\right).\end{aligned} \tag{B.8}$$

The last step of the calculation of the Fock term is to solve the k'-integral, and therefore we will again switch to another coordinate system $\mathbf{k}'=\mathbb{R}\mathbf{q}$ and use the Fourier transform of the interaction potential

$$E_{\rm dd}^{\rm E} = -\frac{1}{2(2\pi)^6}\int {\rm d}^3k' I(\mathbf{k}')\tilde{V}_{\rm dd}(\mathbf{k}') = -\frac{1}{2(2\pi)^6}\int {\rm d}^3q I(\mathbb{R}\mathbf{q})\tilde{V}_{\rm dd}(\mathbb{R}\mathbf{q})$$
$$= -\frac{\mu_0 m^2\bar{R}^3\bar{K}'^3}{73728\pi^4}\int {\rm d}^3q\int_0^{\frac{\pi}{2}}\frac{{\rm d}t}{\sin^6 t}\left(4\sin^2 t - \frac{q_z^2}{K_z'^2} - \frac{q_y^2}{K_y'^2} - \frac{q_x^2}{K_x'^2}\right)^3$$
$$\times\,\Theta\left(2\sin t - \sqrt{\frac{q_z^2}{K_z'^2} + \frac{q_y^2}{K_y'^2} + \frac{q_x^2}{K_x'^2}}\right)\left(\frac{3q_z^2}{q^2} - 1\right). \tag{B.9}$$

Using the substitution $u_i = q_i/K_i'$ and afterwards switching to spherical coordinates we get

$$E_{\rm dd}^{\rm E} = -\frac{\mu_0 m^2\bar{R}^3\bar{K}'^6}{73728\pi^4}\int_0^{2\pi}{\rm d}\phi\int_0^{\pi}{\rm d}\vartheta\int_0^{\frac{\pi}{2}}\frac{{\rm d}t}{\sin^6 t}\int_0^{2\sin t}{\rm d}u u^2(4\sin^2 t - u^2)^3$$
$$\times\left[3\frac{\cos^2\vartheta\sin\vartheta}{(K_x'/K_z')^2\cos^2\phi\sin^2\vartheta + (K_y'/K_z')^2\sin^2\phi\sin^2\vartheta + \cos^2\vartheta} - \sin\vartheta\right]. \tag{B.10}$$

The ϑ- and ϕ-integrals will lead to the anisotropy function, which is defined by (C.5) and (C.6), and the u-integral and t-integral can be solved without any difficulties. The solution of the Fock term reads

$$E_{\rm dd}^{\rm E} = \frac{6N^2c_0}{\bar{R}^3}\left[1 - 3f_{A3}\left(\frac{K_z'}{K_x'}, \frac{K_z'}{K_y'}\right)\right] = \frac{6N^2c_0}{\bar{R}^3}f\left(\frac{K_z'}{K_x'}, \frac{K_z'}{K_y'}\right). \tag{B.11}$$

Appendix C. Anisotropy function

Here we recall the definition of the usual anisotropy function [47]

$$f(x, y) = -\frac{1}{4\pi}\int_0^{2\pi}{\rm d}\phi\int_0^{\pi}{\rm d}\vartheta\sin\vartheta\left[\frac{3x^2y^2\cos^2\vartheta}{(y^2\cos^2\phi + x^2\sin^2\phi)\sin^2\vartheta + x^2y^2\cos^2\vartheta} - 1\right]$$
$$= 1 + 3xy\frac{E(\vartheta_x, \kappa) - F(\vartheta_x, \kappa)}{(1 - y^2)\sqrt{1 - x^2}}, \tag{C.1}$$

where $\vartheta_x = \arccos x$, $\vartheta_y = \arccos y$, $\kappa^2 = (1 - y^2)/(1 - x^2)$ are abbreviations and, $F(\varphi, k)$ is the elliptic integral of first kind and $E(\varphi, k)$ is the elliptic integral of second kind. Notice that

$$f(x, x) = f_s(x) \tag{C.2}$$

denotes the cylindrically symmetric anisotropy function [62, 67–69]. We, then, introduce some auxiliary functions

$$4\pi f_{\rm A1}(x, y) = \int_0^{2\pi}{\rm d}\phi\int_0^{\pi}{\rm d}\vartheta\frac{y^2\sin^3\vartheta\cos^2\phi}{y^2\cos^2\phi\sin^2\vartheta + x^2\sin^2\phi\sin^2\vartheta + x^2y^2\cos^2\vartheta}$$
$$= 4\pi\frac{y^2}{y^2 - x^2}\left[1 - \frac{x}{y}\frac{E(\vartheta_x, \kappa)}{\sqrt{1 - x^2}}\right], \tag{C.3}$$

$$4\pi f_{\rm A2}(x, y) = \int_0^{2\pi}{\rm d}\phi\int_0^{\pi}{\rm d}\vartheta\frac{x^2\sin^3\vartheta\sin^2\phi}{y^2\cos^2\phi\sin^2\vartheta + x^2\sin^2\phi\sin^2\vartheta + x^2y^2\cos^2\vartheta}$$
$$= 4\pi\frac{x^2}{x^2 - y^2}\left[1 - \frac{y}{x}\frac{E(\vartheta_y, \frac{1}{\kappa})}{\sqrt{1 - y^2}}\right], \tag{C.4}$$

$$4\pi f_{\rm A3}(x, y) = \int_0^{2\pi}{\rm d}\phi\int_0^{\pi}{\rm d}\vartheta\frac{x^2y^2\cos^2\vartheta\sin\vartheta}{y^2\cos^2\phi\sin^2\vartheta + x^2\sin^2\phi\sin^2\vartheta + x^2y^2\cos^2\vartheta}$$
$$= -4\pi xy\frac{E(\vartheta_x, \kappa) - F(\vartheta_x, \kappa)}{(1 - y^2)\sqrt{1 - x^2}}. \tag{C.5}$$

At this point, the following identities can be derived

$$f(x, y) = 1 - 3f_{\rm A3}(x, y), \tag{C.6}$$
$$f_{\rm A1}(x, y) = f_{\rm A3}(y/x, 1/x), \tag{C.7}$$
$$f_{\rm A2}(x, y) = f_{\rm A3}(x/y, 1/y), \tag{C.8}$$

$$\sum_{i=1,2,3} f_{Ai}(x, y) = 1. \tag{C.9}$$

Thus, finally, taking (C.6)–(C.8) into account, we have

$$\begin{aligned} f_{\mathrm{A}}(x, y, \theta, \varphi) &= 1 - 3\sin^2\theta\cos^2\varphi\, f_{A1}(x, y) - 3\sin^2\theta\sin^2\varphi\, f_{A2}(x, y) - 3\cos^2\theta\, f_{A3}(x, y) \\ &= \sin^2\theta\cos^2\varphi\, f\left(\frac{y}{x}, \frac{1}{x}\right) + \sin^2\theta\sin^2\varphi\, f\left(\frac{x}{y}, \frac{1}{y}\right) + \cos^2\theta\, f(x, y). \end{aligned} \tag{C.10}$$

Appendix D. Equations for variational parameters in momentum and real space

Here we present the respective equations for the variational parameters of the Wigner function ansätze, i.e., Thomas–Fermi radii and momenta, for all three considered scenarios in section 2, see figure 2.

D.1. Spherical scenario

The five variational parameters $(K_{\mathrm{F}}, R_i, \mu)$ are determined by minimising the grand-canonical potential $\Omega^{(1)}$, which leads to the following set of algebraic equations:

$$\mu = \frac{\hbar^2 K_{\mathrm{F}}^2}{8M}, \tag{D.1}$$

$$\omega_x^2 R_x^2 + \frac{48Nc_0}{M\bar{R}^3}\left[f_{\mathrm{A}}\left(\frac{R_x}{R_z}, \frac{R_y}{R_z}, \theta, \varphi\right) - R_x\partial_{R_x} f_{\mathrm{A}}\left(\frac{R_x}{R_z}, \frac{R_y}{R_z}, \theta, \varphi\right)\right] - \frac{8\mu}{M} = 0, \tag{D.2}$$

$$\omega_y^2 R_y^2 + \frac{48Nc_0}{M\bar{R}^3}\left[f_{\mathrm{A}}\left(\frac{R_x}{R_z}, \frac{R_y}{R_z}, \theta, \varphi\right) - R_y\partial_{R_y} f_{\mathrm{A}}\left(\frac{R_x}{R_z}, \frac{R_y}{R_z}, \theta, \varphi\right)\right] - \frac{8\mu}{M} = 0, \tag{D.3}$$

$$\omega_z^2 R_z^2 + \frac{48Nc_0}{M\bar{R}^3}\left[f_{\mathrm{A}}\left(\frac{R_x}{R_z}, \frac{R_y}{R_z}, \theta, \varphi\right) - R_z\partial_{R_z} f_{\mathrm{A}}\left(\frac{R_x}{R_z}, \frac{R_y}{R_z}, \theta, \varphi\right)\right] - \frac{8\mu}{M} = 0, \tag{D.4}$$

$$N = \frac{1}{48}\bar{R}^3 K_{\mathrm{F}}^3. \tag{D.5}$$

Note that (D.5) represents the particle-number conservation constraint, which is the special case of (10) for $K_x = K_y = K_z = K_{\mathrm{F}}$.

D.2. On-axis scenario

The seven variational parameters (K_i, R_i, μ) are determined by minimising the grand-canonical potential $\Omega^{(2)}$, which leads to the following set of algebraic equations:

$$\frac{\hbar^2 K_x^2}{2M} + \frac{24Nc_0}{\bar{R}^3} K_x\partial_{K_x} f_{\mathrm{A}}\left(\frac{K_z}{K_x}, \frac{K_z}{K_y}, \theta, \varphi\right) - 4\mu = 0, \tag{D.6}$$

$$\frac{\hbar^2 K_y^2}{2M} + \frac{24Nc_0}{\bar{R}^3} K_y\partial_{K_y} f_{\mathrm{A}}\left(\frac{K_z}{K_x}, \frac{K_z}{K_y}, \theta, \varphi\right) - 4\mu = 0, \tag{D.7}$$

$$\frac{\hbar^2 K_z^2}{2M} + \frac{24Nc_0}{\bar{R}^3} K_z\partial_{K_z} f_{\mathrm{A}}\left(\frac{K_z}{K_x}, \frac{K_z}{K_y}, \theta, \varphi\right) - 4\mu = 0, \tag{D.8}$$

$$\omega_x^2 R_x^2 + \frac{48Nc_0}{M\bar{R}^3}\left[f_{\mathrm{A}}\left(\frac{R_x}{R_z}, \frac{R_y}{R_z}, \theta, \varphi\right) - f_{\mathrm{A}}\left(\frac{K_z}{K_x}, \frac{K_z}{K_y}, \theta, \varphi\right) - R_x\partial_{R_x} f_{\mathrm{A}}\left(\frac{R_x}{R_z}, \frac{R_y}{R_z}, \theta, \varphi\right)\right] - \frac{8\mu}{M} = 0, \tag{D.9}$$

$$\omega_y^2 R_y^2 + \frac{48Nc_0}{M\bar{R}^3}\left[f_{\mathrm{A}}\left(\frac{R_x}{R_z}, \frac{R_y}{R_z}, \theta, \varphi\right) - f_{\mathrm{A}}\left(\frac{K_z}{K_x}, \frac{K_z}{K_y}, \theta, \varphi\right) - R_y\partial_{R_y} f_{\mathrm{A}}\left(\frac{R_x}{R_z}, \frac{R_y}{R_z}, \theta, \varphi\right)\right] - \frac{8\mu}{M} = 0, \tag{D.10}$$

$$\omega_z^2 R_z^2 + \frac{48Nc_0}{M\bar{R}^3}\left[f_{\mathrm{A}}\left(\frac{R_x}{R_z}, \frac{R_y}{R_z}, \theta, \varphi\right) - f_{\mathrm{A}}\left(\frac{K_z}{K_x}, \frac{K_z}{K_y}, \theta, \varphi\right) - R_z\partial_{R_z} f_{\mathrm{A}}\left(\frac{R_x}{R_z}, \frac{R_y}{R_z}, \theta, \varphi\right)\right] - \frac{8\mu}{M} = 0, \tag{D.11}$$

$$N = \frac{1}{48}\bar{R}^3\bar{K}^3. \tag{D.12}$$

Similarly as in the spherical scenario, (D.12) coincides with the particle-number conservation equation (10).

D.3. Off-axis scenario

The seven variational parameters (K_i', R_i, μ) are determined by minimising the grand-canonical potential $\Omega^{(3)}$, which leads to the following set of algebraic equations:

$$\frac{\hbar^2 K_x'^2}{2M} + \frac{24Nc_0}{\bar{R}^3} K_x' \partial_{K_x'} f\left(\frac{K_z'}{K_x'}, \frac{K_z'}{K_y'}\right) - 4\mu = 0, \tag{D.13}$$

$$\frac{\hbar^2 K_y'^2}{2M} + \frac{24Nc_0}{\bar{R}^3} K_y' \partial_{K_y'} f\left(\frac{K_z'}{K_x'}, \frac{K_z'}{K_y'}\right) - 4\mu = 0, \tag{D.14}$$

$$\frac{\hbar^2 K_z'^2}{2M} + \frac{24Nc_0}{\bar{R}^3} K_z' \partial_{K_z'} f\left(\frac{K_z'}{K_x'}, \frac{K_z'}{K_y'}\right) - 4\mu = 0, \tag{D.15}$$

$$\omega_x^2 R_x^2 + \frac{48Nc_0}{M\bar{R}^3}\left[f_{\mathrm{A}}\left(\frac{R_x}{R_z}, \frac{R_y}{R_z}, \theta, \varphi\right) - f\left(\frac{K_z'}{K_x'}, \frac{K_z'}{K_y'}\right) - R_x \partial_{R_x} f_{\mathrm{A}}\left(\frac{R_x}{R_z}, \frac{R_y}{R_z}, \theta, \varphi\right)\right] - \frac{8\mu}{M} = 0, \tag{D.16}$$

$$\omega_y^2 R_y^2 + \frac{48Nc_0}{M\bar{R}^3}\left[f_{\mathrm{A}}\left(\frac{R_x}{R_z}, \frac{R_y}{R_z}, \theta, \varphi\right) - f\left(\frac{K_z'}{K_x'}, \frac{K_z'}{K_y'}\right) - R_y \partial_{R_y} f_{\mathrm{A}}\left(\frac{R_x}{R_z}, \frac{R_y}{R_z}, \theta, \varphi\right)\right] - \frac{8\mu}{M} = 0, \tag{D.17}$$

$$\omega_z^2 R_z^2 + \frac{48Nc_0}{M\bar{R}^3}\left[f_{\mathrm{A}}\left(\frac{R_x}{R_z}, \frac{R_y}{R_z}, \theta, \varphi\right) - f\left(\frac{K_z'}{K_x'}, \frac{K_z'}{K_y'}\right) - R_z \partial_{R_z} f_{\mathrm{A}}\left(\frac{R_x}{R_z}, \frac{R_y}{R_z}, \theta, \varphi\right)\right] - \frac{8\mu}{M} = 0, \tag{D.18}$$

$$N = \frac{1}{48}\bar{R}^3 \bar{K}'^3. \tag{D.19}$$

As before, (D.19) coincides with the particle-number conservation equation (10).

Due to the symmetry of the anisotropy function $f(x, y) = f(y, x)$, it follows from (D.13) and (D.14) that $K_x' = K_y'$, i.e., that the FS is cylindrically symmetric with respect to the dipoles' orientation. Additionally, in close analogy with the special case when the dipoles are aligned with one of the trapping axes [44–47], the three equations (D.13)–(D.15) can be rewritten in the following form:

$$K_x' = K_y', \tag{D.20}$$

$$K_z'^2 - K_x'^2 = \frac{144MNc_0}{\hbar^2 \bar{R}^3}\left[1 + \frac{(2K_x'^2 + K_z'^2) f_{\mathrm{s}}\left(\frac{K_z'}{K_x'}\right)}{2(K_z'^2 - K_x'^2)}\right], \tag{D.21}$$

$$\mu = \frac{1}{12}\sum_j \frac{\hbar^2 K_j'^2}{2M}. \tag{D.22}$$

ORCID iDs

Vladimir Veljić https://orcid.org/0000-0001-9889-7060
Aristeu R P Lima https://orcid.org/0000-0001-6171-2595
Lauriane Chomaz https://orcid.org/0000-0001-7196-5721
Simon Baier https://orcid.org/0000-0002-2840-5590
Manfred J Mark https://orcid.org/0000-0001-8157-4716
Antun Balaž https://orcid.org/0000-0002-5435-1688

References

[1] Griesmaier A, Werner J, Hensler S, Stuhler J and Pfau T 2005 *Phys. Rev. Lett.* **94** 160401
[2] Stuhler J, Griesmaier A, Koch T, Fattori M, Pfau T, Giovanazzi S, Pedri P and Santos L 2005 *Phys. Rev. Lett.* **95** 150406
[3] Baranov M 2008 *Phys. Rep.* **464** 71
[4] Lahaye T, Menotti C, Santos L, Lewenstein M and Pfau T 2009 *Rep. Prog. Phys.* **72** 126401
[5] Baranov M A, Dalmonte M, Pupillo G and Zoller P 2012 *Chem. Rev.* **112** 5012
[6] Lu M, Youn S H and Lev B L 2010 *Phys. Rev. Lett.* **104** 063001
[7] Aikawa K, Frisch A, Mark M, Baier S, Rietzler A, Grimm R and Ferlaino F 2012 *Phys. Rev. Lett.* **108** 210401
[8] Kadau H, Schmitt M, Wenzel M, Wink C, Maier T, Ferrier-Barbut I and Pfau T 2016 *Nature* **530** 194
[9] Ferrier-Barbut I, Kadau H, Schmitt M, Wenzel M and Pfau T 2016 *Phys. Rev. Lett.* **116** 215301
[10] Chomaz L, Baier S, Petter D, Mark M J, Wächtler F, Santos L and Ferlaino F 2016 *Phys. Rev.* X **6** 041039
[11] Schmitt M, Wenzel M, Böttcher F, Ferrier-Barbut I and Pfau T 2016 *Nature* **539** 259

[12] Chomaz L, van Bijnen R M W, Petter D, Faraoni G, Baier S, Hendrik Becher J, Mark M J, Wächtler F, Santos L and Ferlaino F 2018 *Nat. Phys.* **14** 442
[13] Muruganandam P and Adhikari S 2009 *Comput. Phys. Commun.* **180** 1888
[14] Vudragović D, Vidanović I, Balaž A, Muruganandam P and Adhikari S K 2012 *Comput. Phys. Commun.* **183** 2021
[15] Kumar R K, Young-S L E, Vudragović D, Balaž A, Muruganandam P and Adhikari S K 2015 *Comput. Phys. Commun.* **195** 117
[16] Lončar V, Balaž A, Bogojević A, Škrbić S, Muruganandam P and Adhikari S K 2016 *Comput. Phys. Commun.* **200** 406
[17] Lončar V, Young-S L E, Škrbić S, Muruganandam P, Adhikari S K and Balaž A 2016 *Comput. Phys. Commun.* **209** 190
[18] Fedorov A K, Kurbakov I L, Shchadilova Y E and Lozovik Yu E 2014 *Phys. Rev.* A **90** 043616
[19] Fedorov A K, Kurbakov I L and Lozovik Yu E 2014 *Phys. Rev.* B **90** 165430
[20] Mishra C and Nath R 2016 *Phys. Rev.* A **94** 033633
[21] Lima A R P and Pelster A 2011 *Phys. Rev.* A **84** 041604(R)
[22] Lima A R P and Pelster A 2012 *Phys. Rev.* A **86** 063609
[23] Pastukhov V 2017 *Phys. Rev.* A **95** 023614
[24] Xi K T and Saito H 2016 *Phys. Rev.* A **93** 011604
[25] Wächtler F and Santos L 2016 *Phys. Rev.* A **93** 061603
[26] Baillie D, Wilson R M, Bisset R N and Blakie P B 2016 *Phys. Rev.* A **94** 021602
[27] Wächtler F and Santos L 2016 *Phys. Rev.* A **94** 043618
[28] Bisset R N, Wilson R M, Baillie D and Blakie P B 2016 *Phys. Rev.* A **94** 033619
[29] Baillie D, Wilson R M and Blakie P B 2017 *Phys. Rev. Lett.* **119** 255302
[30] Blakie P B 2016 *Phys. Rev.* A **93** 033644
[31] Lu M, Burdick N Q and Lev B L 2012 *Phys. Rev. Lett.* **108** 215301
[32] Aikawa K, Frisch A, Mark M, Baier S, Grimm R and Ferlaino F 2014 *Phys. Rev. Lett.* **112** 010404
[33] Naylor B, Reigue A, Marechal E, Gorceix O, Laburthe-Tolra B and Vernac L 2015 *Phys. Rev.* A **91** 011603(R)
[34] Bohn J L, Cavagnero M and Ticknor C 2009 *New J. Phys.* **11** 055039
[35] Aikawa K, Frisch A, Mark M, Baier S, Grimm R, Bohn J L, Jin D S, Bruun G M and Ferlaino F 2014 *Phys. Rev. Lett.* **113** 263201
[36] Burdick N Q, Baumann K, Tang Y, Lu M and Lev B L 2015 *Phys. Rev. Lett.* **114** 023201
[37] Aikawa K, Baier S, Frisch A, Mark M, Ravensbergen C and Ferlaino F 2014 *Science* **345** 1484
[38] Miyakawa T, Sogo T and Pu H 2008 *Phys. Rev.* A **77** 061603
[39] Zhang J N, Qiu R Z, He L and Yi S 2011 *Phys. Rev.* A **83** 053628
[40] Baillie D and Blakie P B 2012 *Phys. Rev.* A **86** 023605
[41] He L, Zhang J N, Zhang Y and Yi S 2008 *Phys. Rev.* A **77** 031605
[42] Sogo T, He L, Miyakawa T, Yi S, Lu H and Pu H 2009 *New J. Phys.* **11** 055017
[43] Sogo T, He L, Miyakawa T, Yi S, Lu H and Pu H 2010 *New J. Phys.* **12** 079801
[44] Lima A R P and Pelster A 2010 *Phys. Rev.* A **81** 021606(R)
[45] Lima A R P and Pelster A 2010 *Phys. Rev.* A **81** 063629
[46] Veljić V, Balaž A and Pelster A 2017 *Phys. Rev.* A **95** 053635
[47] Wächtler F, Lima A R P and Pelster A 2017 *Phys. Rev.* A **96** 043608
[48] Baarsma J E and Törmä P 2016 arXiv:1612.07953
[49] van Loon E G C P, Katsnelson M I, Chomaz L and Lemeshko M 2016 *Phys. Rev.* B **93** 195145
[50] Góral K, Englert B G and Rzążewski K 2001 *Phys. Rev.* A **63** 033606
[51] Ni K K, Ospelkaus S, de Miranda M H G, Pe'er A, Neyenhuis B, Zirbel J J, Kotochigova S, Julienne P S, Jin D S and Ye J 2008 *Science* **322** 231
[52] Vitanov N V, Rangelov A A, Shore B W and Bergmann K 2017 *Rev. Mod. Phys.* **89** 015006
[53] Park J W, Will S A and Zwierlein M W 2015 *Phys. Rev. Lett.* **114** 205302
[54] Moses S A, Covey J P, Miecnikowski M T, Yan B, Gadway B, Ye J and Jin D S 2015 *Science* **350** 659
[55] Frisch A, Mark M, Aikawa K, Baier S, Grimm R, Petrov A, Kotochigova S, Quéméner G, Lepers M, Dulieu O and Ferlaino F 2015 *Phys. Rev. Lett.* **115** 203201
[56] Baranov M A, Dobrek Ł and Lewenstein M 2004 *New J. Phys.* **6** 198
[57] Wenzel M, Böttcher F, Langen T, Ferrier-Barbut I and Pfau T 2017 *Phys. Rev.* A **96** 053630
[58] Góral K, Rzążewski K and Pfau T 2000 *Phys. Rev.* A **61** 051601
[59] Zhang J-N and Yi S 2009 *Phys. Rev.* A **80** 053614
[60] Ronen S and Bohn J L 2010 *Phys. Rev.* A **81** 033601
[61] Giovanazzi S, Pedri P, Santos L, Griesmaier A, Fattori M, Koch T, Stuhler J and Pfau T 2006 *Phys. Rev.* A **74** 013621
[62] Yi S and You L 2001 *Phys. Rev.* A **63** 053607
[63] Stuhler J, Griesmaier A, Koch T, Fattori M and Pfau T 2007 *J. Magn. Magn. Mater.* **316** 429
[64] Howe K, Lima A R P and Pelster A 2009 *Eur. Phys. J.* D **54** 667
[65] Baillie D and Blakie P B 2012 *Phys. Rev.* A **86** 023605
[66] Gradshteyn I S and Ryzhik I M 2007 *Table of Integrals, Series, and Products* 7th edn (Amsterdam: Elsevier)
[67] O'Dell D H J, Giovanazzi S and Eberlein C 2004 *Phys. Rev. Lett.* **92** 250401
[68] Glaum K, Pelster A, Kleinert H and Pfau T 2007 *Phys. Rev. Lett.* **98** 080407
[69] Glaum K and Pelster A 2007 *Phys. Rev.* A **76** 023604

Time-of-flight expansion of trapped dipolar Fermi gases: From the collisionless to the hydrodynamic regime

Vladimir Veljić* and Antun Balaž†
Scientific Computing Laboratory, Center for the Study of Complex Systems, Institute of Physics Belgrade, University of Belgrade, Pregrevica 118, 11080 Belgrade, Serbia

Axel Pelster‡
Physics Department and Research Center Optimas, Technical University of Kaiserslautern, Erwin-Schrödinger Strasse 46, 67663 Kaiserslautern, Germany

(Received 19 December 2016; published 26 May 2017)

A recent time-of-flight (TOF) expansion experiment with polarized fermionic erbium atoms measured a Fermi surface deformation from a sphere to an ellipsoid due to dipole-dipole interaction, thus confirming previous theoretical predictions. Here we perform a systematic study of the ground-state properties and TOF dynamics for trapped dipolar Fermi gases from the collisionless to the hydrodynamic regime at zero temperature. To this end, we solve analytically the underlying Boltzmann-Vlasov equation within the relaxation-time approximation in the vicinity of equilibrium by using a suitable rescaling of the equilibrium distribution. The resulting ordinary differential equations for the respective scaling parameters are then solved numerically for experimentally realistic parameters and relaxation times that correspond to the collisionless, collisional, and hydrodynamic regimes. The equations for the collisional regime are first solved in the approximation of a fixed relaxation time, and then this approach is extended to include a self-consistent determination of the relaxation time. The presented analytical and numerical results are relevant for a detailed quantitative understanding of ongoing experiments and the design of future experiments with ultracold fermionic dipolar atoms and molecules. In particular, the obtained results are relevant for systems with strong dipole-dipole interaction, which turn out to affect significantly the aspect ratios during the TOF expansion.

DOI: 10.1103/PhysRevA.95.053635

I. INTRODUCTION

Atomic and molecular ultracold gases offer many advantages for studying quantum phenomena, especially within the realm of many-body physics, due to the high degree of tunability of interatomic interactions [1,2]. In particular, dipolar quantum gases of atoms and molecules have received much attention in recent years, as the anisotropic and long-range nature of the magnetic or electric dipole-dipole interaction (DDI) gives rise to a rich spectrum of properties in such systems [3–15]. Such systems include those made up of ultracold atoms, as well as those consisting of heteronuclear molecules with large dipole-dipole interactions. Furthermore, in the recent theoretical and experimental research [16] an interesting kind of strongly dipolar quantum gas was introduced. These are weakly bound polar molecules produced from atoms with large magnetic dipole moments, such as erbium and other lanthanides. These molecules can have a very large magnetic moment, which amounts to twice that of its individual atoms [17].

In 2005, an anisotropic deformation of the expanding dipolar bosonic chromium condensate due to DDI was observed [18]. In the recent experiment [19], also the Rosensweig instability was detected in a ^{164}Dy Bose-Einstein condensate, which represents a quantum ferrofluid due to the large atomic magnetic dipole moments. Namely, after a sudden decrease of the scattering length, the dipolar quantum gas creates self-ordered surface structures in the form of droplet crystals, which can only be understood by taking into account DDI [20–25] and the corresponding quantum fluctuations [26–37].

For dipolar Fermi gases, it was predicted that the long-range and anisotropic DDI leads in equilibrium to an anisotropic deformation of the Fermi surface from a sphere to an ellipsoid [38]. A recent time-of-flight (TOF) expansion experiment has now unambiguously detected such an ellipsoidal Fermi surface (FS) deformation in a dipolar quantum gas of fermionic erbium atoms, which turns out to be of the order of a few percent [39]. Within the Hartree-Fock mean-field theory for a many-body system, first-order contributions of DDI to the total energy of the system taken into account are in terms of both the Hartree direct interaction and the Fock exchange interaction [38,40–46]. In the case of a Fermi gas with isotropic interaction, the Hartree and the Fock interactions cancel out [38], thus leading to a spherically symmetric FS. But in the case of a Fermi gas with anisotropic DDI, the Hartree term gives rise to a distortion in real space [47], whereas the Fock term gives rise to a distortion in momentum space, i.e., to an ellipsoidal deformation of the Fermi sphere. Note in this context that the Fock exchange term in dipolar Fermi gases is the consequence of a combined effect of the DDI and the Pauli exclusion principle. In the current experimentally relevant range of dipolar interactions, the theory beyond Hartree-Fock, where the total energy is determined up to second order in the DDI, yields only small differences, which cannot yet be resolved experimentally. Thus, the Hartree-Fock mean-field approximation yields already quantitatively accurate results for present-day experiments [48–50].

*vladimir.veljic@ipb.ac.rs
†antun.balaz@ipb.ac.rs
‡axel.pelster@physik.uni-kl.de

The investigations of collective oscillations and TOF dynamics of dipolar Fermi gases have so far focused on either the collisionless (CL) regime [40–42], where collisions can be neglected, or on the hydrodynamic (HD) regime [44,45], where collisions occur so often that local equilibrium can be assumed. Wächtler *et al.* [46] recently studied even the behavior of collective oscillations when the system undergoes a crossover from one regime to the other.

Motivated by the experimental observation of the ellipsoidal FS deformation in the TOF experiment [39], we continue here the analytical analysis along the lines of Ref. [46] and investigate in detail the expansion dynamics for the collisional regime, which represents the transition zone between the limiting CL and HD regimes. We also extend previous approaches based on the relaxation-time approximation by introducing a self-consistently determined relaxation time, and study how this quantitatively affects the TOF dynamics.

The paper is structured as follows. In Sec. II, we introduce our notation and summarize recent experiments on atomic and molecular dipolar Fermi gases. In Sec. III, we analyze the global equilibrium of the system by minimizing the Hartree-Fock total energy in order to obtain the Thomas-Fermi radii and momenta. Afterwards, in order to study the dynamics, in Sec. IV we follow Ref. [46] and introduce the Boltzmann-Vlasov equation for dipolar Fermi gases as well as an approximative solution, which is based on a suitable rescaling ansatz for the equilibrium Wigner function. In Sec. V, we study in detail the TOF expansion dynamics of an initially trapped Fermi gas. To this end, we present our analytical and numerical results of the TOF analysis all the way from the collisionless to the hydrodynamic regime and reveal how the expanding cloud bears the signature of the underlying DDI. Finally, Sec. VI gathers our concluding remarks and gives an outlook for future research.

II. ATOMIC AND MOLECULAR DIPOLAR FERMI GASES

We consider a trapped ultracold quantum degenerate dipolar gas of single-component fermions of mass M and magnetic dipole moment $\mathbf{m}$ or electric dipole moment $\mathbf{d}$ at zero temperature. The system is then described by the second-quantized Hamiltonian

$$\hat{H} = \int d\mathbf{r}\, \hat{\Psi}^\dagger(\mathbf{r})\left[-\frac{\hbar^2}{2M}\nabla^2 + V(\mathbf{r})\right]\hat{\Psi}(\mathbf{r}) + \frac{1}{2}\iint d\mathbf{r}\, d\mathbf{r}'\, \hat{\Psi}^\dagger(\mathbf{r}')\hat{\Psi}^\dagger(\mathbf{r})V_{\mathrm{int}}(\mathbf{r}-\mathbf{r}')\hat{\Psi}(\mathbf{r})\hat{\Psi}(\mathbf{r}'). \quad (1)$$

Since the Pauli exclusion principle inhibits contact interaction, the long-range DDI between the polarized fermionic point dipoles is dominant. It is described by

$$V_{\mathrm{int}}(\mathbf{r}) = \frac{C_{\mathrm{dd}}}{4\pi|\mathbf{r}|^3}(1-3\cos^2\vartheta), \quad (2)$$

where $\mathbf{r}$ denotes the relative position between the dipoles, ϑ stands for the angle between $\mathbf{r}$ and the polarization axis of the dipoles, and C_{dd} represents the dipolar interaction strength, which depends on the nature of the dipoles. Namely, for electric dipoles it is defined as $C^e_{\mathrm{dd}} = d^2/\varepsilon_0$, where ε_0 is the vacuum permittivity, while for magnetic dipoles one has $C^m_{\mathrm{dd}} = \mu_0 m^2$, where μ_0 is the vacuum permeability. Magnetic dipolar moments are usually measured in units of Bohr magneton ($\mu_{\mathrm{B}} = 9.27401\times10^{-24}\,\mathrm{JT}^{-1}$), and electric dipolar moments in units of debye ($\mathrm{D} = 3.33564\times10^{-30}$ cm). Note that the DDI of polar molecules is about 10^4 times stronger than that of dipolar atoms, as $C^e_{\mathrm{dd}}/C^m_{\mathrm{dd}} \sim \alpha_S^{-2}$, with $\alpha_S = 7.297\times10^{-3}$ being the Sommerfeld fine-structure constant.

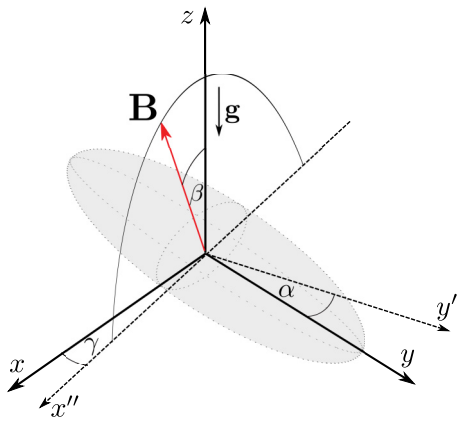

FIG. 1. Schematic illustration of the geometry in the Innsbruck experiment with ^{167}Er [39]. Axes x, y, z correspond to trap axes, while the orientation of the magnetic field $\mathbf{B}$ and the atomic dipoles is determined by spherical coordinates β and γ. Earth's gravitational field is parallel to the z axis, while the imaging axis is denoted by y', lies in the xy plane, and forms an angle α with y axis.

Due to the anisotropy in the dipolar interaction potential (2), dipolar Fermi gases tend to be stretched along the polarization direction, since this leads to a lower total energy. Here, we consider the parameters of a recent Innsbruck experiment [39] performed with the fermionic erbium atoms ^{167}Er in the collisionless regime, which are confined into a three-dimensional optical dipole trap with frequencies $(\omega_x,\omega_y,\omega_z) = (579, 91, 611)\times2\pi$ Hz. It contained $N = 7\times10^4$ atoms at a temperature T of $0.18\,T_{\mathrm{F}}$, with the Fermi temperature being $T_{\mathrm{F}} = 1.1\,\mu$K. The underlying geometry of the experiment is depicted in Fig. 1. Gravity is oriented along the z direction. The atomic cloud is imaged along the y' axis, which forms an angle $\alpha = 28^\circ$ with respect to the y axis. The magnetic field $\mathbf{B}$ forms an angle β with the z axis and lies in the $x''z$ plane, which is rotated for an angle $\gamma = 14^\circ$ with respect to the xz plane. In the following, we restrict ourselves to the general geometry of the anisotropic trap, where the dipoles are oriented in the direction of one of the trap axes, which reflects the experimental situation at the two limiting cases $\beta = 0^\circ$ and $\beta = 90^\circ$.

Previous theoretical works have predicted that the degree of deformation of the FS depends on the Fermi energy and the strength of the dipole moment [38,44–46]; therefore, we use a relative interaction strength of the DDI when comparing its effect on different species of ultracold Fermi gases. The relative interaction strength is given by

$$\epsilon_{\mathrm{dd}} = \frac{C_{\mathrm{dd}}}{4\pi}\sqrt{\frac{M^3\bar{\omega}}{\hbar^5}}N^{1/6}, \quad (3)$$

where $\bar{\omega} = (\omega_x\omega_y\omega_z)^{1/3}$ denotes the geometric mean of the trap frequencies.

The available dipolar Fermi gases in current ultracold experiments are listed in Table I, together with the maximal

TABLE I. Maximal values of dipole moments (m for species with a magnetic dipole and d for species with an electric dipole) and relative interaction strengths of fermionic atoms and molecules currently used in ultracold experiments, calculated according to Eq. (3) using the trap parameters and particle number given in the text. Note that the electric dipole moments d of molecular species ^{23}Na ^{40}K and ^{40}K ^{87}Rb can be tuned to smaller values by using an external electric field.

Gas	^{53}Cr [51]	^{167}Er [52]	^{161}Dy [53]	^{167}Er ^{168}Er [16]	^{23}Na ^{40}K [54]	^{40}K ^{87}Rb [55]
m/d	$6\,\mu_B$	$7\,\mu_B$	$10\,\mu_B$	$14\,\mu_B$	0.8 D	0.566 D
ϵ_{dd}	0.02	0.15	0.30	1.76	5.44	7.77

values of their dipole moments and relative interaction strengths, considering the trap parameters and particle number given above. A quantum degenerate Fermi gas of the strongly magnetic atoms of dysprosium was produced in 2012 [53]. Later on, a degenerate Fermi gas of erbium atoms [52] and molecules [16] was also realized. A dipolar Fermi sea of degenerate ^{53}Cr, together with a BEC of ^{52}Cr, was produced in 2015 [51]. A few years ago, a molecular dipolar gas of ^{40}K ^{87}Rb was realized using a single step of STIRAP [56] (stimulated Raman adiabatic passage) with two-frequency laser irradiation [55], and with the same technique an ultracold dipolar gas of fermionic molecules of ^{23}Na ^{40}K was created in a recent experiment [54,57]. The same technique can be also used for thermal [58] and ultracold dipolar Bose gases [59] of heteronuclear molecules.

We will consider the experimentally available range of relative strengths of the DDI and atom or molecule species given in Table I in the following sections. Therefore, the presented results are directly applicable to current and future experiments.

III. GLOBAL EQUILIBRIUM

A quantum many-body system can be described in terms of a Wigner function $\nu = \nu(\mathbf{r},\mathbf{k},t)$, as it represents the Wigner-Weyl transform of the density matrix of the system and is equivalent to a quantum-mechanical wave function [60]. The Wigner function is a quasiprobability distribution function, and integrating it over the space or the momentum variables leads to the respective probability distribution functions. The quantum-mechanical expectation values of observables [61–65] can be obtained as their phase-space averages, weighted by the Wigner function.

Considering a trapped ultracold dipolar Fermi gas, the equilibrium distribution function in the phase space will rapidly decrease to zero outside a certain closed surface, due to a combined effect of the Pauli exclusion principle, which is responsible for a formation of the FS in the momentum space and the trapping in real space. Therefore, in order to model the global equilibrium distribution of the dipolar Fermi gas, we use an ansatz for the semiclassical Wigner function, which resembles the form of the Wigner-transformed Fermi-Dirac distribution of a noninteracting Fermi gas. Note that the temperature of the dipolar Fermi gas in the experiment [39] is low enough that thermal fluctuations are expected to be of the order of $(T/T_F)^2 \approx 3\%$ due to the Sommerfeld expansion. This justifies to use the zero-temperature approximation for the Wigner-transformed Fermi-Dirac distribution of a noninteracting Fermi gas:

$$\nu^0(\mathbf{r},\mathbf{k}) = \Theta\left(1 - \sum_i \frac{r_i^2}{R_i^2} - \sum_i \frac{k_i^2}{K_i^2}\right). \tag{4}$$

Here Θ is the Heaviside step function. The variational parameters R_i and K_i represent the Thomas-Fermi (TF) radius and the Fermi momentum in the ith direction, respectively, and describe the extension of the equilibrium Fermi surface in both coordinate and momentum space. With this ansatz, the normalization of the distribution $\nu^0(\mathbf{r},\mathbf{k})$ to N fermions leads

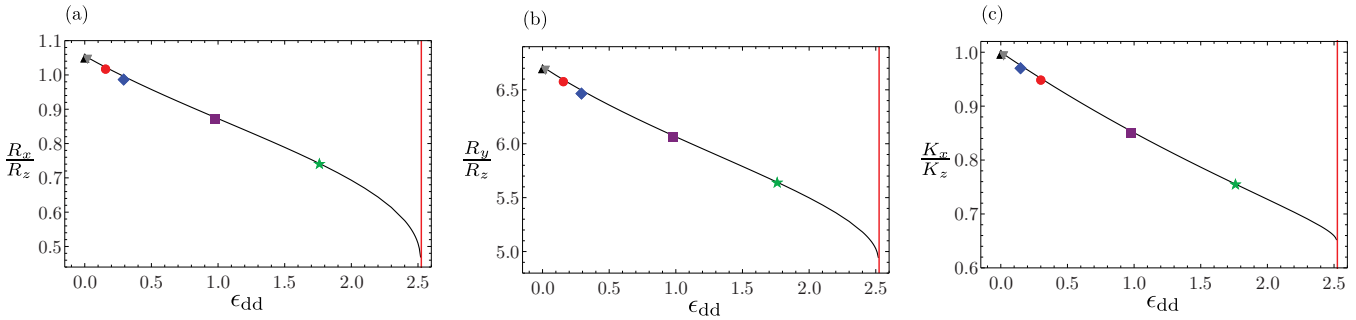

FIG. 2. Aspect ratios in real and momentum space as functions of relative dipolar interaction strength ϵ_{dd} for Fermi gases in global equilibrium for considered trap geometry with dipoles parallel to z axis: (a) R_x/R_z, (b) R_y/R_z, and (c) K_x/K_z. Black upward-pointing triangles represent aspect ratios for the limiting case of a noninteracting Fermi gas: in real space $R_x/R_z = \omega_z/\omega_x$ and $R_y/R_z = \omega_z/\omega_y$, while in momentum space $K_x/K_z = 1$ (Fermi sphere). Other symbols represent aspect ratios for dipolar atoms and molecules from Table II: ^{53}Cr (gray downward-pointing triangles), ^{167}Er (red circles), ^{161}Dy (blue diamonds), ^{40}K ^{87}Rb (purple squares), and ^{167}Er ^{168}Er (green stars). Red vertical line corresponds to a critical value of the relative dipolar interaction strength $\epsilon_{dd}^{crit} \approx 2.52$ for considered trap geometry; for $\epsilon_{dd} > \epsilon_{dd}^{crit}$ no stable stationary solution exists for a system of Eqs. (10)–(14), together with Eq. (5).

to the condition

$$N = \int d\mathbf{r} \int \frac{d\mathbf{k}}{(2\pi)^3}\, \nu^0(\mathbf{r},\mathbf{k}) = \frac{1}{48}\bar{R}^3\bar{K}^3\,, \tag{5}$$

where $\bar{R} = (R_x R_y R_z)^{1/3}$ and $\bar{K} = (K_x K_y K_z)^{1/3}$ denote the geometric means of the respective TF radii and momenta. The total energy of the system in the Hartree-Fock approximation for dipoles oriented along the z axis, i.e., $\beta = 0^\circ$, is given by

$$E = \frac{N}{8}\sum_j \frac{\hbar^2 K_j^2}{2M} + \frac{N}{8}\frac{M}{2}\sum_j \omega_j^2 R_j^2 - \frac{48N^2c_0}{8\bar{R}^3} f\left(\frac{R_x}{R_z},\frac{R_y}{R_z}\right) + \frac{48N^2c_0}{8\bar{R}^3} f\left(\frac{K_z}{K_x},\frac{K_z}{K_y}\right), \tag{6}$$

where $c_0 = \frac{2^{10}C_{\rm dd}}{3^4\cdot 5\cdot 7\pi^3}$, while the function f and its derivatives with respect to the first and second arguments, f_1 and f_2, respectively, are anisotropy functions defined in Refs. [44–46]. Note that the corresponding expression for the Hartree-Fock energy of the second considered case of dipoles oriented along the x axis, i.e., $\beta = 90^\circ$ is obtained by a simple cyclic permutation of indices $x \to y \to z \to x$ in Eq. (6). The same applies to all other equations throughout the paper.

The TF radii and momenta R_i and K_i are determined by minimizing the energy (6) with respect to them, which leads to the following set of algebraic equations:

$$\frac{\hbar^2 K_x^2}{2M} - \frac{1}{3}\sum_j \frac{\hbar^2 K_j^2}{2M} - \frac{48Nc_0}{\bar{R}^3}\frac{K_z}{K_x} f_1\left(\frac{K_z}{K_x},\frac{K_z}{K_y}\right) = 0, \tag{7}$$

$$\frac{\hbar^2 K_y^2}{2M} - \frac{1}{3}\sum_j \frac{\hbar^2 K_j^2}{2M} - \frac{48Nc_0}{\bar{R}^3}\frac{K_z}{K_y} f_2\left(\frac{K_z}{K_x},\frac{K_z}{K_y}\right) = 0, \tag{8}$$

$$\frac{\hbar^2 K_z^2}{2M} - \frac{1}{3}\sum_j \frac{\hbar^2 K_j^2}{2M} + \frac{48Nc_0}{\bar{R}^3}\left[\frac{K_z}{K_x} f_1\left(\frac{K_z}{K_x},\frac{K_z}{K_y}\right) + \frac{K_z}{K_y} f_2\left(\frac{K_z}{K_x},\frac{K_z}{K_y}\right)\right] = 0, \tag{9}$$

$$\omega_x^2 R_x^2 - \frac{1}{3}\sum_j \frac{\hbar^2 K_j^2}{M^2} - \frac{48Nc_0}{M\bar{R}^3}\left[f\left(\frac{K_z}{K_x},\frac{K_z}{K_y}\right) - f\left(\frac{R_x}{R_z},\frac{R_y}{R_z}\right) + \frac{R_x}{R_z} f_1\left(\frac{R_x}{R_z},\frac{R_y}{R_z}\right)\right] = 0, \tag{10}$$

$$\omega_y^2 R_y^2 - \frac{1}{3}\sum_j \frac{\hbar^2 K_j^2}{M^2} - \frac{48Nc_0}{M\bar{R}^3}\left[f\left(\frac{K_z}{K_x},\frac{K_z}{K_y}\right) - f\left(\frac{R_x}{R_z},\frac{R_y}{R_z}\right) + \frac{R_y}{R_z} f_2\left(\frac{R_x}{R_z},\frac{R_y}{R_z}\right)\right] = 0, \tag{11}$$

$$\omega_z^2 R_z^2 - \frac{1}{3}\sum_j \frac{\hbar^2 K_j^2}{M^2} - \frac{48Nc_0}{M\bar{R}^3}\left[f\left(\frac{K_z}{K_x},\frac{K_z}{K_y}\right) - f\left(\frac{R_x}{R_z},\frac{R_y}{R_z}\right) - \frac{R_x}{R_z} f_1\left(\frac{R_x}{R_z},\frac{R_y}{R_z}\right) - \frac{R_y}{R_z} f_2\left(\frac{R_x}{R_z},\frac{R_y}{R_z}\right)\right] = 0. \tag{12}$$

Note that Eqs. (7)–(9) are linearly dependent, and due to the symmetry of the anisotropy function $f(x,y) = f(y,x)$ can be reduced to two independent equations [44–46],

$$K_x = K_y\,, \tag{13}$$

$$K_z^2 - K_x^2 = \frac{144MNc_0}{\hbar^2\bar{R}^3}\left[1 - \frac{\left(2K_x^2 + K_z^2\right) f_s\left(\frac{K_z}{K_x}\right)}{2\left(K_x^2 - K_z^2\right)}\right], \tag{14}$$

where $f_s(x) \equiv f(x,x)$ denotes the diagonal part of the anisotropy function. This implies that the momentum distribution of a dipolar Fermi gas in global equilibrium remains cylindrically symmetric despite a general triaxial harmonic confinement [44,45]. Due to the anisotropy of the dipolar interaction potential, dipolar quantum gases tend to be stretched along the polarization direction, i.e., the direction of an external magnetic or electric field, since this leads to a lower total energy. We note that this is valid not only for fermions but for bosons as well [18,26,27]. Equations (10)–(14), together with Eq. (5), represent a closed set of six algebraic equations, which fix all variational parameters R_i and K_i in global equilibrium.

For sufficiently weak interactions, a local minimum might exist to which the system would return after a small perturbation. The regions of system parameters satisfying this property are called stable and the mathematical criterion behind this classification is given by positive eigenvalues of the Hessian matrix of the energy functional [45]. Figure 2 depicts aspect ratios of stable solutions, i.e., the deformation of the Fermi surface in real and momentum space in global equilibrium for the dipolar Fermi gases given in Table II. These results are obtained for the dipoles oriented in the direction of the z axis, i.e., for the angle $\beta = 0^\circ$ (see Fig. 1). For the limiting case of a noninteracting Fermi gas, we know that the aspect ratios in real space are $R_x/R_z = \omega_z/\omega_x$ and $R_y/R_z = \omega_z/\omega_y$, while in momentum space the Fermi surface becomes the Fermi sphere and therefore we have $K_x/K_z = 1$.

Red vertical lines in Fig. 2 represent a critical value of the relative interaction strength $\epsilon_{\rm dd}^{\rm crit} \approx 2.52$ for the considered trap geometry. Namely, for $\epsilon_{\rm dd} > \epsilon_{\rm dd}^{\rm crit}$ stable stationary solutions

TABLE II. Dipole moments (m for species with a magnetic dipole and d for species with an electric dipole) and relative interaction strengths of fermionic atoms and molecules to be used throughout the paper, calculated using the trap parameters and particle number given in the text.

Gas	^{53}Cr [51]	^{167}Er [52]	^{161}Dy [53]	^{40}K ^{87}Rb [55]	^{167}Er ^{168}Er [16]
m/d	$6\,\mu_{\rm B}$	$7\,\mu_{\rm B}$	$10\,\mu_{\rm B}$	0.2 D	$14\,\mu_{\rm B}$
$\epsilon_{\rm dd}$	0.02	0.15	0.30	0.97	1.76

for Eqs. (10)–(14), together with Eq. (5), do not exist [45,66] for system parameters from the Innsbruck experiment [39]. Note that the value of $\epsilon_{\rm dd}^{\rm crit}$ does not depend on the mass of the species and is universal for a given trap geometry, as can be shown by rewriting Eqs. (10)–(14) in the dimensionless form.

From Table I we see that electric dipolar molecules ^{23}Na ^{40}K and ^{40}K ^{87}Rb with the largest values of relative dipolar interaction strength $\epsilon_{\rm dd}$ are unstable for the considered system parameters if their maximal values of electric dipole moments are used, since in both cases $\epsilon_{\rm dd} > \epsilon_{\rm dd}^{\rm crit}$. However, by using an external electric field, their dipole moments can be tuned to smaller values, and therefore we will consider the case of ^{40}K ^{87}Rb with the value of electric dipole moment tuned down to $d = 0.2$ D [67], for which one obtains $\epsilon_{\rm dd} = 0.97 < \epsilon_{\rm dd}^{\rm crit}$. Table II gives the corresponding parameters of the five atomic and molecular dipolar species we will consider in the rest of this paper.

In Fig. 2, corresponding aspect ratios for the noninteracting case are shown as black upward-pointing triangles in comparison with aspect ratios for interacting Fermi gases. For atomic gases of ^{53}Cr, ^{167}Er, and ^{161}Dy the DDI is not that strong, and their aspect ratios in momentum space deviate less than 5% from unity; see Fig. 2(c). Actually, for ^{53}Cr (gray downward-pointing triangles), the aspect ratio in momentum space is just 1% smaller than 1, which is quite challenging to be observable in an experiment. Nevertheless, for ^{167}Er (red circles) the aspect ratio in momentum space turns out to be about 3% less than 1 and has already been experimentally observed in Ref. [39], meaning that the 5% deformation for ^{161}Dy (blue diamonds) should also be observable. For the considered parameters for ^{40}K ^{87}Rb (purple squares) with $\epsilon_{\rm dd} = 0.97$ we obtain an even larger value of the FS deformation of about 15%. Furthermore, a molecule of ^{168}Er ^{167}Er (green stars) with $\epsilon_{\rm dd} = 1.76$ would yield a FS deformation of nearly 25%.

Note that the critical value $\epsilon_{\rm dd}^{\rm crit}$ strongly depends on the trap geometry, as can be seen in Fig. 3, where we show its dependence on the frequency ω_x for fixed values $(\omega_y,\omega_z) = (91,611)\times 2\pi$ Hz from the Innsbruck experiment [39]. For

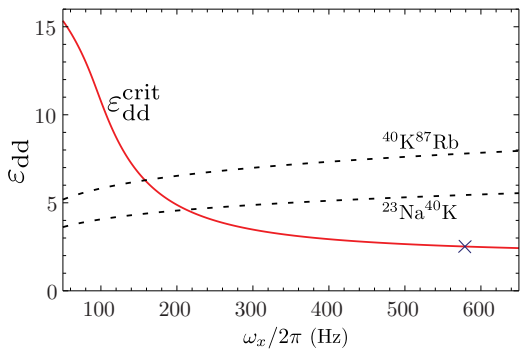

FIG. 3. Critical value of relative dipolar interaction strength $\epsilon_{\rm dd}^{\rm crit}$ (red solid line) as function of trap frequency ω_x for fixed values $(\omega_y,\omega_z) = (91,611)\times 2\pi$ Hz and particle number $N = 7\times 10^4$. Blue cross corresponds to experimental value of frequency $\omega_x = 579\times 2\pi$ Hz from the Innsbruck experiment [39], for which $\epsilon_{\rm dd}^{\rm crit} \approx 2.52$. Black dashed lines depict relative dipolar interaction strength $\epsilon_{\rm dd}$ for dipolar molecular species ^{23}Na ^{40}K and ^{40}K ^{87}Rb according to Eq. (3), for the same parameters and for maximal values of their electric dipole moments from Table I.

the corresponding experimental value $\omega_x = 579\times 2\pi$ Hz we obtain $\epsilon_{\rm dd}^{\rm crit} \approx 2.52$ (blue cross), the same value that can be deduced from Fig. 2. In Fig. 3, we also show relative dipolar interaction strength $\epsilon_{\rm dd}$ for molecular species ^{23}Na ^{40}K and ^{40}K ^{87}Rb for maximal values of their electric dipole moments from Table I. Note that the relative interaction strengths also depend on the trap geometry according to Eq. (3). As already pointed out, for the cigar-shaped trap geometry of the Innsbruck experiment [39], both molecular species turn out to be unstable. However, for the pancake-shaped trap with sufficiently small value of the frequency ω_x, i.e., $\omega_x < 210\times 2\pi$ Hz for ^{23}Na ^{40}K and $\omega_x < 155\times 2\pi$ Hz for ^{40}K ^{87}Rb, both species can be made stable even if their maximal electric dipole moments are used.

IV. SCALING ANSATZ FOR THE BOLTZMANN-VLASOV EQUATION

The dynamics of a trapped ultracold dipolar degenerate Fermi gas can be described in terms of the Botzmann-Vlasov (BV) equation, which was previously prominently used in the realm of nuclear [68,69] and plasma [70,71] physics. It was already used to study the TOF dynamics of ultracold fermions with the contact interaction [72,73], as well as their collective modes [74,75]. The BV equation determines the time evolution of the Wigner function ν [46] and for a dipolar Fermi gas it reads:

$$\frac{\partial \nu(\mathbf{r},\mathbf{k},t)}{\partial t} + \frac{\hbar\mathbf{k}}{M}\nabla_{\mathbf{r}}\nu + \frac{1}{\hbar}\nabla_{\mathbf{k}}U(\mathbf{r},\mathbf{k},t)\nabla_{\mathbf{r}}\nu(\mathbf{r},\mathbf{k},t) - \frac{1}{\hbar}\nabla_{\mathbf{r}}U(\mathbf{r},\mathbf{k},t)\nabla_{\mathbf{k}}\nu(\mathbf{r},\mathbf{k},t) = I_{\rm coll}[\nu](\mathbf{r},\mathbf{k},t)\,. \quad (15)$$

Here $U(\mathbf{r},\mathbf{k},t) = U_{\rm ext}(\mathbf{r}) + \int d\mathbf{r}' V_{\rm int}(\mathbf{r}-\mathbf{r}')n(\mathbf{r}',t) - \int \frac{d\mathbf{k}'}{(2\pi\hbar)^3} \tilde{V}_{\rm int}(\mathbf{k}-\mathbf{k}')\nu(\mathbf{r},\mathbf{k}',t)$ denotes the mean-field potential, which includes external trap potential, as well as the respective Hartree and Fock terms, where $V_{\rm int}(\mathbf{r})$ represents the DDI potential (2) and $\tilde{V}_{\rm int}(\mathbf{k})$ its Fourier transform. Note that this Hartree-Fock dynamic mean-field description is self-consistent and is of the first order in the interaction potential. On the right-hand side of Eq. (15), we have the collision integral $I_{\rm coll}[\nu](\mathbf{r},\mathbf{k},t)$, which is of second order of the interaction potential and describes collisions between two particles [76]. Instead of using a full expression for the collision integral, which would require a detailed modeling of scattering processes between atoms or molecules, we apply here the relaxation-time approximation [1,77] in the form

$$I_{\rm coll}[\nu(\mathbf{r},\mathbf{k},t)] = -\frac{\nu(\mathbf{r},\mathbf{k},t) - \nu^{\rm le}(\mathbf{r},\mathbf{k})}{\tau}\,. \quad (16)$$

Here τ denotes the relaxation time, which is related to the average time between collisions, and $\nu^{\rm le}$ stands for the distribution function corresponding to local equilibrium. The physical idea is that the particles interact via collisions and exchange energy and momentum, which eventually leads to a relaxation of the system into a local equilibrium state in which the collisions will no longer change the distribution function. In contrast to that, the local velocity field or the density can still be spatially dependent. The local thermodynamical equilibrium of a dipolar Fermi gas is defined by $I_{\rm coll}[\nu^{\rm le}] = 0$. If the time-dependent distribution function $\nu(\mathbf{r},\mathbf{k},t)$ is close to the global equilibrium $\nu^0(\mathbf{r},\mathbf{k})$, it can be approximately expressed

by a suitable rescaling of the equilibrium distribution [77]:

$$\nu(\mathbf{r},\mathbf{k},t) \to \Gamma(t)\nu^0[\boldsymbol{\mathcal{R}}(\mathbf{r},t),\boldsymbol{\mathcal{K}}(\mathbf{r},\mathbf{k},t)]\,, \tag{17}$$

with the rescaled variables defined by

$$\mathcal{R}_i(\mathbf{r},t) = \frac{r_i}{b_i(t)} \tag{18}$$

and

$$\mathcal{K}_i(\mathbf{r},\mathbf{k},t) = \frac{1}{\sqrt{\theta_i(t)}}\left[k_i - \frac{M\dot{b}_i(t)r_i}{\hbar b_i(t)}\right], \tag{19}$$

where $b_i(t)$ and $\theta_i(t)$ are time-dependent dimensionless scaling parameters. The normalization factor $\Gamma(t)$ is given by [77]

$$\Gamma(t)^{-1} = \prod_i b_i(t)\sqrt{\theta_i(t)}\,. \tag{20}$$

The second term in the bracket of Eq. (19) is proportional to the local velocity. Namely, taking the derivative with respect to time in Eq. (18) we get $\dot{\mathcal{R}}_i(\mathbf{r},t) \sim k_i - M\dot{b}_i(t)r_i/[\hbar b_i(t)]$ with $k_i = M\dot{r}_i/\hbar$ [42,78]. By subtracting the drift velocity $\dot{b}_i(t)r_i/b_i(t)$ in the ansatz (19), it is ensured that the momentum $\boldsymbol{\mathcal{K}}(\mathbf{r},\mathbf{k},t)$ is not affected by the time dependence of the ansatz for $\boldsymbol{\mathcal{R}}(\mathbf{r},t)$.

The time dependence of the distribution function is governed by the scaling parameters $b_i(t)$ and $\theta_i(t)$, which denote the time-dependent deformations of the spatial and momentum variables, respectively. By inserting the above ansatz into the Boltzmann-Vlasov equation (15), one obtains coupled ordinary differential equations of motion for the respective scaling parameters [46]:

$$\ddot{b}_i + \omega_i^2 b_i - \frac{\hbar^2 K_i^2 \theta_i}{M^2 b_i R_i^2} + \frac{48Nc_0}{Mb_iR_i^2\prod_j b_jR_j}\left[f\left(\frac{b_xR_x}{b_zR_z},\frac{b_yR_y}{b_zR_z}\right) - b_iR_i\frac{\partial}{\partial b_iR_i}f\left(\frac{b_xR_x}{b_zR_z},\frac{b_yR_y}{b_zR_z}\right)\right]$$

$$-\frac{48Nc_0}{Mb_iR_i^2\prod_j b_jR_j}\left[f\left(\frac{\theta_z^{\frac{1}{2}}K_z}{\theta_x^{\frac{1}{2}}K_x},\frac{\theta_z^{\frac{1}{2}}K_z}{\theta_y^{\frac{1}{2}}K_y}\right) + \theta_i^{\frac{1}{2}}K_i\frac{\partial}{\partial\theta_i^{\frac{1}{2}}K_i}f\left(\frac{\theta_z^{\frac{1}{2}}K_z}{\theta_x^{\frac{1}{2}}K_x},\frac{\theta_z^{\frac{1}{2}}K_z}{\theta_y^{\frac{1}{2}}K_y}\right)\right] = 0, \tag{21}$$

$$\dot{\theta}_i + 2\frac{\dot{b}_i}{b_i}\theta_i + \frac{1}{\tau}\left(\theta_i - \theta_i^{\mathrm{le}}\right) = 0. \tag{22}$$

Note that in the case of the global equilibrium, Eqs. (21) with the initial conditions $b_i(0) = \theta_i(0) = 1$ and $\dot{b}_i(0) = \dot{\theta}_i(0) = 0$ at $t = 0$ reduce to Eqs. (10)–(12), as expected. Also, we remark that the initial conditions correspond to $\nu(\mathbf{r},\mathbf{k},t=0) \equiv \nu^0(\mathbf{r},\mathbf{k})$.

V. TIME-OF-FLIGHT EXPANSION

The most ubiquitous method to study the physics of trapped ultracold gases is their absorption imaging after the release of the atomic or molecular cloud from the trap. Turning off the trap potential allows the ultracold gas cloud to expand for tens of milliseconds and an absorption image is taken afterward, when the cloud is large enough for the image to be recorded by a CCD camera. This technique, known as the TOF imaging, is one of the most important probes of ultracold quantum systems and TOF expansion experiments are a key diagnostic tool to study their properties. From the size of the expanded cloud and the known time of flight one can directly obtain, for instance, the Fermi energy for a noninteracting degenerate Fermi gas. In the case of free ballistic expansion, which is generically applied to theoretically model TOF, the ellipsoidal FS deformation due to DDI is taken into account before TOF, while all interactions between atoms during TOF are neglected. In contrast to that, a nonballistic expansion model takes into account interactions for calculating both global equilibrium before TOF and the subsequent expansion. In this section, we show how quantitative information about the ellipsoidal FS deformation relevant for the current experiments can be determined from solving the BV equation for a TOF expansion of the dipolar Fermi gas.

Bearing in mind that the trap potential is turned off during TOF, Eqs. (21) and (22) can be used to describe the TOF dynamics if we remove the terms $\omega_i^2 b_i$ which stem from the harmonic trap potential. Within this formalism, the average sizes of the Fermi gas cloud in real space are given by (see Appendix A for more details)

$$\langle r_i^2\rangle = \frac{1}{N}\int\frac{d\mathbf{k}}{(2\pi)^3}\int d\mathbf{r}\,\nu(\mathbf{r},\mathbf{k},t)r_i^2 = \frac{1}{8}R_i^2b_i^2(t)\,. \tag{23}$$

The deformation of the cloud shape is described in terms of the cloud aspect ratio $A_R(t)$, which is defined by the ratio of the root mean square of the transverse and longitudinal cloud radii, i.e., the average sizes of the cloud in vertical $\sqrt{\langle r_{\mathrm{v}}^2\rangle}$ and horizontal $\sqrt{\langle r_{\mathrm{h}}^2\rangle}$ direction in the imaging plane. Since the imaging axis in the Innsbruck experiment [39] has an angle of $\alpha = 28^\circ$ with respect to the y axis, according to Eq. (A6) from Appendix A this leads to

$$A_R(t) = \frac{R_zb_z(t)}{\sqrt{R_x^2b_x^2(t)\cos^2\alpha + R_y^2b_y^2(t)\sin^2\alpha}}\,. \tag{24}$$

This aspect ratio in real space $A_R(t)$ represents a directly measurable quantity in the TOF dynamics experiments. In order to describe the influence of DDI on the FS we also use a corresponding aspect ratio in momentum space. In analogy to $A_R(t)$, the average sizes of the Fermi gas cloud in momentum space read (see Appendix B for more details)

$$\langle k_i^2\rangle = \frac{1}{N}\int d\mathbf{r}\int\frac{d\mathbf{k}}{(2\pi)^3}\nu(\mathbf{r},\mathbf{k},t)k_i^2$$

$$= \frac{1}{8}\left(K_i^2\theta_i(t) + \frac{M^2R_i^2\dot{b}_i^2(t)}{\hbar^2}\right), \tag{25}$$

and the corresponding aspect ratio in momentum space is given by

$$A_K(t) = \sqrt{\frac{\langle k_z^2\rangle}{\langle k_x^2\rangle \cos^2\alpha + \langle k_y^2\rangle \sin^2\alpha}}. \tag{26}$$

The relaxation time τ in Eqs. (22) determines the regime of the dipolar Fermi gas and, therefore, by solving the appropriate equations for varying values of τ, we are able to describe dynamic properties of the Fermi gas all the way from the collisionless ($\bar{\omega}\tau \gg 1$) to the hydrodynamic ($\bar{\omega}\tau \ll 1$) regime. Here, as before, $\bar{\omega}$ represents the geometric mean of the trap frequencies. In Sec. V A, we will study the collisionless regime; in Sec. V B, we examine the hydrodynamic regime; while in Sec. V C, we will investigate the system behavior in the intermediate, collisional regime. In Sec. V D, we will improve the relaxation-time approximation in the collisional regime even further by determining the relaxation time in a self-consistent way.

A. Collisionless regime

The value of the relaxation time τ determines the regime of the Fermi gas during the expansion. In the low-density or collisionless regime, which is determined by the condition $\bar{\omega}\tau \gg 1$, the relaxation time τ can be taken to be infinite. In the limit $\tau \to \infty$, the differential Eqs. (22) for the scaling parameters θ_i decouple and the dynamic behavior in each direction is independent from the others. Due to this, Eqs. (22) can be solved analytically. With the respective initial conditions $b_i(0) = \theta_i(0) = 1$ and $\dot{b}_i(0) = \dot{\theta}_i(0) = 0$, we obtain $\theta_i(t) = b_i(t)^{-2}$. Inserting this solution in Eqs. (21) for the scaling parameters $b_i(t)$ yields the equations of motion in the collisionless regime [40–42]. We numerically solve them for a general system geometry, where the trap frequencies in the three directions are different and correspond to the values of the Innsbruck experiment [39], and the magnetic field is oriented either in z direction ($\beta = 0^\circ$) or in x direction ($\beta = 90^\circ$). Although at $\beta = 90^\circ$ the dipoles' orientation forms an angle of $\gamma = 14^\circ$ (see Fig. 1) with respect to the x axis, we assume for simplicity in our calculations that the dipoles are parallel to the x axis.

Graphs in the left-hand side column of Fig. 4 show aspect ratios $\sqrt{\langle r_x^2\rangle/\langle r_z^2\rangle}$, $\sqrt{\langle r_y^2\rangle/\langle r_z^2\rangle}$, as well the cloud aspect ratio A_R in real space during TOF in the collisionless regime. The black dotted line in the middle corresponds to the case of a noninteracting Fermi gas, i.e., $c_0 = 0$, where the differential equations for the scaling parameters $b_i(t)$ can be solved analytically, yielding

$$b_i^{(0)}(t) = \sqrt{1 + \left(\frac{\hbar K_i^{(0)}}{M R_i^{(0)}}\right)^2 t^2}, \tag{27}$$

with $R_i^{(0)}$ and $K_i^{(0)}$ denoting the global equilibrium radius and momentum in the ith direction, respectively. These scaling parameters are solutions of Eqs. (10)–(14), together with Eq. (5), for the case of a noninteracting Fermi gas with

$$R_i^{(0)} = \sqrt{\frac{2E_F}{M\omega_i^2}}, \quad K_i^{(0)} = \sqrt{\frac{2ME_F}{\hbar^2}}, \tag{28}$$

where $E_F = (6N)^{1/3}\hbar\bar{\omega}$ denotes the Fermi energy. All aspect ratios for a noninteracting Fermi gas in real space asymptotically approach one in the long TOF limit. This shows that a cloud of noninteracting fermions becomes spherical after a sufficiently long expansion, reflecting its isotropic momentum distribution even in the triaxial harmonic trap. As DDI is absent here, the orientation of the magnetic or the electric field, i.e., of the dipole moments of atoms or molecules, has no influence on the FS deformation [79]. Graphs in the right-hand side column of Fig. 4 show the corresponding aspect ratios in momentum space. As expected, the black dotted line is constant and equal to one, and as for the noninteracting fermions the FS is not deformed.

Furthermore, Fig. 4 also depicts the time dependence of the aspect ratios when the DDI is taken into account. Dashed lines correspond to the ballistic expansion, when DDI is assumed to affect the initial ground state, but not later during the expansion. Mathematically, this means that the ballistic expansion is also determined by Eqs. (27), but now with the parameters R_i and K_i instead of $R_i^{(0)}$ and $K_i^{(0)}$, respectively:

$$b_i^{\mathrm{bal}}(t) = \sqrt{1 + \left(\frac{\hbar K_i}{M R_i}\right)^2 t^2}. \tag{29}$$

Solid lines in Fig. 4 represent results for the nonballistic expansion, when we take DDI into account for calculating both the initial ground state and the subsequent expansion. To obtain these results, one has to solve numerically the coupled differential Eqs. (21) together with $\theta_i(t) = b_i(t)^{-2}$. In Figs. 4(a) to 4(d), top red solid and dashed lines correspond to the orientation of dipoles in the x direction, and bottom blue solid and dashed lines correspond to dipoles' orientation in the z direction, while in Figs. 4(e) and 4(f) the position of lines turns out to be reversed: Top blue lines give results for dipoles in the z direction, and bottom red lines show them for dipoles in the x direction.

From the graphs in the right-hand column of Fig. 4, we read off that the aspect ratios in momentum space are constant if ballistic expansion approximation is used (all dashed lines). This is not surprising, since here DDI is neglected during the expansion. This can also be shown mathematically if we insert the solution for $b_i^{\mathrm{bal}}(t)$ from Eq. (29) into expression (25) for $\langle k_i^2\rangle$, using $\theta_i(t) = b_i(t)^{-2}$, which is valid for the collisionless regime. With this we obtain $\langle k_i^2\rangle^{\mathrm{bal}} = K_i^2$; thus the momentum space aspect ratios $\sqrt{\langle k_i^2\rangle^{\mathrm{bal}}/\langle k_j^2\rangle^{\mathrm{bal}}} = K_i/K_j$ for the ballistic expansion are clearly time independent and are therefore determined by the initial ground-state distribution.

From Fig. 4, we see that the cloud aspect ratios in real space reach their corresponding plateaus after several tens of milliseconds. The asymptotic value of A_R for $\beta = 0^\circ$ for ballistic expansion is 1.025, whereas for nonballistic expansion it is 1.035, thus resulting in a 1% difference due to DDI. For $\beta = 90^\circ$, the asymptotic value of A_R for ballistic expansion is 0.98, while for nonballistic expansion it is 0.97, representing again a 1% difference. We also note that for $\beta = 0^\circ$ the usual inversion of the cloud shape occurs, while for $\beta = 90^\circ$ this is not the case. All these results are in excellent quantitative agreement with the experimental values reported in Ref. [39].

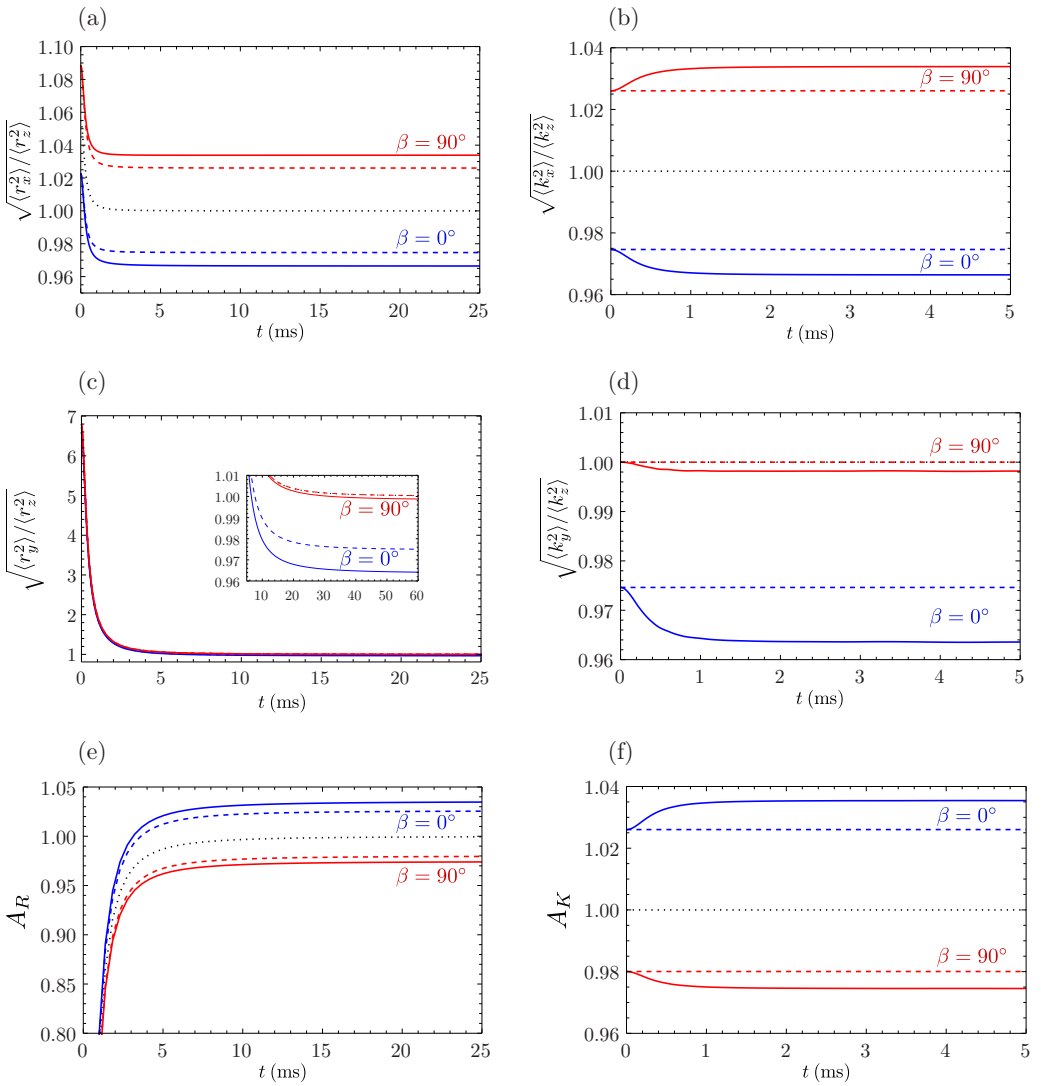

FIG. 4. Aspect ratios in real and momentum space in the collisionless regime during TOF expansion of ultracold gas of ^{167}Er: (a) $\sqrt{\langle r_x^2\rangle/\langle r_z^2\rangle}$, (b) $\sqrt{\langle r_y^2\rangle/\langle r_z^2\rangle}$, (c) A_R, (d) $\sqrt{\langle k_x^2\rangle/\langle k_z^2\rangle}$, (e) $\sqrt{\langle k_y^2\rangle/\langle k_z^2\rangle}$, (f) A_K. Black dotted lines represent aspect ratios for noninteracting case, dashed lines represent ballistic expansion, and solid lines represent nonballistic expansion. As indicated in the graphs (a)–(d), two lower blue solid and dashed lines correspond to $\beta = 0°$, and two upper red solid and dashed lines correspond to $\beta = 90°$, while in graphs (e) and (f) the position of lines is reversed: two upper blue solid and dashed lines are for $\beta = 0°$, and two lower red solid and dashed lines are for $\beta = 90°$.

Aspect ratios in momentum space behave similarly, and again a difference of around 0.5–1% between their asymptotic values in a ballistic and nonballistic expansion are observed. But one important difference is that here they are reached much faster, after several milliseconds. A more detailed analysis reveals that the two terms in Eq. (25) compete with each other during TOF, but the second term becomes dominant quite fast. Although the corresponding term in Eq. (23) has the same asymptotic behavior, the initial value of A_K is much closer to its asymptotic value than in the case of A_R and, as a consequence, all aspect ratios in momentum space converge faster.

Note that the aspect ratio in momentum space at the initial time $t = 0$ coincides with the asymptotic aspect ratio in real space for ballistic expansion:

$$A_K^{\mathrm{bal}}(0) = \lim_{t\to\infty} A_R^{\mathrm{bal}}(t)\,. \tag{30}$$

The ballistic expansion aspect ratio in momentum space at $t = 0$ can be calculated from Eq. (26) by using the initial conditions for the scaling parameters to yield

$$A_K^{\mathrm{bal}}(0) = \frac{K_z}{\sqrt{K_x^2\cos^2\alpha + K_y^2\sin^2\alpha}}\,. \tag{31}$$

On the other hand, the asymptotic value of the ballistic expansion aspect ratio in real space can be obtained if we insert the approximate expressions for the long-time behavior of the scaling parameters $b_i^{\mathrm{bal}}(t) \approx \hbar K_i t/(M R_i)$ from Eq. (29) into Eq. (24), which yields the same value as $A_K^{\mathrm{bal}}(0)$ in Eq. (31). This fact was used in Ref. [39] in order to observe the ellipsoidal deformation of the FS, as the real space aspect ratios can be readily measured during TOF. However, this is only correct within the ballistic approximation, as for the truly nonballistic expansion such a relationship is no longer valid.

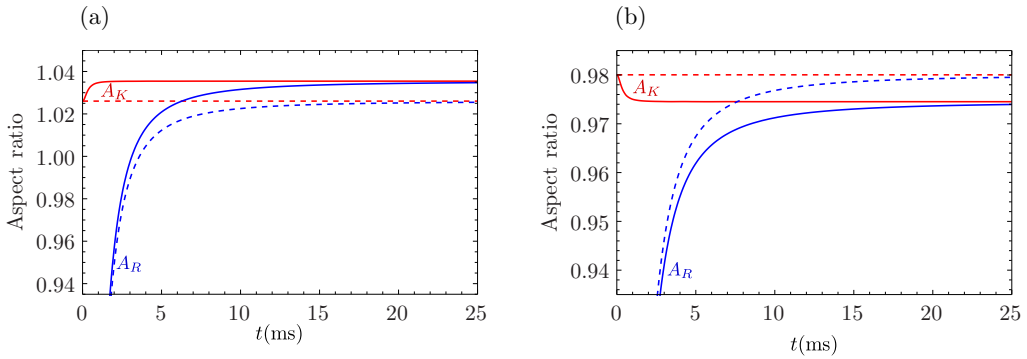

FIG. 5. Aspect ratios in real and momentum space in the collisionless regime converge to the same asymptotic values during TOF expansion of ultracold gas of ^{167}Er: (a) $\beta = 0^\circ$, (b) $\beta = 90^\circ$. Solid (dashed) lines represent aspect ratios for nonballistic (ballistic) expansion of ^{167}Er. The initially lower branch of blue lines corresponds to real space aspect ratios A_R, while the initially upper branch of red lines corresponds to momentum space aspect ratios A_K.

But from Fig. 5 we read off that both for ballistic (dashed lines) and nonballistic (solid lines) expansion another relationship seems to hold. Namely, the aspect ratios in momentum space and the corresponding aspect ratios in real space turn out to have the same asymptotic values:

$$\lim_{t\to\infty} A_K(t) = \lim_{t\to\infty} A_R(t)\,. \tag{32}$$

The above is true for both considered orientations of dipoles, i.e., $\beta = 0^\circ$ and $\beta = 90^\circ$. A similar conclusion was reached in Ref. [38] for a dipolar Fermi gas that was initially in a cylindrically symmetric harmonic trap, but we see here that this is true even for a fully anisotropic harmonic trapping potential. Note that this finding cannot be directly used to determine the aspect ratio in momentum space at $t = 0$ and the corresponding initial deformation of the FS, as for the ballistic expansion according to Eq. (30). But this observation still allows us to theoretically extract information on the momentum space distribution from experimental data. However, this requires that the corresponding equations are propagated backwards in time, so that the initial distribution in momentum space is calculated starting from the experimentally measured distribution in real space. Here, the numerical challenge is that this backward propagation has to be calculated for an infinitely long expansion time.

B. Hydrodynamic regime

In contrast to the previously considered collisionless regime, where collisions are completely neglected, we now turn to the hydrodynamic regime, where the system is supposed to have such a high density and, therefore, such a high collision rate, that it is always in local equilibrium. Although realistic systems, even if initially in the hydrodynamic regime, eventually become collisionless during the expansion, we follow Refs. [44,45] and consider this theoretical limiting case for the sake of completeness.

In the hydrodynamic regime, the scaling parameters $\theta_i^{\rm hd}$ always coincide with the local equilibrium values; i.e., we have $\theta_i^{\rm hd} = \theta_i^{\rm le}$. However, since the limit $\tau \to 0$ holds, the last terms in the left-hand side of Eqs. (22) are undetermined. Therefore, instead of Eqs. (22), the hydrodynamic regime is defined via the condition [77]

$$\Gamma^{\rm hd}(t)^{-1} = \prod_i b_i^{\rm hd}(t)\sqrt{\theta_i^{\rm hd}(t)} = 1\,. \tag{33}$$

Using this condition, minimizing the Hartree-Fock energy (6) in the local equilibrium leads to the equations [44,45]

$$\theta_x^{\rm hd} = \theta_y^{\rm hd}\,, \tag{34}$$

$$\frac{\hbar^2\theta_z^{\rm hd}K_z^2}{2M} - \frac{\hbar^2\theta_x^{\rm hd}K_x^2}{2M} = \frac{72Nc_0}{\prod_j b_j^{\rm hd}R_j}\left[1 + \frac{\left(2\theta_x^{\rm hd}K_x^2 + \theta_z^{\rm hd}K_z^2\right) f_s\left(\frac{\sqrt{\theta_z^{\rm hd}}K_z}{\sqrt{\theta_x^{\rm hd}}K_x}\right)}{2\left(\theta_z^{\rm hd}K_z^2 - \theta_x^{\rm hd}K_x^2\right)}\right]. \tag{35}$$

Equations (21), together with the identifications $b_i(t) = b_i^{\rm hd}(t)$ and $\theta_i(t) = \theta_i^{\rm hd}(t)$, with Eqs. (34) and (35), and the normalization condition (33) represent a closed set of six equations for the six respective scaling parameters in the hydrodynamic regime. These equations are solved numerically during the nonballistic TOF expansion. For comparison, we have also solved the corresponding equations for the ballistic expansion, although the hydrodynamic regime implies that DDI cannot be neglected at any point.

Figure 6 shows the corresponding aspect ratios in real and momentum space for ^{167}Er. As expected, we see that there is a significant difference between the ballistic and the nonballistic expansion, in contrast to the collisionless regime in Fig. 4. From the graphs in the left column of Fig. 6, we observe that the real space aspect ratios for $\beta = 0^\circ$ behave generally similarly to those in the collisionless regime, including the cloud shape inversion, although the asymptotic values differ more from their initial values for nonballistic expansion. On the other hand, for $\beta = 90^\circ$ we see a qualitatively different behavior in Fig. 6(a), where the aspect ratio $\sqrt{\langle r_x^2\rangle/\langle r_z^2\rangle}$ increases, while in Fig. 4(a) it decreases. In Fig. 6(c) for $\beta = 90^\circ$, we read off that the aspect ratio A_R even behaves nonmonotonously, with a local maximum at around 1 ms, while in

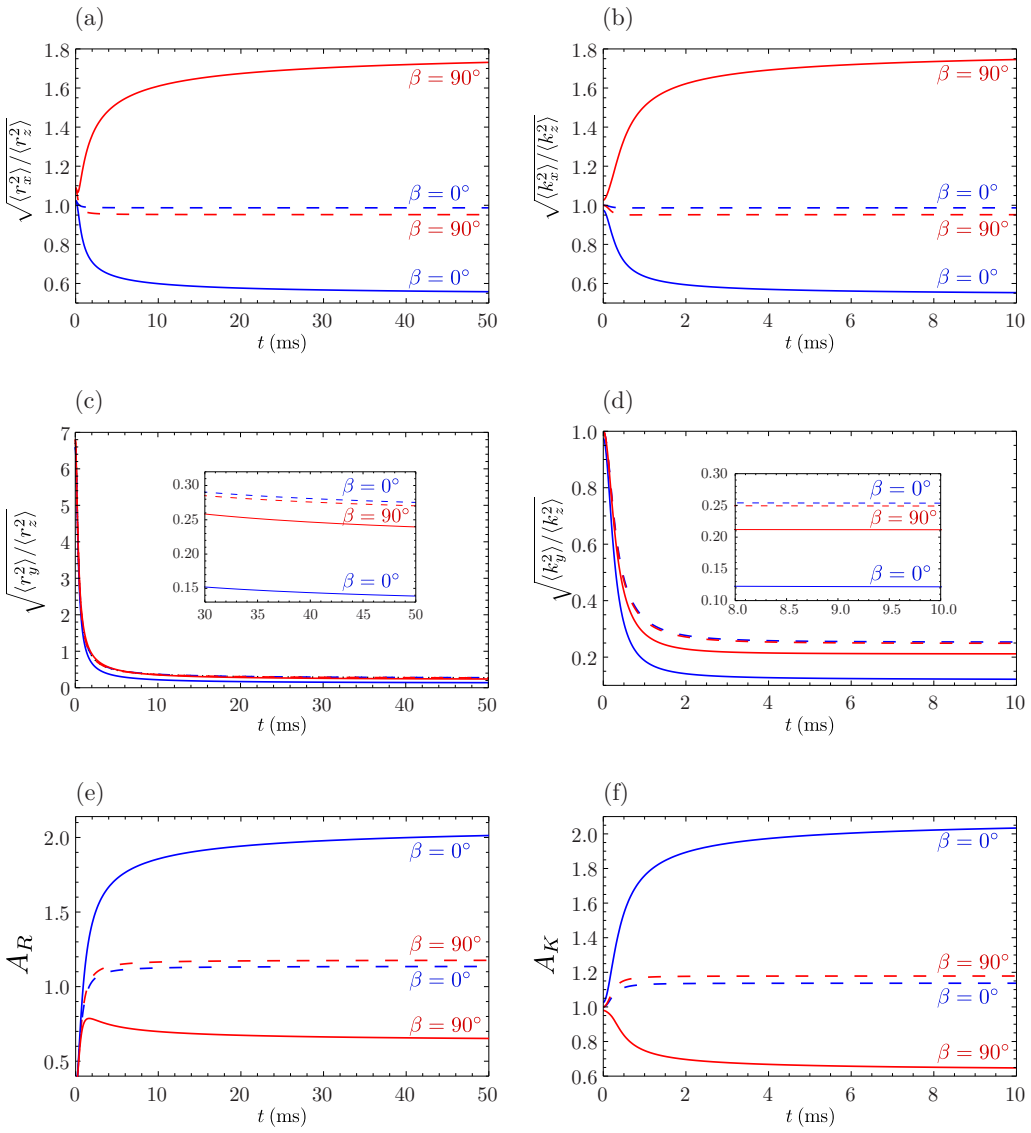

FIG. 6. Aspect ratios in real and momentum space in the hydrodynamic regime during TOF expansion of ultracold gas of ^{167}Er: (a) $\sqrt{\langle r_x^2\rangle/\langle r_z^2\rangle}$, (b) $\sqrt{\langle r_y^2\rangle/\langle r_z^2\rangle}$, (c) A_R, (d) $\sqrt{\langle k_x^2\rangle/\langle k_z^2\rangle}$, (e) $\sqrt{\langle k_y^2\rangle/\langle k_z^2\rangle}$, (f) A_K. Dashed lines represent ballistic expansion and solid lines represent nonballistic expansion. As indicated in graphs (a)–(d), the lower blue solid and the upper blue dashed line correspond to $\beta = 0°$, while the upper red solid and the lower red dashed line correspond to $\beta = 90°$. In graphs (e) and (f), the position of lines is reversed: The upper blue solid and the lower blue dashed line are for $\beta = 0°$; the lower red solid and the upper red dashed line are for $\beta = 90°$.

the collisionless regime it only increases monotonously until it reaches its asymptotic value. However, again the inversion of the cloud shape is not present for $\beta = 90°$, unlike for $\beta = 0°$. We also note that the positions of ballistic expansion curves are reversed in all graphs compared to the collisionless regime, including those for momentum space aspect ratios.

The behavior of momentum space aspect ratios in the right column of Fig. 6 is generally the same as in Fig. 4 for the collisionless regime, just with larger differences between initial and asymptotic values, for both cases $\beta = 0°$ and $\beta = 90°$.

The final cloud aspect ratio in real space for nonballistic expansion is twice as large as the corresponding collisionless value for $\beta = 0°$, while for $\beta = 90°$ the asymptotic value of the aspect ratio is around 0.65, which amounts to a decrease of around 35% compared to the collisionless value. For the ballistic expansion, which we know to be unrealistic in the hydrodynamic regime, the corresponding increase and decrease amounts are both around 12%. Similar numbers are also obtained for the momentum space aspect ratio A_K, as can be seen from the graphs on the right-hand side in Fig. 6. Since the corresponding values in the collisionless regime are all close to one, the above percentages also apply here and represent the results for the ellipsoidal deformation of the FS in the hydrodynamic regime.

The same conclusion can be also obtained from Fig. 7, where we compare aspect ratios in real and momentum space. Furthermore, with these graphs we confirm that the asymptotic values of the aspect ratios A_R and A_K also coincide in the

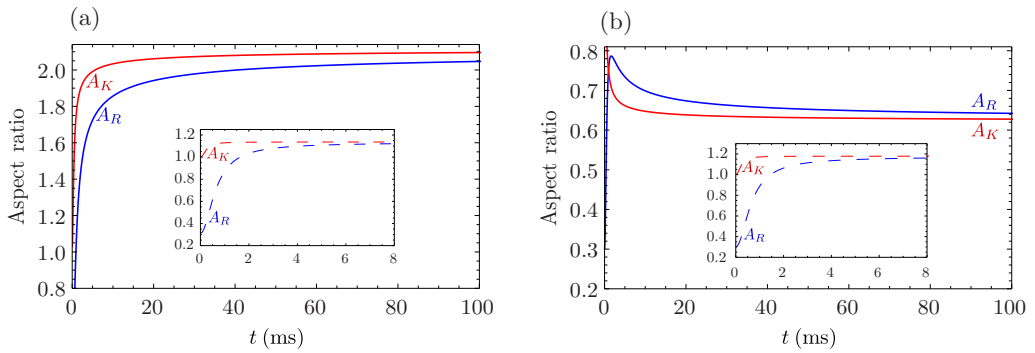

FIG. 7. Aspect ratios in real and momentum space in the hydrodynamic regime converge to the same asymptotic values during TOF expansion of ultracold gas of ^{167}Er: (a) $\beta = 0°$, (b) $\beta = 90°$. Solid lines give aspect ratios for nonballistic expansion, while dashed lines in the insets show the corresponding ballistic results. Blue lower lines in panel (a) and blue upper lines in panel (b) correspond to A_R, while red upper lines in panel (a) and red lower lines in panel (b) correspond to A_K.

hydrodynamic regime for both cases $\beta = 0°$ and $\beta = 90°$, as stated by Eq. (32) for the collisionless regime. If we compare the convergence of aspect ratios to their asymptotic values in Figs. 5 and 7, we see that in the hydrodynamic regime typical times to reach the plateau are similar in real and in momentum space, and have the value of several tens of milliseconds. This coincides with the corresponding convergence times for real space aspect ratios in the collisionless regime, where also a significant difference between the initial and the asymptotic values of aspect ratios occurred. Only in the case of momentum space aspect ratios in the collisionless regime, where the deformation of the FS is small during the whole expansion, can asymptotic values be reached faster, namely in just few milliseconds.

However, as already emphasized, even if initially in the hydrodynamic regime, the dipolar Fermi gas becomes more dilute during the TOF expansion, and the hydrodynamic regime continuously goes over into the collisional regime, and, finally, into the collisionless regime. Therefore, we model the collisional regime in the remainder of this section, since it is relevant for experiments where the density of the Fermi gas is high enough so that we can assume it is initially in the collisional or in the hydrodynamic regime.

C. Collisional regime with constant relaxation time

Here we start considering the collisional regime and assume that the relaxation-time approximation (16) can be applied. Furthermore, in this section we presume that the relaxation time τ remains constant during the TOF. The latter assumption is only valid for short times of flight, before the density of the gas decreases significantly. We will improve upon this approximation in Sec. V D, where the relaxation time is determined self-consistently.

However, provided that the relaxation time is constant, the TOF dynamics can be obtained by directly solving Eqs. (21) and (22) for a given value of τ. Note that the values of the scaling parameters $\theta_i^{\rm le}$ in local equilibrium are obtained according to Sec. V B; i.e., they represent the solutions of the equations for the hydrodynamic regime $\theta_i^{\rm hd}$.

The physical meaning of Eqs. (22) is that dissipation occurs when the system is outside of a local equilibrium as long as there are collisions, i.e., as long as the relaxation time τ remains finite. Effects of collisions are therefore described through Eqs. (22), whereas Eqs. (21) for the scaling parameters b_i do not directly contain such terms. However, effects of collisions enter indirectly into Eqs. (21) through the scaling parameters θ_i.

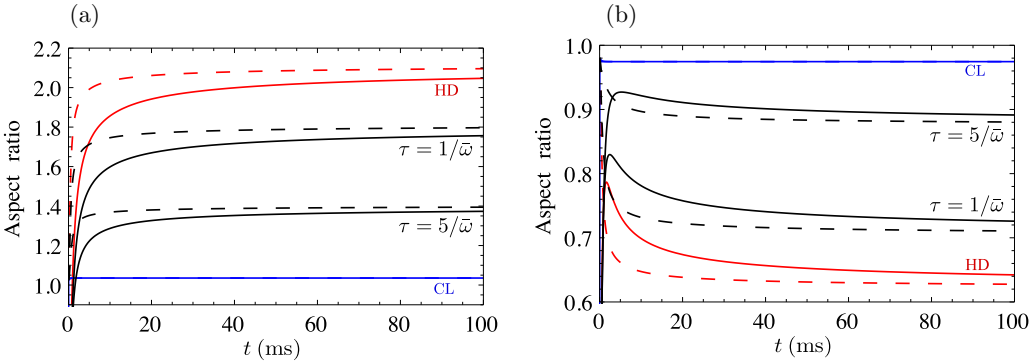

FIG. 8. Aspect ratios in real (solid lines) and momentum space (dashed lines) in the collisional regime during TOF expansion of ultracold gas of ^{167}Er: (a) $\beta = 0°$, (b) $\beta = 90°$. The pairs of curves in panel (a) from top to bottom and in panel (b) from bottom to top correspond to hydrodynamic regime (HD, red), collisional regime (black) for fixed relaxation times $\tau = 1/\bar{\omega}$ and $\tau = 5/\bar{\omega}$, and collisionless regime (CL, blue).

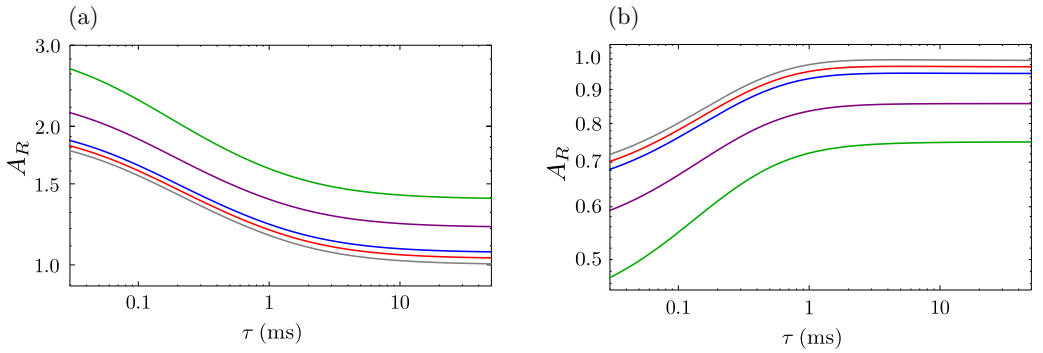

FIG. 9. Aspect ratios in real space after $t = 10$ ms TOF as function of fixed relaxation time τ for different ultracold Fermi gases: (a) $\beta = 0°$, (b) $\beta = 90°$. The curves in panel (a) from bottom to top and in panel (b) from top to bottom correspond to ^{53}Cr (gray), ^{167}Er (red), ^{161}Dy (blue), ^{40}K ^{87}Rb (purple), and ^{167}Er ^{168}Er (green).

Here we numerically solve the coupled system of Eqs. (21) and (22) during the nonballistic expansion for a fixed value of the relaxation time τ. Varying the value of the relaxation time we are able to describe all regimes, from the collisionless, obtained in the limit $\tau \to \infty$, to the hydrodynamic, obtained in the limit $\tau \to 0$. In particular, although the approximation of a fixed relaxation time is not realistic for longer expansion times, it allows us to understand and describe in more detail different collisional regimes, for finite values of τ, when the system undergoes a crossover from one limiting regime to the other.

Figure 8 shows the obtained aspect ratios for ^{167}Er in real and momentum space for the two limiting cases considered previously, the collisionless and the hydrodynamic regime, as well as for the collisional regime with the fixed relaxation times $\tau = 1/\bar{\omega}$ and $\tau = 5/\bar{\omega}$, where $\bar{\omega}$ represents a geometric mean of the trap frequencies. Depending on the respective geometry, asymptotic values of aspect ratios either decrease with increasing relaxation time [see Fig. 8(a) for $\beta = 0°$] or vice versa [see Fig. 8(b) for $\beta = 90°$]. We also read off from these figures that the corresponding asymptotic values of aspect ratios in real and momentum space in the collisional regime are again equal according to relation (32).

Motivated by the experiment reported in Ref. [39], in Fig. 9 we plot the aspect ratio in real space A_R obtained after $t = 10$ ms TOF as a function of a fixed relaxation time τ for two different orientations of dipoles for the respective ultracold Fermi gases given in Table II. If the dipoles are oriented along the z axis, i.e., Fig. 9(a), the corresponding aspect ratios for any fixed value of the relaxation time τ increase monotonously with the relative dipolar interaction strength $\epsilon_{\rm dd}$, while for the dipoles along x axis, i.e., Fig. 9(b), the situation is opposite, as expected. Note that the corresponding curves for the noninteracting case $\epsilon_{\rm dd} = 0$ would be quite close to those for ^{53}Cr, as can already be expected according to Fig. 2.

Plots like those in Fig. 9 represent powerful diagnostic tools for estimating the relaxation time τ from experimentally measured values of aspect ratios A_R for sufficiently short TOF, when the fixed relaxation-time approximation is still applicable. Furthermore, these graphs can be used for estimating the time scale t to approach the asymptotic values of the aspect ratios from experimentally available TOF expansion data. Provided that it turns out for a TOF t that the corresponding relaxation time τ satisfies the condition $\bar{\omega}\tau \gg 1$, one has already reached the collisionless regime. This means that for longer times t no further change of the aspect ratio is expected as one is already quite close to its asymptotic value.

D. Collisional regime with self-consistently determined relaxation time

Whereas in Sec. V C we assumed that the relaxation time is constant, now we model the TOF expansion of ultracold dipolar Fermi gases more realistically and take into account that the relaxation time is also time dependent. Namely, during TOF the gas rapidly expands, the distance between atoms grows, and as a consequence the relaxation time increases, thus eventually leading the system into the collisionless regime, even if initially it was in the hydrodynamic or in the collisional regime.

In order to quantify this physical notion, one would have to calculate the collision integral on the right-hand side of Eq. (15), which requires a detailed modeling of scattering processes in the system, i.e., the elastic collisions of fermionic atoms or molecules that arise purely from universal dipolar scattering. The standard approach for the case of a system close to local equilibrium is to use the relaxation-time approximation [1,77], which is given by Eq. (16). In Ref. [80], it was derived that the characteristic relaxation time for a classical gas can be expressed as

$$\tau = \frac{\alpha_{\rm coll}}{\bar{n}\sigma_{\rm el} v}, \tag{36}$$

where the parameter $\alpha_{\rm coll}$ denotes a geometry-dependent average number of collisions which is necessary to rethermalize the system after a collision, $\bar{n}$ represents the mean number density, $\sigma_{\rm el}$ is the total elastic cross section, and v is the mean relative velocity. In Ref. [81], it was heuristically argued and experimentally confirmed that for quantum degenerate dipolar fermionic systems at low temperatures and parameter regimes considered here, the relaxation time can be modeled by a modified expression

$$\tau_{\rm SC} = \frac{\alpha_{\rm coll}}{\eta\bar{n}\sigma_{\rm el} v}, \tag{37}$$

which allows us to calculate it self-consistently; hence the subscript SC. In the above equation, η stands for a Pauli suppression factor, which represents the reduction of the

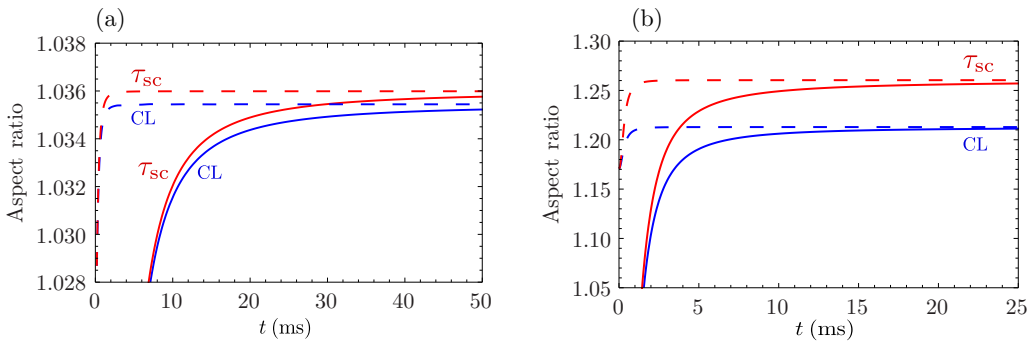

FIG. 10. Aspect ratios in real (solid lines) and momentum space (dashed lines) in the collisional regime during TOF expansion for $\beta = 0°$: (a) ^{167}Er, (b) ^{40}K ^{87}Rb. Red upper solid and dashed lines correspond to expansion dynamics with self-consistently determined relaxation time τ_{sc}. For comparison, blue lower solid and dashed lines give the corresponding aspect ratios for the collisionless regime (CL).

rethermalization rate in a degenerate Fermi gas due to Pauli blocking, and amounts to $\eta = 1$ for nondegenerate gases. The Pauli suppression factor depends on the degeneration level of fermions and is usually expressed as a function of the dimensionless temperature T/T_F, where T denotes the temperature and T_F is the Fermi temperature for the corresponding system.

In the considered case, the mean number density is given by $\bar{n} = N/V(t)$, where the volume $V(t)$ of the Fermi gas increases during the TOF expansion according to

$$V(t) = \frac{4\pi}{3} \prod_i R_i b_i(t) \,. \tag{38}$$

The total elastic cross section σ_{el} is universally related to the dipole moment of fermions [67] according to

$$\sigma_{el} = \frac{32\pi}{15} a_{dd}^2 \,, \tag{39}$$

where $a_{dd} = C_{dd} M/8\pi\hbar^2$ represents a characteristic dipole length. The mean relative velocity v is given by

$$v = \sqrt{\frac{16 k_B T}{\pi M}} \,. \tag{40}$$

For the parameters of the experiment [39] with atomic ^{167}Er used throughout this paper, the universal dipolar scattering theory [81] predicts the total elastic cross section value $\sigma_{el} = 1.8\times10^{-12}\,\mathrm{cm}^2$, which agrees with the value measured in Ref. [16]. The temperature of the system was set to $T/T_F = 0.18$, with $T_F = 1.1\,\mu$K, which yields the Pauli suppression factor $\eta = 0.3$ [81], as well as the mean relative velocity v according to Eq. (40). To completely fix all parameters which are necessary for a self-consistent determination of the relaxation time with Eq. (37), we still need to take the appropriate value of the number of collisions α_{coll} for the given geometry, i.e., for the given angle β from Ref. [81].

Figure 10(a) shows the corresponding aspect ratios in real and momentum space for ^{167}Er during TOF expansion for $\beta = 0°$, for which the average number of collisions to rethermalize is $\alpha_{coll} = 3.2$ [81]. The red upper solid and dashed lines in Fig. 10(a) are obtained by numerically solving Eqs. (21) and (22), with the relaxation time determined self-consistently through Eq. (37). In the same plot, we also see for the sake of comparison the results for the collisionless regime in terms of the blue lower solid and dashed lines. The difference between the corresponding lines is less than 0.1%, which is certainly within the experimental error bars, and confirms that the system is indeed very close to the collisionless regime, as assumed in Ref. [39].

However, systems with a stronger DDI can easily reach the collisional regime, where a finite value for the relaxation time has to be taken into account. In order to demonstrate this, we analyze the TOF expansion of a ^{40}K ^{87}Rb dipolar Fermi gas [55], whose relative dipolar interaction strength is $\epsilon_{dd} = 0.97$, compared to $\epsilon_{dd} = 0.15$ for ^{167}Er (see Table II). Polar molecules have generically stronger electric dipole moments in comparison with the magnetic dipole moments of atoms, which is expected to yield a sensible difference in the respective aspect ratios.

In Fig. 10(b), we show the TOF expansion dynamics for ^{40}K ^{87}Rb for the same number of fermions and trap frequencies as in Ref. [39]. The temperature of the system is assumed to be $T = 350\,\mathrm{nK} = 0.3\,T_F$, as in Ref. [55], which yields the Pauli suppression factor $\eta = 0.5$ [81]. The total elastic cross section according to Eq. (39) in this case is $\sigma_{el} = 9.6\times10^{-11}\,\mathrm{cm}^2$, in agreement with the results of Ref. [67]. The average number of collisions to rethermalize is again taken to be $\alpha_{coll} = 3.2$ for $\beta = 0°$ [81]. The difference between the aspect ratios calculated using the self-consistently determined relaxation time and those calculated assuming that the system is in the collisionless regime is here around 10%, which could be clearly observed in future experiments. Furthermore, for polar

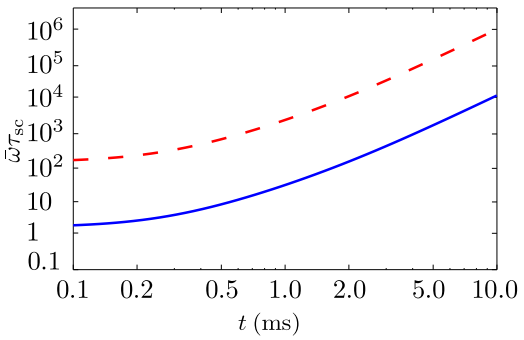

FIG. 11. Self-consistently determined relaxation time (37) as function of TOF t for ultracold Fermi gas of ^{167}Er (red dashed line) and ^{40}K ^{87}Rb (blue solid line) for $\beta = 0°$. The collisionless regime is achieved for $\bar{\omega}\tau_{sc} \gg 1$.

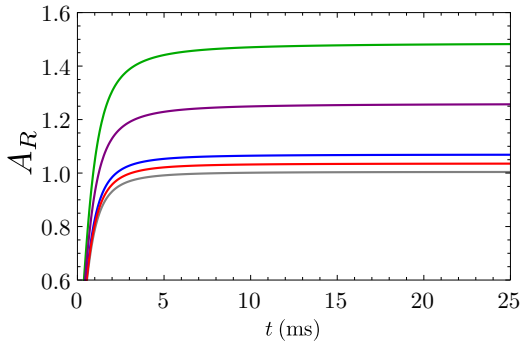

FIG. 12. Aspect ratios in real space during TOF expansion in the collisional regime with self-consistently determined relaxation time for different ultracold Fermi gases for $\beta = 0^\circ$. The curves from bottom to top correspond to ^{53}Cr (gray), ^{167}Er (red), ^{161}Dy (blue), ^{40}K ^{87}Rb (purple), and ^{167}Er ^{168}Er (green).

molecules with a stronger DDI, the differences are expected to be even more pronounced. Thus, in experiments with such systems, the relaxation time must be taken into account, for instance through the self-consistent approach presented here. We also note that the asymptotic values of aspect ratios in real and momentum space turn out to be again the same, as was already the case in the collisionless and in the hydrodynamic regimes.

Figure 11 shows the resulting time dependence of the self-consistently determined relaxation time during TOF expansion for both analyzed species, i.e., ^{167}Er (red dashed line) and ^{40}K ^{87}Rb (blue solid line). As we can see, for an atomic gas of ^{167}Er the relaxation time satisfies the condition $\bar{\omega}\tau_{\mathrm{SC}} \gg 1$ right from the beginning, which further justifies the previous conclusion that the system is always in the collisionless regime [39]. For a molecular gas of ^{40}K ^{87}Rb, however, this condition is satisfied only after 1–2 ms, so initially the system is in the collisional regime. Furthermore, we recognize that the relaxation time increases quite fast, namely faster than exponential, as we can see from the log-log plot of Fig. 11. Thus, the approximation of Sec. V C with a fixed relaxation time would clearly not be suitable, and a self-consistent approach as presented here is indispensable.

To summarize our results for the aspect ratios during the TOF expansion in the collisional regime with self-consistently determined relaxation time, in Fig. 12 we combine our results for the time dependence of aspect ratios in real space A_R for $\beta = 0^\circ$ for ^{167}Er from Fig. 10(a) and ^{40}K ^{87}Rb from Fig. 10(b) with the results for three other considered dipolar fermionic species from Table II. We see that increasing relative dipolar interaction strength leads to increasing aspect ratios after long TOF. While for ^{53}Cr, ^{167}Er, and ^{161}Dy, asymptotic values of A_R are just few percent over 1, for ^{40}K ^{87}Rb we obtain a value of about 1.26 and for ^{167}Er ^{168}Er a value of about 1.48.

VI. CONCLUSIONS

In conclusion, we have explored the properties of trapped dipolar Fermi gases at zero temperature in global equilibrium, as well as their dynamics during TOF expansion by using the Boltzmann-Vlasov formalism in the relaxation-time approximation for the collision integral. We have studied the aspect ratios of the fermionic cloud in real and momentum space, including the deformation of the Fermi sphere due to the presence of the dipole-dipole interaction. In particular, we have extended the existing theoretical models such that we could describe all experimentally relevant regimes: collisionless, collisional, and hydrodynamic.

The obtained results for the global equilibrium and the TOF expansion aspect ratios in the collisionless regime are in excellent agreement with experimental results of Ref. [39]. In the collisional regime, we have introduced an approach for self-consistently determining the relaxation time, which allows a detailed modeling of the global equilibrium and the TOF expansion in cases when the collision integral cannot be neglected. We have also shown that a strong dipole-dipole interaction, available for some experimentally accessible ultracold Fermi species, could place the system into the collisional regime, which requires using a self-consistent determination of the relaxation time presented here. Furthermore, we find that in the collisional regime the TOF dynamics can be accurately studied only if the nonballistic expansion is used, and the dipole-dipole interaction is properly taken into account not only to calculate the ground state, but also during the whole TOF. Therefore, the obtained theoretical results are relevant for designing future experiments with strongly dipolar Fermi gases, for identifying results of the corresponding TOF measurements, and for identifying effects of dipole-dipole interaction in general.

For future work, it would be of interest to go beyond Refs. [80,81] and derive more accurate results for the relaxation time from first principles. This would amount to linearizing the BV equation and treating the linearization with the rescaling technique introduced in Ref. [77]. Furthermore, the approach developed here, based on the relaxation-time approximation for the Boltzmann-Vlasov equation, can also be applied to other fields of physics. The examples include nuclear physics, such as a study of viscosity of the quark-gluon plasma [82,83] and ultrarelativistic heavy-ion collisions [84], as well as plasma physics [85], where, e.g., transient regimes of degenerate electrons can be studied using the relaxation-time approximation [86].

ACKNOWLEDGMENTS

We acknowledge L. Chomaz, F. Ferlaino, A. R. P. Lima, I. Vasić, and F. Wächtler for inspiring discussions. This work was supported in part by the Ministry of Education, Science, and Technological Development of the Republic of Serbia under Projects ON171017 and IBEC, by the German Academic and Exchange Service (DAAD) under Project IBEC, and by the German Research Foundation (DFG) via the Collaborative Research Centers SFB/TR49 and SFB/TR185. Numerical simulations were run on the PARADOX supercomputing facility at the Scientific Computing Laboratory of the Institute of Physics Belgrade.

APPENDIX A: ASPECT RATIO IN REAL SPACE

To calculate aspect ratios in real space, we use the same geometry as in Ref. [39]; see Fig. 1. The imaging plane is $x'z$;

i.e., the imaging is performed along the y' axis, which is rotated counterclockwise for an angle α with respect to the y axis. The TOF absorption images correspond to density profiles of the system, so we first calculate the particle density $n(\mathbf{r},t)$ from the Wigner quasiprobability-distribution function,

$$\begin{aligned} n(\mathbf{r},t) &= \int \frac{d\mathbf{k}}{(2\pi)^3}\nu(\mathbf{r},\mathbf{k},t) \\ &= \int \frac{d\mathbf{k}}{(2\pi)^3}\Gamma(t)\nu^0[\mathcal{R}(\mathbf{r},t),\mathcal{K}(\mathbf{r},\mathbf{k},t)] \\ &= \int \frac{d\mathbf{k}}{(2\pi)^3}\Gamma(t)\Theta\left(1-\sum_i \frac{\mathcal{R}_i^2(\mathbf{r},t)}{R_i^2}-\sum_i \frac{\mathcal{K}_i^2(\mathbf{r},\mathbf{k},t)}{K_i^2}\right), \end{aligned}$$

where expressions for $\mathcal{R}_i(\mathbf{r},t)$ and $\mathcal{K}_i(\mathbf{r},\mathbf{k},t)$ are given by Eqs. (18) and (19), respectively. Changing the momentum variables k_i to $u_i = \frac{1}{K_i\sqrt{\theta_i(t)}}(k_i - \frac{M\dot{b}_i(t)}{\hbar b_i(t)}r_i)$ and switching to spherical coordinates yields

$$\begin{aligned} n(\mathbf{r},t) = \frac{\prod_i K_i}{6\pi^2\prod_i b_i(t)}&\left(1-\sum_i \frac{r_i^2}{R_i^2 b_i^2(t)}\right)^{\frac{3}{2}} \\ &\Theta\left(1-\sum_i \frac{r_i^2}{R_i^2 b_i^2(t)}\right). \end{aligned} \tag{A1}$$

The expectation value of a quantity $Q(\mathbf{r})$ in real space is given by

$$\langle Q\rangle = \frac{1}{N}\int d\mathbf{r}\, n(\mathbf{r},t)Q(\mathbf{r}), \tag{A2}$$

so we immediately obtain that the expectation values of the coordinates vanish: $\langle r_i\rangle = 0$. Therefore, the size in the ith direction of an atomic or molecular cloud in real space is described in terms of the root mean squares $\sqrt{\langle r_i^2\rangle}$. Using the expression (A1) for the particle density, the corresponding expectation values are found to be

$$\langle r_i^2\rangle = \frac{1}{N}\int d\mathbf{r}\, n(\mathbf{r},t)r_i^2 = \frac{1}{8}R_i^2 b_i(t). \tag{A3}$$

Since the imaging is performed in the $x'z$ plane, the aspect ratio in real space is defined by

$$A_R(t) = \sqrt{\frac{\langle r_z^2\rangle}{\langle r_x'^2\rangle}}, \tag{A4}$$

so we also need to calculate the expectation value $\langle r_x'^2\rangle$, where $(r_x',r_y',r_z) = (r_x\cos\alpha + r_y\sin\alpha, r_y'\cos\alpha - r_x\sin\alpha, r_z)$. After a straightforward but tedious calculation, we get

$$\langle r_x'^2\rangle = \tfrac{1}{8}\left[R_x^2 b_x^2(t)\cos^2\alpha + R_y^2 b_y^2(t)\sin^2\alpha\right], \tag{A5}$$

and finally the aspect ratio (A4) is given by

$$A_R(t) = \frac{R_z b_z(t)}{\sqrt{R_x^2 b_x^2(t)\cos^2\alpha + R_y^2 b_y^2(t)\sin^2\alpha}}. \tag{A6}$$

Note that in the Innsbruck experiment [39] the angle α had the value $\alpha = 28^\circ$.

APPENDIX B: ASPECT RATIO IN MOMENTUM SPACE

In order to describe effects of the DDI on the Fermi surface, we use an aspect ratio in momentum space, which is defined similarly as the aspect ratio in real space. First, we calculate the particle density in momentum space $n(\mathbf{k},t)$ from the Wigner quasiprobability-distribution function,

$$\begin{aligned} n(\mathbf{k},t) &= \int d\mathbf{r}\,\nu(\mathbf{r},\mathbf{k},t) \\ &= \int d\mathbf{r}\,\Gamma(t)\nu^0[\mathcal{R}(\mathbf{r},t),\mathcal{K}(\mathbf{r},\mathbf{k},t)] \\ &= \int d\mathbf{r}\,\Gamma(t)\Theta\left(1-\sum_i \frac{\mathcal{R}_i(\mathbf{r},t)^2}{R_i^2}-\sum_i \frac{\mathcal{K}_i(\mathbf{r},\mathbf{k},t)^2}{K_i^2}\right), \end{aligned}$$

where again expressions for $\mathcal{R}_i(\mathbf{r},t)$ and $\mathcal{K}_i(\mathbf{r},\mathbf{k},t)$ are given by Eqs. (18) and (19), respectively. After a change of spatial variables r_i according to $u_i = \frac{D_i(t)r_i}{R_i b_i(t)} - \frac{MR_i\dot{b}_i(t)k_i}{\hbar K_i^2\theta_i(t)D_i}$ with $D_i(t) = \sqrt{1+\frac{M^2R_i^2\dot{b}_i^2(t)}{\hbar^2K_i^2\theta_i(t)}}$, we switch to spherical coordinates and obtain

$$\begin{aligned} n(\mathbf{k},t) = \frac{4\pi}{3}\frac{\prod_i R_i}{\prod_i\sqrt{\theta_i(t)}D_i(t)}&\left(1-\sum_i \frac{k_i^2}{K_i^2\theta_i(t)D_i^2(t)}\right)^{\frac{3}{2}} \\ &\Theta\left(1-\sum_i \frac{k_i^2}{K_i^2\theta_i(t)D_i^2(t)}\right). \end{aligned} \tag{B1}$$

The expectation value of a variable $Q(\mathbf{k})$ in momentum space is given by

$$\langle Q\rangle = \frac{1}{N}\int \frac{d\mathbf{k}}{(2\pi)^3}\, n(\mathbf{k},t)Q(\mathbf{k}), \tag{B2}$$

so we get $\langle k_i\rangle = 0$ and the cloud sizes in momentum space are also defined by root mean squares $\sqrt{\langle k_i^2\rangle}$. The corresponding expectation values can be explicitly calculated and yield

$$\langle k_i^2\rangle = \frac{1}{N}\int \frac{d\mathbf{k}}{(2\pi)^3}\, n(\mathbf{k},t)k_i^2 = \frac{1}{8}\left(K_i^2\theta_i(t) + \frac{M^2R_i^2\dot{b}_i^2(t)}{\hbar^2}\right), \tag{B3}$$

where we have used the same variable change as above, as well as Eq. (5). The aspect ratio in momentum space is defined as

$$A_K(t) = \sqrt{\frac{\langle k_z^2\rangle}{\langle k_x'^2\rangle}}, \tag{B4}$$

where $(k_x',k_y',k_z) = (k_x\cos\alpha + k_y\sin\alpha, k_y'\cos\alpha - k_x\sin\alpha, k_z)$. After a lengthy calculation we get

$$\langle k_x'^2\rangle = \tfrac{1}{8}\left[D_x^2K_x^2\theta_x(t)\cos^2\alpha + D_y^2K_y^2\theta_y(t)\sin^2\alpha\right], \tag{B5}$$

and finally the momentum space aspect ratio (B4) reduces to

$$A_K(t) = \sqrt{\frac{\hbar^2 K_z^2 \theta_z(t) + M^2 R_z^2 \dot{b}_z^2(t)}{\left[\hbar^2 K_x^2 \theta_x(t) + M^2 R_x^2 \dot{b}_x^2(t)\right]\cos^2\alpha + \left[\hbar^2 K_y^2 \theta_y(t) + M^2 R_y^2 \dot{b}_y^2(t)\right]\sin^2\alpha}}\,. \tag{B6}$$

[1] C. J. Pethick and H. Smith, *Bose-Einstein Condensation in Dilute Gases*, 2nd ed. (Cambridge University Press, Cambridge, UK, 2008).
[2] L. Pitaevskii and S. Stringari, *Bose-Einstein Condensation and Superfluidity*, 2nd ed. (Oxford University Press, Oxford, UK, 2016).
[3] L. Santos, G. V. Shlyapnikov, and M. Lewenstein, Phys. Rev. Lett. **90**, 250403 (2003).
[4] K. Glaum, A. Pelster, H. Kleinert, and T. Pfau, Phys. Rev. Lett. **98**, 080407 (2007).
[5] K. Glaum and A. Pelster, Phys. Rev. A **76**, 023604 (2007).
[6] M. Baranov, Phys. Rep. **464**, 71 (2008).
[7] T. Lahaye, C. Menotti, L. Santos, M. Lewenstein, and T. Pfau, Rep. Prog. Phys. **72**, 126401 (2009).
[8] L. D. Carr and J. Ye, New J. Phys. **11**, 055009 (2009).
[9] C. Krumnow and A. Pelster, Phys. Rev. A **84**, 021608(R) (2011).
[10] J. K. Block, N. T. Zinner, and G. M. Bruun, New J. Phys. **14**, 105006 (2012).
[11] A. I. Nicolin, Proc. Rom. Acad. Ser. A-Math. Phys. **14**, 35 (2013).
[12] B. Nikolić, A. Balaž, and A. Pelster, Phys. Rev. A **88**, 013624 (2013).
[13] H. Al-Jibbouri, I. Vidanović, A. Balaž, and A. Pelster, J. Phys. B **46**, 065303 (2013).
[14] A. Balaž, R. Paun, A. I. Nicolin, S. Balasubramanian, and R. Ramaswamy, Phys. Rev. A **89**, 023609 (2014).
[15] M. Ghabour and A. Pelster, Phys. Rev. A **90**, 063636 (2014); S. K. Adhikari, *ibid.* **88**, 043603 (2013); J. Phys. B: At. Mol. Opt. Phys. **46**, 115301 (2013); **45**, 235303 (2012).
[16] A. Frisch, M. Mark, K. Aikawa, S. Baier, R. Grimm, A. Petrov, S. Kotochigova, G. Quéméner, M. Lepers, O. Dulieu, and F. Ferlaino, Phys. Rev. Lett. **115**, 203201 (2015).
[17] B. Gadway and B. Yan, J. Phys. B **49**, 152002 (2016).
[18] J. Stuhler, A. Griesmaier, T. Koch, M. Fattori, T. Pfau, S. Giovanazzi, P. Pedri, and L. Santos, Phys. Rev. Lett. **95**, 150406 (2005).
[19] H. Kadau, M. Schmitt, M. Wenzel, C. Wink, T. Maier, I. Ferrier-Barbut, and T. Pfau, Nature (London) **530**, 194 (2016).
[20] P. Muruganandam and S. Adhikari, Comput. Phys. Commun. **180**, 1888 (2009).
[21] D. Vudragović, I. Vidanović, A. Balaž, P. Muruganandam, and S. K. Adhikari, Comput. Phys. Commun. **183**, 2021 (2012).
[22] R. K. Kumar, L. E. Young-S., D. Vudragović, A. Balaž, P. Muruganandam, and S. K. Adhikari, Comput. Phys. Commun. **195**, 117 (2015).
[23] V. Lončar, A. Balaž, A. Bogojević, S. Škrbić, P. Muruganandam, and S. K. Adhikari, Comput. Phys. Commun. **200**, 406 (2016).
[24] B. Satarić, V. Slavnić, A. Belić, A. Balaž, P. Muruganandam, and S. K. Adhikari, Comput. Phys. Commun. **200**, 411 (2016).
[25] L. E. Young-S., D. Vudragović, P. Muruganandam, S. K. Adhikari, and A. Balaž, Comput. Phys. Commun. **204**, 209 (2016).
[26] A. R. P. Lima and A. Pelster, Phys. Rev. A **84**, 041604(R) (2011).
[27] A. R. P. Lima and A. Pelster, Phys. Rev. A **86**, 063609 (2012).
[28] R. N. Bisset and P. B. Blakie, Phys. Rev. A **92**, 061603(R) (2015).
[29] I. Ferrier-Barbut, H. Kadau, M. Schmitt, M. Wenzel, and T. Pfau, Phys. Rev. Lett. **116**, 215301 (2016).
[30] P. B. Blakie, Phys. Rev. A **93**, 033644 (2016).
[31] K.-T. Xi and H. Saito, Phys. Rev. A **93**, 011604(R) (2016).
[32] F. Wächtler and L. Santos, Phys. Rev. A **93**, 061603 (2016).
[33] F. Wächtler and L. Santos, Phys. Rev. A **94**, 043618 (2016).
[34] R. N. Bisset, R. M. Wilson, D. Baillie, and P. B. Blakie, Phys. Rev. A **94**, 033619 (2016).
[35] D. Baillie, R. M. Wilson, R. N. Bisset, and P. B. Blakie, Phys. Rev. A **94**, 021602 (2016).
[36] L. Chomaz, S. Baier, D. Petter, M. J. Mark, F. Wächtler, L. Santos, and F. Ferlaino, Phys. Rev. X **6**, 041039 (2016).
[37] M. Schmitt, M. Wenzel, F. Böttcher, I. Ferrier-Barbut, and T. Pfau, Nature (London) **539**, 259 (2016).
[38] T. Miyakawa, T. Sogo, and H. Pu, Phys. Rev. A **77**, 061603 (2008).
[39] K. Aikawa, S. Baier, A. Frisch, M. Mark, C. Ravensbergen, and F. Ferlaino, Science **345**, 1484 (2014).
[40] T. Sogo, L. He, T. Miyakawa, S. Yi, H. Lu, and H. Pu, New J. Phys. **11**, 055017 (2009).
[41] T. Sogo, L. He, T. Miyakawa, S. Yi, H. Lu, and H. Pu, New J. Phys. **12**, 079801 (2010).
[42] J.-N. Zhang, R.-Z. Qiu, L. He, and S. Yi, Phys. Rev. A **83**, 053628 (2011).
[43] D. Baillie and P. B. Blakie, Phys. Rev. A **86**, 023605 (2012).
[44] A. R. P. Lima and A. Pelster, Phys. Rev. A **81**, 021606(R) (2010).
[45] A. R. P. Lima and A. Pelster, Phys. Rev. A **81**, 063629 (2010).
[46] F. Wächtler, A. R. P. Lima, and A. Pelster, arXiv:1311.5100 [cond-mat.quant-gas].
[47] M. Abad, A. Recati, and S. Stringari, Phys. Rev. A **85**, 033639 (2012).
[48] B. Liu and L. Yin, Phys. Rev. A **84**, 053603 (2011).
[49] J. Krieg, P. Lange, L. Bartosch, and P. Kopietz, Phys. Rev. A **91**, 023612 (2015).
[50] P. Lange, J. Krieg, and P. Kopietz, Phys. Rev. A **93**, 033609 (2016).
[51] B. Naylor, A. Reigue, E. Maréchal, O. Gorceix, B. Laburthe-Tolra, and L. Vernac, Phys. Rev. A **91**, 011603(R) (2015).
[52] K. Aikawa, A. Frisch, M. Mark, S. Baier, R. Grimm, and F. Ferlaino, Phys. Rev. Lett. **112**, 010404 (2014).
[53] M. Lu, N. Q. Burdick, and B. L. Lev, Phys. Rev. Lett. **108**, 215301 (2012).
[54] J. W. Park, S. A. Will, and M. W. Zwierlein, Phys. Rev. Lett. **114**, 205302 (2015).
[55] K.-K. Ni, S. Ospelkaus, M. H. G. de Miranda, A. Pe'er, B. Neyenhuis, J. J. Zirbel, S. Kotochigova, P. S. Julienne, D. S. Jin, and J. Ye, Science **322**, 231 (2008).

[56] N. V. Vitanov, A. A. Rangelov, B. W. Shore, and K. Bergmann, Rev. Mod. Phys. **89**, 015006 (2017).
[57] J. W. Park, S. A. Will, and M. W. Zwierlein, New J. Phys. **17**, 075016 (2015).
[58] E. Kuznetsova, M. Gacesa, P. Pellegrini, S. F. Yelin, and R. Ct, New J. Phys. **11**, 055028 (2009).
[59] P. D. Gregory, P. K. Molony, M. P. Kppinger, A. Kumar, Z. Ji, B. Lu, A. L. Marchant, and S. L. Cornish, New J. Phys. **17**, 055006 (2015).
[60] W. P. Schleich, *Quantum Optics in Phase Space* (Wiley-VCH, Berlin, 2005).
[61] A. Bogojević, A. Balaž, and A. Belić, Phys. Rev. E **72**, 036128 (2005).
[62] A. Bogojević, I. Vidanović, A. Balaž, and A. Belić, Phys. Lett. A **372**, 3341 (2008).
[63] I. Vidanović, A. Bogojević, A. Balaž, and A. Belić, Phys. Rev. E **80**, 066706 (2009).
[64] A. Balaž, I. Vidanović, A. Bogojević, A. Belić, and A. Pelster, J. Stat. Mech. (2011) P03004.
[65] A. Balaž, I. Vidanović, A. Bogojević, A. Belić, and A. Pelster, J. Stat. Mech. (2011) P03005.
[66] D. Baillie, R. N. Bisset, and P. B. Blakie, Phys. Rev. A **91**, 013613 (2015).
[67] J. L. Bohn, M. Cavagnero, and C. Ticknor, New J. Phys. **11**, 055039 (2009).
[68] V. Baran, M. Colonna, V. Greco, and M. D. Toro, Phys. Rep. **410**, 335 (2005).
[69] R. Tabacu, M. R. Raportaru, E. Slusanschi, V. Baran, and A. I. Nicolin, Rom. J. Phys. **60**, 1441 (2015).
[70] Z. L. Petrović, Z. M. Raspopović, S. Dujko, and T. Makabe, Appl. Surf. Sci. **192**, 1 (2002).
[71] S. Dujko, U. Ebert, R. D. White, and Z. L. Petrović, Jpn. J. Appl. Phys. **50**, 08JC01 (2011).
[72] K. Dusling and T. Schäfer, Phys. Rev. A **84**, 013622 (2011).
[73] P.-A. Pantel, D. Davesne, and M. Urban, Phys. Rev. A **91**, 013627 (2015).
[74] S. Chiacchiera, T. Lepers, D. Davesne, and M. Urban, Phys. Rev. A **79**, 033613 (2009).
[75] S. Chiacchiera, T. Lepers, D. Davesne, and M. Urban, Phys. Rev. A **84**, 043634 (2011).
[76] L. P. Kadanoff and G. Baym, *Quantum Statistical Mechanics* (Benjamin, New York, 1962).
[77] P. Pedri, D. Guéry-Odelin, and S. Stringari, Phys. Rev. A **68**, 043608 (2003).
[78] Y. Castin and R. Dum, Phys. Rev. Lett. **77**, 5315 (1996).
[79] S. Giorgini, L. P. Pitaevskii, and S. Stringari, Rev. Mod. Phys. **80**, 1215 (2008).
[80] J. L. Bohn and D. S. Jin, Phys. Rev. A **89**, 022702 (2014).
[81] K. Aikawa, A. Frisch, M. Mark, S. Baier, R. Grimm, J. L. Bohn, D. S. Jin, G. M. Bruun, and F. Ferlaino, Phys. Rev. Lett. **113**, 263201 (2014).
[82] M. Bluhm, B. Kämpfer, and K. Redlich, J. Phys.: Conf. Ser. **270**, 012062 (2011).
[83] W. Florkowski, R. Ryblewski, and M. Strickland, Phys. Rev. D **86**, 085023 (2012).
[84] W. Florkowski, *Phenomenology of Ultra-relativistic Heavy-Ion Collisions* (World Scientific, Singapore, 2010).
[85] J. A. Bittencourt, *Fundamentals of Plasma Physics*, 3rd ed. (Springer, New York, 2004).
[86] K. F. Brennan, *The Physics of Semiconductors with Applications to Optoelectronic Devices* (Cambridge University Press, Cambridge, UK, 1999).

Q 35: Quantum Gases (Fermions) I

Time: Wednesday 14:00–16:15 Location: S HS 037 Informatik

Group Report Q 35.1 Wed 14:00 S HS 037 Informatik

Beyond particle transport at an atomic quantum point contact: thermoelectric effects and spin control — Martin Lebrat, •Philipp Fabritius, Samuel Häusler, Dominik Husmann, Jeff Mohan, Tilman Esslinger, and Laura Corman — Departmen of Physics, ETH Zurich, 8093 Zurich, Switzerland

In this talk, we report on a few remarkable transport properties of lithium-6 atoms through a quantum point contact (QPC) precisely defined by a set of optical potentials. The versatility of cold-atom techniques allows us to directly measure heat or spin currents and to tune interatomic interactions.

In a first experiment performed with a unitary Fermi gas close to the superfluid transition, we probe the thermoelectric effects induced by a temperature difference accross the QPC. We show that the system evolves towards a non-equilibrium steady state, associated with a reduced heat diffusion and a strong violation of the Wiedemann-Franz law. In a second experiment performed with weakly interacting atoms, we locally lift the spin degeneracy of atoms inside the QPC using an optical tweezer tuned very close to atomic resonance. We observe quantized, spin-polarized transport that is robust to dissipation and sensitive to interaction effects on the scale of the Fermi length.

These results open the way to the quantum simulation of efficient thermoelectric and spintronic devices with cold atoms.

Q 35.2 Wed 14:30 S HS 037 Informatik

Transverse magnetization effect of the spin-imbalanced Hofstadter-Hubbard model — •Bernhard Irsigler, Jun-Hui Zheng, Mohsen Hafez-Torbati, and Walter Hofstetter — Institut für Theoretische Physik, Frankfurt am Main, Germany

We spin-imbalance the fermionic, time-reversal invariant Hofstadter-Hubbard model through a population difference between two spin states. In the strongly interacting regime, where the system can be described by an effective spin model, we find an exotic spin structure by means of classical Monte-Carlo calculations. Remarkably, this spin structure exhibits a finite transverse net magnetization perpendicular to the magnetization induced by the population imbalance. We further investigate effects of quantum fluctuations within the dynamical mean-field approximation and obtain a rich phase diagram including ferromagnetic, anti-ferromagnetic, and ferrimagnetic phases, where the latter emerges from strong interaction induced quantum entanglement.

Q 35.3 Wed 14:45 S HS 037 Informatik

Degenerate Fermi gases of polar molecules with tilted dipoles — •Vladimir Veljić[1], Axel Pelster[2], and Antun Balaž[1] — [1]Scientific Computing Laboratory, Center for the Study of Complex Systems, Institute of Physics Belgrade, University of Belgrade, Serbia — [2]Research Center OPTIMAS and Department of Physics, Technische Universität Kaiserslautern, Germany

A recent experimental realization of an ultracold quantum degenerate gas of ^{40}K^{87}Rb molecules [1] opens up a new chapter in exploring strongly dipolar Fermi gases. This includes the deformation of the Fermi surface (FS) for polarized systems, where the electric dipoles have a preferential orientation. Compared to atomic magnetic species [2,3], this effect is significantly increased in ultracold Fermi gases of polar molecules, and the stability of the system is expected to strongly depend on its geometry. Here we generalize a previous Hartree-Fock mean-field theory [2] for the Wigner function, which now takes into account that the cloud shape in the ground state is determined not only by the trap frequencies, but also by the dipoles' orientation. We calculate the corresponding FS deformation for an arbitrary orientation of the dipoles, demonstrating the great promise for the exploration of polarized degenerate molecules.

[1] L. De Marco, G. Valtolina, K. Matsuda, W. G. Tobias, J. P. Covey, and J. Ye, arXiv:1808.00028 (2018).
[2] V. Veljić, A. R. P. Lima, L. Chomaz, S. Baier, M. J. Mark, F. Ferlaino, A. Pelster, and A. Balaž, New J. Phys. **20**, 093016 (2018).
[3] V. Veljić, A. Balaž, and A. Pelster, Phys. Rev. A **95**, 053635 (2017).

Q 35.4 Wed 15:00 S HS 037 Informatik

A few-body approach to pairing correlations in a two-dimensional Fermi gas — •Ralf Klemt, Jan Hendrik Becher, Ram-Janik Petzold, Philipp M. Preiss, and Selim Jochim — Physikalisches Institut der Universität Heidelberg, Im Neuenheimer Feld 226, 69120 Heidelberg

Strong pairing correlations are, in combination with a shell structure, the central mechanism leading to the structure of atomic and nuclear matter but are also key to understanding the nature of strongly correlated fermionic many-body-phases as seen for example in the framework of the BEC-BCS crossover.

In this talk, I present recent experimental efforts on realizing and probing deterministic few-body states of fermionic ^6Li in a two-dimensional geometry. In the presence of strong interactions, it was theoretically shown [1] that such a system features signatures which can be interpreted as the few-body precursor of a normal to superfluid transition. As a consequence, in this superfluid phase strong pairing correlations at the "Fermi-surface", reminiscent of Cooper-pairing in many-body systems, are present.

We will characterize such few-body systems by probing the excitation spectrum of the pairing mode as well as by directly observing single particle resolved spin-spin correlations in momentum space. However, the unique opportunity to directly observe all relevant correlations will also help bridging the gap toward the understanding of strongly interacting fermionic 2D systems in the many-body limit.

[1] J. Bjerlin et al., PRL. 116, 155302 (2016)

Q 35.5 Wed 15:15 S HS 037 Informatik

Diverging exchange force for ultracold fermionic atoms — •Christian Schilling[1] and Rolf Schilling[2] — [1]Clarendon Laboratory, University of Oxford — [2]Institut für Physik, Johannes Gutenberg-Universität Mainz

The Pauli exclusion principle $0 \leq n_k \leq 1$ is a kinematical constraint on fermionic occupation numbers which strongly shapes the behavior and the properties of fermionic quantum systems on all length scales. We demonstrate that this fundamental restriction can also be interpreted dynamically: the fermionic exchange symmetry manifests itself in the one-fermion picture in the form of an "exchange force" which repulsively diverges on the boundary of the allowed region, preventing fermionic occupation numbers n_k from leaving their domain $0 \leq n_k \leq 1$. Moreover, for translationally invariant one-band lattice models (e.g. ultracold atoms in an optical lattice), we exploit the *ab initio* knowledge of the natural orbitals (momentum states) and discover the exact one-matrix functional $\mathcal{F}(\vec{n})$ for smaller cluster systems (such as the Hubbard square). Remarkably, $\mathcal{F}(\vec{n})$ turns out to be strongly shaped by Pauli's exclusion principle and its recently found generalization.

Q 35.6 Wed 15:30 S HS 037 Informatik

High-Contrast Interference of Ultracold Fermions — •Jan Hendrik Becher, Philipp M. Preiss, Ralf Klemt, Vincent Klinkhamer, Andrea Bergschneider, and Selim Jochim — Physics Institute, Heidelberg University, Germany

Many-body interference between indistinguishable particles induces strong correlations rooted in quantum statistic. Such correlations have been studied with few photons but are thus limited to massless, non-interacting systems. Using deterministically prepared fermionic atoms in optical tweezers, such experiments can be extended to a higher particle number and further correlations can be induced by tuning the interactions over a wide range.

In our experiment we assemble mesoscopic fermionic quantum systems from independently prepared optical tweezers. We combine the full control of the system with a single-atom, spin-resolved imaging scheme that allows us to extract momentum correlation functions up to third order.

I will present recent measurements on momentum correlations between three independently prepared, identical fermions. The observed correlations are purely induced by quantum statistics and are a consequence of the particles' indistinguishability. We measure and analyze two and three-body density correlations after time-of-flight and find that even non-interacting, identical fermions exhibit intrinsic three-body correlations that cannot be predicted from measured two-body correlation functions.

Q 35.7 Wed 15:45 S HS 037 Informatik

Stability diagram of degenerate Fermi gases of polar molecules with tilted dipoles

V. Veljić[1], A. Pelster[2], and A. Balaž[1]

[1]Scientific Computing Laboratory, Center for the Study of Complex Systems, Institute of Physics Belgrade, University of Belgrade, Serbia
[2] Physics Department and Research Center OPTIMAS, Technical University of Kaiserslautern, Germany

A recent experimental realization of an ultracold quantum degenerate gas of $^{40}K^{87}Rb$ molecules [1] opens up a new chapter in exploring strongly dipolar Fermi gases and many-body phenomena arising in that regime. This includes the deformation of the Fermi surface (FS) for polarized systems, where the electric dipoles have a preferential orientation, which can be achieved using an external field. Compared to atomic magnetic species [2,3], this effect is significantly increased in ultracold Fermi gases of polar molecules, and the stability of the system is expected to strongly depend on its geometry. Here we generalize a previous Hartree-Fock mean-field theory [2] for the Wigner function, which now takes into account that the cloud shape in the ground state is determined not only by the trap frequencies, but also by the dipoles' orientation. In the special case of a spherically symmetric trap, the cloud is elongated in the direction of the dipoles, similar to the FS. We obtain here a universal stability diagram for dipolar fermions and calculate the corresponding FS deformation for an arbitrary orientation of the dipoles, demonstrating the great promise for the exploration of degenerate molecules in electric fields, where the strong dipole-dipole interaction dominates. These results are important for designing future experiments with polar molecules, as well as for the interpretation of measured data, including the dynamics and the time-of-flight expansion.

References

[1] L. De Marco, G. Valtolina, K. Matsuda, W. G. Tobias, J. P. Covey, and J. Ye, arXiv:1808.00028 (2018).

[2] V. Veljić, A. R. P. Lima, L. Chomaz, S. Baier, M. J. Mark, F. Ferlaino, A. Pelster, and A. Balaž, New J. Phys. **20**, 093016 (2018).

[3] V. Veljić, A. Balaž, and A. Pelster, Phys. Rev. A **95**, 053635 (2017).

Ground state of an ultracold Fermi gas of tilted dipoles

V. Veljić[1], A. R. P. Lima[2], L. Chomaz[3], S. Baier[3], M. J. Mark[3,4], F. Ferlaino[3,4], A. Pelster[5], and Antun Balaž[1]

[1]*Scientific Computing Laboratory, Center for the Study of Complex Systems, Institute of Physics Belgrade, University of Belgrade, Serbia*
[2]*Universidade da Integração Internacional da Lusofonia Afro-Brasileira, Campus das Auroras, Acarape-Ceará, Brazil*
[3]*Institute for Experimental Physics, University of Innsbruck, Innsbruck, Austria*
[4]*Institute for Quantum Optics and Quantum Information, Austrian Academy of Sciences, Innsbruck, Austria*
[5]*Physics Department and Research Center OPTIMAS, TU Kaiserslautern, Germany*

Many-body dipolar effects in Fermi gases are quite subtle as they energetically compete with the large kinetic energy at and below the Fermi surface (FS). Recently it was experimentally observed in a sample of erbium atoms that its FS is deformed from a sphere to an ellipsoid due to the presence of the anisotropic and long-range dipole-dipole interaction [1]. Moreover, it was suggested that, when the dipoles are rotated by means of an external field, the Fermi surface follows their rotation, thereby keeping the major axis of the momentum-space ellipsoid parallel to the dipoles. Here we generalize a previous Hartree-Fock mean-field theory [2] to systems confined in an elongated triaxial trap with an arbitrary orientation of the dipoles relative to the trap. With this we study for the first time the effects of the dipoles' arbitrary orientation on the ground-state properties of the system [3]. Furthermore, taking into account the geometry of the system, we show how the ellipsoidal FS deformation can be reconstructed, assuming ballistic expansion, from the experimentally measurable real-space aspect ratio after a free expansion. We compare our theoretical results with new experimental data measured with erbium Fermi gas for various trap parameters and dipole orientations. The observed remarkable agreement demonstrates the ability of our model to capture the full angular dependence of the FS deformation. Moreover, for systems with even higher dipole moment, our theory predicts an additional unexpected effect: the FS does not simply follow rigidly the orientation of the dipoles, but softens showing a change in the aspect ratio depending on the dipoles' orientation relative to the trap geometry, as well as on the trap anisotropy itself. Our theory provides the basis for understanding and interpreting phenomena in which the investigated physics depends on the underlying structure of the FS, such as fermionic pairing and superfluidity.

References

[1] K. Aikawa, et al., Science **345**, 1484 (2014).
[2] V. Veljić, A. Balaž, and A. Pelster, Phys. Rev. A **95**, 053635 (2017).
[3] V. Veljić, et al., arXiv:1806.05672 (2018).

Poster 30

Ground state of an ultracold Fermi gas of tilted dipoles

Vladimir Veljić,[1] Aristeu R. P. Lima,[2] Lauriane Chomaz,[3] Simon Baier,[3]
Manfred J. Mark,[3,4] Francesca Ferlaino,[3,4] Axel Pelster,[5,*] and Antun Balaž[1]

[1] *Center for the Study of Complex Systems, Institute of Physics Belgrade, University of Belgrade, Serbia*
[2] *University for International Integration of the Afro-Brazilian Lusophony, Brazil*
[3] *Institute for Experimental Physics, University of Innsbruck, Austria*
[4] *Institute for Quantum Optics and Quantum Information, Austrian Academy of Sciences, Innsbruck, Austria*
[5] *Physics Department and Research Center OPTIMAS, Technische Universität Kaiserslautern, Germany*

Many-body dipolar effects in Fermi gases are quite subtle as they energetically compete with the large kinetic energy at and below the Fermi surface (FS). Recently it was experimentally observed in a sample of erbium atoms that its FS is deformed from a sphere to an ellipsoid due to the presence of the anisotropic and long-range dipole-dipole interaction [1]. Moreover, it was suggested that, when the dipoles are rotated by means of an external field, the Fermi surface follows their rotation, thereby keeping the major axis of the momentum space ellipsoid parallel to the dipoles. Here we generalise a previous Hartree-Fock mean-field theory [2, 3] to systems confined in an elongated triaxial trap with an arbitrary orientation of the dipoles relative to the trap. With this we study for the first time the effects of the dipoles' arbitrary orientation on the ground-state properties of the system. Furthermore, taking into account the geometry of the system, we show how the ellipsoidal FS deformation can be reconstructed, assuming ballistic expansion, from the experimentally measurable real-space aspect ratio after a free expansion. We perform new and extensive measurements for various parameters to study the full angular dependence of the FS deformation and show that the FS does not simply follow rigidly the orientation of the dipoles, but depends additionally on the dipoles' orientation relative to the trap geometry, as well as on the trap anisotropy itself, see the illustration in Fig. 1. The presented direct comparison of the obtained analytical and numerical results with our experimental observations shows very good agreement. The developed theory is relevant for understanding and interpreting future experiments

* axel.pelster@physik.uni-kl.de

with ultracold fermionic dipolar quantum gases, where the investigated physics depends on the underlying structure of the FS.

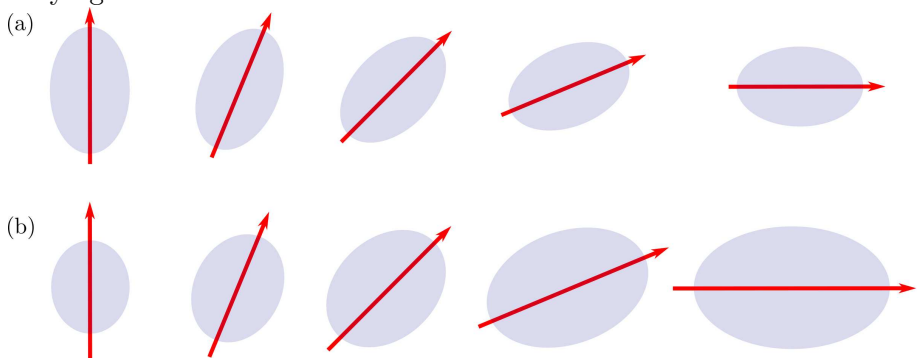

Fig. 1: Illustration of angular dependence of FS deformation in momentum space for system in anisotropic trap: (a) for weak DDI, when FS ellipsoid just rotates like a rigid object; (b) for strong DDI, when FS deformation strongly depends on dipoles' orientation.

---

[1] K. Aikawa, S. Baier, A. Frisch, M. Mark, C. Ravensbergen, and F. Ferlaino, Science **345**, 1484 (2014).

[2] F. Wächtler, A.R.P. Lima, and A. Pelster, Phys. Rev. A **96**, 043608 (2017).

[3] V. Veljić, A. Balaž, and A. Pelster, Phys. Rev. A **95**, 053635 (2017).

Abstract Submitted
for the DAMOP18 Meeting of
The American Physical Society

Ground state of a Fermi gas with tilted dipoles[1] ANTUN BALAZ, VLADIMIR VELJIC, Institute of Physics Belgrade, Serbia, ARISTEU R. P. LIMA, University for International Integration of the Afro-Brazilian Lusophony, Brazil, SIMON BAIER, LAURIANE CHOMAZ, University of Innsbruck, Austria, FRANCESCA FERLAINO, University of Innsbruck and IQOQI of Austrian Academy of Sciences, Innsbruck, Austria, AXEL PELSTER, Physics Department and Research Center OPTIMAS, Technical University of Kaiserslautern, Germany
— In the presence of an anisotropic and long-range dipole-dipole interaction, the Fermi sphere of an ultracold Fermi gas deforms into an ellipsoid. Recently, it was experimentally observed in such systems that the shape of the Fermi surface follows the rotation of the dipoles when they are tilted [1]. Here we generalize the Hartree-Fock mean-field theory of Refs. [2, 3], where the dipoles were assumed to be parallel to one of the trap axes, to an arbitrary orientation of the dipoles and obtain the ground-state Thomas-Fermi radii and momenta. The calculated angular dependence of the Fermi surface deformation shows good agreement with experimental observations. We also find that the angular dependence of the aspect ratio turns out to be a direct consequence of the dipole tilting.
[1] K. Aikawa, et al., Science **345**, 1484 (2014).
[2] F. Wächtler, et al., Phys. Rev. A **96**, 043608 (2017).
[3] V. Veljić, et al., Phys. Rev. A **95**, 053635 (2017).

[1]ON171017 and BEC-L by Serbian Ministry of Education, Science and Technological Development; BEC-L by DAAD; SFB/TR49 and SFB/TR185 by DFG

Antun Balaz
Institute of Physics Belgrade, Serbia

Date submitted: 05 Feb 2018 Electronic form version 1.4

Q 25: Quantum Gases (Fermions) I

Time: Monday 16:15–18:00 Location: K 1.022

Q 25.1 Mon 16:15 K 1.022

Probing homogeneous two-dimensional Fermi gases in momentum space — •Lennart Sobirey, Niclas Luick, Klaus Hueck, Fynn Förger, Jonas Siegl, Thomas Lompe, and Henning Moritz — Institut für Laserphysik, Universität Hamburg, Luruper Chaussee 149, 22761 Hamburg, Germany

Ultracold two-dimensional Fermi gases are uniquely suited to investigate the interplay of reduced dimensionality and strong interactions in quantum many-body systems. Here, we report on our realization of an ultracold 2D Fermi gas trapped in a homogeneous disk-shaped potential. This system is ideally suited to measure non-local quantities such as correlation functions and the momentum distribution. Furthermore, homogeneous systems simplify the creation of quantum phases which exist only in narrow regions of the phase diagram. To confine the homogeneous gas, we radially confine it by a ring-shaped blue-detuned beam with steep walls. We perform matter wave focusing to extract its momentum distribution and directly observe Pauli blocking in a near unity occupation of momentum states.

Q 25.2 Mon 16:30 K 1.022

Ground State of a Fermi Gas with Tilted Dipoles — •Vladimir Veljić[1], Aristeu R. P. Lima[2], Simon Baier[3], Lauriane Chomaz[3], Francesca Ferlaino[4,5], Axel Pelster[5], and Antun Balaž[1] — [1]Center for the Study of Complex Systems, Institute of Physics Belgrade, University of Belgrade, Serbia — [2]University for International Integration of the Afro-Brazilian Lusophony, Brazil — [3]Institute for Experimental Physics, University of Innsbruck, Austria — [4]Institute for Quantum Optics and Quantum Information, Austrian Academy of Sciences, Innsbruck, Austria — [5]Physics Department and Research Center OPTIMAS, Technical University of Kaiserslautern, Germany

In the presence of an anisotropic and long-range dipole-dipole interaction, the Fermi sphere of an ultracold Fermi gas deforms into an ellipsoid. Recently, it was experimentally observed in such systems that the shape of the Fermi surface follows the rotation of the dipoles when they are tilted [1]. Here we generalize the Hartree-Fock mean-field theory of Refs. [2, 3], where the dipoles were assumed to be parallel to one of the trap axes, to an arbitrary orientation of the dipoles and obtain the ground-state Thomas-Fermi radii and momenta. The calculated angular dependence of the Fermi surface deformation shows good agreement with experimental observations. We also find that the angular dependence of the aspect ratio turns out to be a direct consequence of the dipole tilting.

[1] K. Aikawa, et al., Science **345**, 1484 (2014).
[2] F. Wächtler, et al., Phys. Rev. A **96**, 043608 (2017).
[3] V. Veljić, et al., Phys. Rev. A **95**, 053635 (2017).

Q 25.3 Mon 16:45 K 1.022

High temperature pairing in a strongly interacting two-dimensional Fermi gas — •Luca Bayha[1], Puneet Murthy[1], Mathias Neidig[1], Ralf Klemt[1], Igor Boettcher[2], Tilman Enss[3], Marvin Holten[1], Gerhard Zürn[1], Philipp Preiss[1], and Selim Jochim[1] — [1]Physikalisches Institut, Universität Heidelberg — [2]Department of Physics, Simon Fraser University — [3]Institut für Theoretische Physik, Universität Heidelberg

Understanding the nature of the normal phase of strongly correlated Fermi systems is a fascinating open question in many-body physics.
In this talk I will present recent measurements, where we observe many-body pairing in a strongly interacting quasi two-dimensional ultracold Fermi gas at temperatures far above critical temperature for superfluidity. We employ spatially resolved radio-frequency spectroscopy to probe the pairing energy in the system. We identify and study a regime in the normal phase, where the pairing gap shows a clear density dependence and significantly exceeds the intrinsic two-body binding energy. This implies that pairing in this regime is driven by many-body correlations, rather than two-body physics. These correlations are remarkably robust against thermal fluctuations, as the effects persist up to temperatures close to the Fermi-temperature.

Q 25.4 Mon 17:00 K 1.022

Anomalous breaking of scale invariance in a two-dimensional Fermi gas — •Marvin Holten, Luca Bayha, Antonia Klein, Puneet Murthy, Philipp Preiss, and Selim Jochim — Physikalisches Institut, University of Heidelberg, Germany

The frequency of the breathing mode of a classical, two-dimensional Fermi gas in a harmonic confinement is fixed by the scale invariance of the Hamiltonian. On the quantum mechanical level, however, scale invariance is broken by introducing the two dimensional scattering length a_{2D} as a regulator. This is an example for a quantum anomaly in the field of ultracold atoms and leads to a shift of the frequency of the collective breathing mode of the cloud. In this talk, I present our experimental study of this frequency shift for a two component Fermi gas in the strongly interacting regime. We observe a significant shift away from the scale invariant result that depends on both interactions and temperature. A careful consideration of all the additional terms that may lead to explicit breaking of scale invariance is required to distinguish those from the effects caused by the anomaly.

Q 25.5 Mon 17:15 K 1.022

Violation of the Wiedemann-Franz law in a unitary Fermi gas — •Samuel Häusler, Dominik Husmann, Martin Lebrat, Philipp Fabritius, Laura Corman, Jean-Philippe Brantut, and Tilman Esslinger — Institute for Quantum Electronics, ETH Zurich, 8093 Zürich, Switzerland

In materials heat and particle transport are often coupled, leading to thermoelectric effects. A temperature gradient may cause particle transport (Seebeck effect) and a variation in chemical potential can induce heat currents (Peltier effect). These phenomena are suited to probe the fundamental excitations that are challenging to identify in strongly correlated matter.

To study these phenomena, we prepare a system consisting of two reservoirs of fermionic lithium atoms at unitarity close to the superfluid transition. After heating one of the reservoirs they may exchange particles and heat through a quantum point contact. We observe a violent initial particle current from cold to hot that brings the system to a non-equilibrium steady state where currents vanish in the presence of finite temperature difference and chemical potential bias. The steady state reveals a finite particle and suppressed thermal conductance strongly violating the Wiedemann-Franz law, which relates the two conductances by a universal number in the limit of low temperatures. This violation signals a breakdown of Fermi liquid behaviour and remains for wider channel geometries, where the system relaxes back to equilibrium. These findings are related to the celebrated fountain effect in bosonic helium II.

Q 25.6 Mon 17:30 K 1.022

Observation of the Higgs mode in the superfluid BEC-BCS crossover in Fermi gases — •Johannes Kombe, Jean-Sébastien Bernier, and Corinna Kollath — Uni Bonn, Nussallee 14-16, 53115 Bonn

Thanks to recent advances, investigating the non-equilibrium dynamics of interacting systems is now possible. Using time-dependent perturbations, one can probe from a different angle the mechanisms responsible for the collective phenomena present in correlated systems. Taking advantage of this progress, we investigate both theoretically and experimentally the evolution of a three-dimensional Fermi gas while the interaction strength is effectively modified. Our study, carried out on the BCS side, reveals various collective excitations. Interestingly, this approach highlights the presence of the Higgs mode.

Q 25.7 Mon 17:45 K 1.022

Spinor Gases of Fermionic Erbium Atoms — •Jan Hendrik Becher[1,3], Simon Baier[1], Lauriane Chomaz[1,2], Gabriele Natale[1], Daniel Petter[1], Manfred Mark[1,2], and Francesca Ferlaino[1,2] — [1]Institut für Experimentalphysik, Universität Innsbruck, Austria — [2]Institut für Quantenoptik und Quanteninformation, Innsbruck, Austria — [3]Physikalisches Institut, Heidelberg University, Germany

Over the last decade, dipolar quantum gases have become an ideal system to study novel phenomena in ultracold quantum physics. In particular, strongly magnetic atomic species, such as erbium, open fascinating possibilities to investigate dipole-dipole interaction (DDI) and its impact on few- and many-body effects in ultracold spinor gases.

Here we report on first experimental investigations of spin physics in fermionic erbium, ^{167}Er. Due to its large quantum numbers, fermionic

erbium has a remarkably large number of spin states in the lowest level manifold, $F = 19/2$. The 20 different m_F states interact via both contact and DDI. The DDI is violating spin conservation and effects the dynamics of out-of-equilibrium spin systems.

In the experiment, we create a spin polarized, degenerate Fermi gas in the absolute lowest Zeeman sublevel. We then load the atomic sample into a 3D optical lattice and start spin preparation by applying a radio frequency pulse. In this setting, we study the interaction in the proximity of homonuclear p-wave Feshbach resonances and discover new interspin Feshbach resonances. Furthermore we investigate the dynamics of spin excitations in the frozen-particle regime.

Ground State of a Fermi Gas with Tilted Dipoles

V. Veljić[1], A.R.P. Lima[2], A. Balaž[1], and A. Pelster[3]

[1] *Scientific Computing Laboratory, Center for the Study of Complex Systems, Institute of Physics Belgrade, University of Belgrade, Serbia*
[2] *University for International Integration of the Afro-Brazilian Lusophony, Brazil*
[3] *Physics Department and Research Center OPTIMAS, Technical University of Kaiserslautern, Germany*
E-mail: vveljic@ipb.ac.rs

In the presence of an isotropic interactions, the Fermi surface of an ultracold Fermi gas is spherical. Introducing anisotropic and long-range dipole-dipole interaction to the system deforms the Fermi surface to an ellipsoid. Recently, it was experimentally observed in a degenerate dipolar Fermi gas of erbium atoms that the shape of the atomic cloud follows the rotation of the dipoles when they are tilted [1]. Here we generalize the Hartree-Fock mean-field theory of Refs. [2, 3], where the magnetic field was assumed to be parallel to one of the axes of the harmonic trap. To this end, we extend the calculations for an arbitrary orientation of the dipoles and obtain the ground state by minimizing the total energy of the system, which allows to determine its Thomas-Fermi radii and momenta. The angle dependence of the Fermi surface deformation, presented in Fig. 1(a), shows that it is almost constant, in good agreement with experimental observation. Contrary to that, the angle dependence of the aspect ratio, presented in Fig. 1(b) together with the experimental data of Ref. [1], turns out to be a direct consequence of tilting of the dipoles. These analytical and numerical calculations agree quantitatively well with experimental observations from the Innsbruck experiment [1] and are relevant for understanding similar ongoing experiments with ultracold fermionic dipolar atoms.

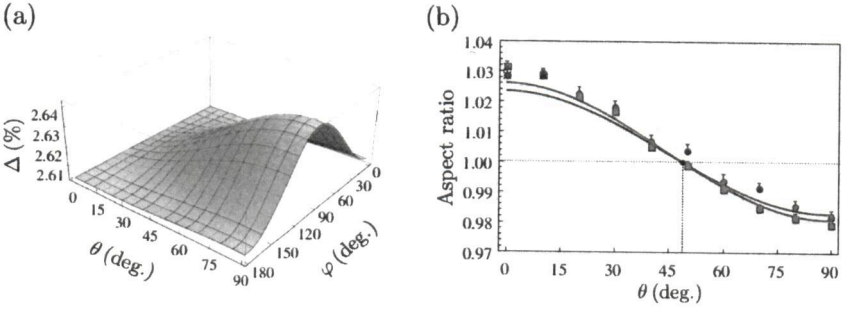

References

[1] K. Aikawa, et al., Science **345**, 1484 (2014).
[2] F. Waechtler, A. R. P. Lima, and A. Pelster, Phys. Rev. A (in press).
[3] V. Veljić, A. Balaž, and A. Pelster, Phys. Rev. A **95**, 053635 (2017).

Deformation of the Fermi Surface

Vladimir Veljić[1], Antun Balaž[1]and Axel Pelster[2]
[1]*Scientific Computing Laboratory, Center for the Study of Complex Systems, Institute of Physics Belgrade, University of Belgrade, Serbia*
[2]*Physics Department and Research Center OPTIMAS, Technical, University of Kaiserslautern, Germany*
e-mail: vveljic@ipb.ac.rs

In the presence of isotropic interactions, the Fermi surface of an ultracold Fermi gas is spherical. Introducing anisotropic and long-range dipole-dipole interaction (DDI) to the system deforms the Fermi surface to an ellipsoid, as was experimentally observed in a degenerate dipolar Fermi gas of erbium atoms [1]. The deformation is caused by the interplay between the strong magnetic DDI and the Pauli exclusion principle. It was also observed that the atomic cloud follows the rotation of the dipoles when the direction of the external magnetic field is changed, keeping the major axis always parallel to the direction of the maximum attraction of the DDI. Here we present a generalization of the previous Hartree-Fock mean-field theory [2, 3], where the magnetic field was assumed to be parallel to one of the harmonic trap axes. We now extend our calculations for an arbitrary orientation of the magnetic field. In order to obtain the ground state and analyze the resulting deformation of the Fermi surface, we minimize the total energy of the system, which enables us to determine its Thomas-Fermi radii and momenta. These analytical and numerical calculations are in agreement with observations from the Innsbruck experiment [1] and are relevant for understanding similar ongoing experiments with ultracold fermionic dipolar atoms.

REFERENCES

[1] K. Aikawa, et al., Science **345**, 1484 (2014).
[2] F. Wächtler, A. R. P. Lima, and A. Pelster, eprint arXiv:1311.5100 (2013).
[3] V. Veljić, A. Balaž,and A. Pelster, Phys. Rev. A **95**, 053635 (2017).

Austria

We study the dynamics of an F=1 spinor Bose-Einstein condensate in one spatial dimension out of equilibrium by means of semi-classical simulations. Our main focus lies on sudden quenches within the paramagnetic phase, where the system is quenched near the critical point of a phase transition by varying an external magnetic field. The time evolution of the resulting non-equilibrium state including quantum effects is studied within the framework of the truncated Wigner approximation. To this end, the coupled Gross-Pitaevskii equations for the fundamental fields are solved numerically using higher-order time-splitting Fourier pseudospectral methods. We observe the formation of soliton-like excitations and study their link to the build-up of correlations in the system. By continuously tuning the interaction away from an integrable point of the system, we further investigate the effects of non-integrability on the observed dynamics. Our results are put into relation with the concept of non-thermal fixed points and critical phenomena.

Q 31.8 Tue 17:00 P OGs

Dynamics of a one-dimensional two-component Bose gas quenched to criticality. — •Martin Rabel, Markus Karl, and Thomas Gasenzer — Kirchhoff-Institut für Physik, Im Neuenheimer Feld 227, 69120 Heidelberg, Germany

We study the dynamics of a two-component Bose gas after a parameter quench into the proximity of a quantum critical point using analytical, real-time effective-action techniques. The relative degrees of freedom within the system can be described by a quasi-spin 1/2 model. This model is subject to a mean-field paramagnetic to ferromagnetic quantum phase transition. For the full model this corresponds to a transition from a miscible to an immiscible phase. The transition is investigated in a dynamical setup: The initial state is the ground-state configuration far away from criticality. Following a sudden quench to criticality the time evolution of the emerging spin fluctuations is analysed. In the one-dimensional system under investigation, the non-vanishing energy introduced by the quench leads to a finite correlation length during the induced time evolution. The finite critical correlation length is determined within a leading-order $1/N$ approximation. The obtained analytical results are compared with Truncated-Wigner numerical simulations.

Q 31.9 Tue 17:00 P OGs

Goldstone mode in the quench dynamics of an ultracold BCS Fermi gas: A full Bogoliubov-de Gennes approach — •Peter Kettmann[1], Simon Hannibal[1], Mihail Croitoru[2], Vollrath Martin Axt[3], and Tilmann Kuhn[1] — [1]Institute of Solid State Theory, University of Münster — [2]Condensed Matter Theory, University of Antwerp — [3]Theoretical Physics III, University of Bayreuth

Ultracold Fermi gases are a convenient system to probe and study the properties of phases like the BEC and the BCS phase and the crossover in between those regimes. In particular, ultracold Fermi gases can be used as a test bed to study the two fundamental dynamical modes –the Higgs and the Goldstone mode– which result from spontaneous symmetry breaking in these phases.

We investigate the Goldstone mode in the dynamics of a cigar-shaped cloud of ultracold ^{6}Li after an interaction quench on the BCS side of the BCS-BEC crossover. To this end, we numerically solve Heisenberg's equations of motion for the Bogoliubov single-particle excitations in the framework of the Bogoliubov-de Gennes (BdG) formalism. Extending previous studies, we use a full BdG approach instead of the truncated Anderson solution. This improves the validity in the strong-coupling regime and ensures a correct coupling of the Goldstone mode to the trapping potential.

We study the impact of this extension on the dynamics of the single-particle excitations and find an overall good qualitative agreement of both solutions. However, some significant deviations occur predominantly in the case of strong coupling.

Q 31.10 Tue 17:00 P OGs

Universal scaling and non-thermal fixed points in spin systems — •Stefanie Czischek[1], Halil Cakir[1], Markus Karl[1], Michael Kastner[2], Markus K. Oberthaler[1], and Thomas Gasenzer[1] — [1]Kirchhoff-Institut für Physik, Im Neuenheimer Feld 227, 69120 Heidelberg, Germany — [2]Institute of Theoretical Physics, University of Stellenbosch, Stellenbosch 7600, South Africa

We study the dynamical build-up of correlations after sudden quenches in spin systems using the discrete truncated Wigner approximation. In particular, we consider quenches from large external fields into the vicinity of a quantum critical point within the paramagnetic phase. We calculate correlation lengths and study their time evolution at different distances from the critical point. For the transverse-field Ising chain, we find that the discrete truncated Wigner approximation is in good agreement with exact analytical and numerical results. Our exact results show that the correlation function takes the form given by a generalized Gibbs ensemble already after short times and small relative distances, which is also found in the discrete truncated Wigner approximation. The agreement of both results for quenches into the vicinity of the critical point suggests that the discrete truncated Wigner approximation may be used to determine the correlation dynamics after quenches for spin systems which are not exactly solvable, in one and higher dimensions.

Q 31.11 Tue 17:00 P OGs

Probing Relaxation at the Many-Body Localization Transition with Ultracold Fermions in Optical Lattices — •Sebastian Scherg[1,2], Henrik Lüschen[1,2], Pranjal Bordia[1,2], Ulrich Schneider[1,2,3], and Immanuel Bloch[1,2] — [1]Ludwig-Maximilians-Universität, Schellingstr. 4, 80799 München, Germany — [2]Max-Planck-Institut für Quantenoptik, Hans-Kopfermann-Str. 1, 85748 Garching, Germany — [3]Cavendish Laboratory, University of Cambridge, J. J. Thomson Avenue, Cambridge CB3 0HE, United Kingdom

The phenomenon of Many-Body Localization (MBL) describes a generic non-thermalizing phase in which quantum information can persist locally up to infinite times. This phase is separated from a phase obeying the Eigenstate Thermalization Hypothesis via a disorder driven, dynamical phase transition, which happens not only in the ground state but over an extended range of excited states. While the dynamical structure deep in the MBL phase is arguably well understood in one dimension, there is a paucity of results close to the critical point and in higher dimensions.

In this work, we report on the observation of MBL in one and two dimensions. We directly probe the transition points finding critically slow relaxation below the critical disorder strength in both 1D and 2D. The slow dynamics in 1D can be attributed to Griffiths type effects. We highlight the importance of interactions, which strongly govern the behavior around the critical point.

Q 31.12 Tue 17:00 P OGs

Sub-Doppler laser cooling of fermionic 40K atoms in gray optical molasses — •Max Hachmann, Robert Büchner, Raphael Eichberger, and Andreas Hemmerich — Institut für Laser-Physik, Universität Hamburg

Most experiments on quantum degenerate gases begin with a laser cooling phase that is followed by evaporative cooling in a conservative trap. The final quantum degeneracy strongly depends on the temperature at the end of the laser cooling phase and sub-Doppler cooling is often a key ingredient for initiating efficient evaporation. In our experiment for fermionic 40K a cooling cycle on the D2 transition for a bright optical molasses has been used. However, 40 K features a narrow hyperfine structure in the excited state of the D2 transition that hinders efficient sub-Doppler cooling by cooling to the red of this transition. The same is true for other isotopes of potassium and lithium. To overcome this limitation a gray molasses cooling scheme on the D1 transition at 770 nm can be implemented to produce cold and dense atomic samples. Here we report on the current progress of the experimental implementation.

Q 31.13 Tue 17:00 P OGs

Fermi Surface Deformation in Dipolar Fermi Gases — •Vladimir Veljić[1], Antun Balaž[1], and Axel Pelster[2] — [1]Scientific Computing Laboratory, Center for the Study of Complex Systems, Institute of Physics Belgrade, University of Belgrade, Serbia — [2]Physics Department and Research center OPTIMAS, Technical University of Kaiserslautern, Germany

In a recent time-of-flight (TOF) expansion experiment with ultracold polarized fermionic erbium atoms, TOF images show that the atomic cloud has an ellipsoidal shape, with an elongation in the direction of atomic dipoles [1]. The Hartree-Fock mean-field theory presented in Refs. [2,3], which was restricted to the orientation of dipoles along one of the harmonic trap axes, is generalized here for an arbitrary orientation of dipoles. Afterwards, using this approach we analyze the resulting Fermi surface deformation, calculate TOF dynamics, and solve the corresponding Boltzmann-Vlasov equation within the relaxation-time approximation in the vicinity of a new equilibrium configuration by

using a suitable rescaling of the equilibrium distribution. The resulting ordinary differential equations of motion for the scaling parameters are solved numerically for experimentally relevant parameters at zero temperature. A comparison of our analytical and numerical results with the Innsbruck experimental results [1] is also presented.
[1] K. Aikawa, et al., Science **345**, 1484 (2014).
[2] F. Wächtler, A.R.P. Lima, and A. Pelster, `arXiv:1311.5100` (2013).
[3] V. Veljić, A. Balaž, and A. Pelster, `arXiv:1608.06448` (2016).

Q 31.14 Tue 17:00 P OGs

Towards second sound in a quasi two dimensional Fermi gas — •Daniel Hoffmann, Thomas Paintner, Wolfgang Limmer, and Johannes Hecker Denschlag — Universität Ulm, Institut für Quantenmaterie, Deutschland

Excitations in ultracold quantum gases have become a versatile tool to unveil fundamental thermodynamics. Especially the properties of superfluidity have been investigated extensively using local or global excitations. One phenomena which has recently been demonstrated in a quantum gas experiment is second sound excitation (see [1]). In this experiment entropy waves were excited in a suprafluid/normal fluid mixture and were detected by means of density modulation.

In the project presented here, we extend the work on second sound to quasi two dimensional gases. We use a degenerate Fermi gas of ^{6}Li loaded into a highly anisotropic trap, where the conditions of a quasi 2D Fermi gas can be fulfilled. To excite second sound, we use an intensity-modulated laser beam focused on the trap center to generate entropy waves. Detecting density modulations in the Fermi gas enables us to extract the second sound excitation. Our presentation shows first results towards second sound in a quasi 2D interacting Fermi gas.

[1]: Sidorenkov et al., Nature 498, 78-81 (2013)

Q 31.15 Tue 17:00 P OGs

Quench dynamics and equilibrium behavior in a spinless Fermi-Hubbard ladder with dipolar interactions — •Philipp Fabritius and Shannon Whitlock — Physikalisches Institut, Universität Heidelberg, Im Neuenheimer Feld 226, 69120 Heidelberg

We report on theoretical simulations of a spinless Fermi-Hubbard model on a two-leg ladder with anisotropic long-range dipolar interactions. Using a density-matrix renormalization group approach we obtain the quantum phase diagram. We also present results on the dynamical evolution of the system following a quantum quench from an insulating to an interlayer superfluid phase. These results have relevance for future experiments which aim to use quantum gas microscopy to reveal exotic superfluid and magnetic phases with ultracold atoms.

Q 31.16 Tue 17:00 P OGs

An experiment to initialize and study the Fermi-Hubbard model atom by atom — •Phillip Wieburg, Kai Morgener, Thomas Lompe, and Henning Moritz — Institut für Laserphysik, Universität Hamburg, Luruper Chaussee 149, 22761 Hamburg, Germany

Investigating the Fermi-Hubbard model with cold atoms is typically done by evaporatively cooling an ultracold Fermi gas and loading it into a large optical lattice. In contrast, we plan to build up a Fermi-Hubbard system site by site using optical microtraps. Each microtrap will contain a single atom cooled to the vibrational ground state by Raman-sideband cooling. This technique combines fast experimental cycle times with single site addressability and detection and allows studying the fundamental processes governing the Fermi-Hubbard model in a bottom-up approach.

Here we report upon the commissioning of this new experiment, which is going to be able to cool a gas of 40K to quantum degeneracy as well as to directly lasercool single atoms into optical microtraps. We have already lasercooled 39K and 40K atoms and trapped them magnetically. Further cooling of the atoms will be performed using Raman-sideband cooling [1,2]. In order to image and to manipulate the atoms with high spatial resolution, our setup is equipped with a novel type achromatic imaging system located inside the vacuum chamber.

[1] A.M. Kaufman et al., Physical Review X 2 041014 (2012).
[2] L. W. Cheuk et al., Phys. Rev. Lett. 114, 193001 (2015).

Q 31.17 Tue 17:00 P OGs

Anomalous heating in ion traps: where does the noise originate? — •Carsten Henkel[1], Henning Kaufmann[2], and Ulrich Poschinger[2] — [1]Universität Potsdam — [2]Johannes-Gutenberg-Universität Mainz

Trapped ions that are laser-cooled to the ground state of a Paul trap provide a promising platform for quantum information processing and surface analysis. The ions are subject to fluctuating electric fields emanating from the surrounding electrodes which lead to a finite heating rate whose detailed behaviour is not yet fully understood (patch potentials, surface adsorbates, temperature and distance dependence ...)[1]. Building on a recent model with metallic electrodes covered by a thin lossy dielectric [2], we investigate the spatial distribution of the charge fluctuations that generate the electric field noise. We analyze for example the interference that is at the origin of the maximum of noise for films with a certain thickness [3, 4]. The aim is to mitigate anomalous heating with suitably coated electrodes that screen the dominant noise sources.

[1] M. Brownnutt, M. Kumph, P. Rabl, and R. Blatt, Rev. Mod. Phys. 87 (2015) 1419
[2] M. Kumph, C. Henkel, P. Rabl, M. Brownnutt, and R. Blatt, New J. Phys. 18 (2016) 023020
[3] S. Bauer, Am. J. Phys. 60 (1992) 257
[4] S. A. Biehs, D. Reddig, and M. Holthaus, Eur. Phys. J. B 55 (2007) 237; S. A. Biehs, Eur. Phys. J. B 58 (2007) 423

Q 31.18 Tue 17:00 P OGs

A hybrid atom-ion trap for ultracold Li and Yb$^+$ — •Jannis Joger[1], Henning Fürst[1], Norman Ewald[1], Thomas Secker[2], Thomas Feldker[1], and Rene Gerritsma[1] — [1]Institute of Physics, University of Amsterdam, Netherlands — [2]Institute for Coherence and Quantum Technology, TU Eindhoven, Netherlands

Our setup for realising a hybrid system of ultra-cold atoms and ions is presented. This setup allows studying the quantum dynamics of mixtures of fermionic atoms and ions. Recent experiments have shown that the time-dependent trapping field of the ions can cause heating in hybrid atom-ion systems [1]. One way to mitigate this problem is to employ ion-atom combinations with a large mass ratio [2]. The highest convenient mass ratio - for species that still allow for straightforward laser cooling - is achieved by using the combination ^{171}Yb$^+$ and ^{6}Li.

Combining ion trapping technology with ultra-cold lithium poses particular challenges that we address on this poster. We present numerical simulations showing that the s-wave limit may be reached in our setup, opening up the possibility of studying atom-ion Feshbach resonances [3] and show our first experimental results of atom-ion interactions.

[1] Z. Meir et al., arXiv:1603.01810 (2016)
[2] M. Cetina et al., Phys. Rev. Lett. 109, 253201 (2012).
[3] M. Tomza, C.P. Koch and R. Moszynski, Phys. Rev. A 91, 042706 (2015).

Q 31.19 Tue 17:00 P OGs

Laser cooling of Dysprosium — •Niels Petersen, Florian Mühlbauer, Carina Baumgärtner, Lena Maske, and Patrick Windpassinger — QUANTUM, Institut für Physik, Johannes Gutenberg-Universität Mainz, Staudingerweg 7, 55128 Mainz, Germany

Ultra-cold dipolar quantum gases enable the study of many-body physics with long-range, inhomogeneous interaction effects due to the anisotropic character of the dipole-dipole interaction. These systems are expected to show novel exotic quantum phases and phase transitions which can be studied with dysprosium atoms. Dysprosium is a rare-earth element with one of the largest ground-state magnetic moments (10 Bohr magnetons) in the periodic table. Therefore, the dipole-dipole interaction is not a small perturbation but becomes comparable in strength to the s-wave scattering. This influences significantly the physical properties of the trapped atomic sample, such as its shape and stability.

This poster presents the current status of our experimental setup to generate dysprosium quantum gases. We discuss the relevant properties of dysprosium and present our laser system and vacuum design. We present spectroscopic measurements of the relevant cooling transitions and show our progress towards laser cooling of dysprosium atoms in a magneto optical trap.

Q 31.20 Tue 17:00 P OGs

The role of particle (in-)distinguishability for many-particle dynamics in optical lattices — •Tobias Brünner, Gabriel Dufour, Alberto Rodriguez, and Andreas Buchleitner — Physikalisches Institut, Universität Freiburg, Hermann-Herder-Str. 3, D-79104 Freiburg, Germany

Much attention has been dedicated so far to the dynamical impact of

Cloud Shape of Dipolar Fermi Gases

Vladimir Veljić[1], Antun Balaž[1], and Axel Pelster[2]

[1]Scientific Computing Laboratory, Institute of Physics Belgrade, University of Belgrade, Pregrevica 118, 11080 Belgrade, Serbia
[2]Physics Department and Research center OPTIMAS, Technical University of Kaiserslautern, 67663 Kaiserslautern, Germany
E-mail: vladimir.veljic@ipb.ac.rs

In a recent time-of-flight (TOF) expansion experiment for ultracold polarized fermionic erbium atoms it was shown that the Fermi surface has an ellipsoidal shape [1]. It was also observed that the Fermi surface follows a rotation of the dipoles, which is induced by changing the direction of the external magnetic field, keeping the major axis always parallel to the direction of maximal attraction of the dipole-dipole interaction. Here we present a theory for determining the cloud shape in both real and momentum space by extending the work of Ref. [2], where the magnetic field is oriented along one of the harmonic trap axes, to an arbitrary orientation of the magnetic field. In order to analyze the cloud shape within TOF dynamics, we solve analytically the corresponding Boltzmann-Vlasov equation by using a suitable rescaling of the equilibrium distribution [3]. The resulting ordinary differential equations of motion for the scaling parameters are solved numerically in the collisionless regime at zero temperature and turn out to agree with the observations in the Innsbruck experiment [1].

References

[1] K. Aikawa et al., Science **345**, 1484 (2014).
[2] F. Wächtler, A. R. P. Lima, and A. Pelster, arXiv:1311.5100 (2013).
[3] P. Pedri, D. Guery-Odelin, and S. Stringari, Phys. Rev. A **68**, 043608 (2003).

53115 Bonn

We study the excitation spectrum of the ionic Hubbard model. The ionic Hubbard model consists of three terms: a nearest-neighbor tunneling, an onsite interaction and an alternating energy offset between even and odd sites. It was originally introduced for the description of condensed matter systems, e.g. mixed stacked organic compounds, and can be cleanly realized by ultracold fermionic atoms confined to an optical superlattice. Its phase diagram in one dimension has attracted considerable theoretical interest. In the limits of predominating energy offset or onsite interaction strength, the ground state is a band insulator or Mott insulator, respectively. In between a narrow so-called bond-ordered wave phase has been predicted which spontaneously breaks site-inversion symmetry. The excitation spectrum of the ionic Hubbard model has attracted much less attention so far. We exert a time-periodic modulation of the superlattice amplitude and study the exact time-dependence within the time-dependent density matrix renormalization group method. Our study is motivated by the possibilities of experimental probing in cold atomic gas experiments where our choice of perturbation corresponds to lattice amplitude modulation spectroscopy of superlattice geometry.

Q 58.82 Thu 16:30 Empore Lichthof

A Laser System for Cooling of Yb Atoms — •Benjamin Nagler, Tobias Eul, Carsten Lippe, Benjamin Gänger, Jan Phieler, Thomas Pinnel, Christina Weirich, and Artur Widera — Technische Universität Kaiserslautern, Fachbereich Physik und Landesforschungszentrum Optimas, Erwin-Schrödinger-Str. 46, 67663 Kaiserslautern, Germany

Quantum gases have proven useful tools to gain insight into fundamental phenomena of quantum physics. The working horse for preparation of these systems is laser cooling of dilute atomic gases. Here we report on the current state of preparing an ultracold gas of Ytterbium atoms, focusing on the laser system developed. This features blue light generation by second harmonic generation several hundreds of MHz detuned from the atomic transition for operating a Zeeman slower, stabilized onto an atomic resonance. We will show key features of the laser system and present measurements of the system characteristics.

Q 58.83 Thu 16:30 Empore Lichthof

Fermionic many-body states under the microscope — •Daniel Greif[1], Maxwell F. Parsons[1], Anton Mazurenko[1], Christie S. Chiu[1], Sebastian Blatt[1,2], Florian Huber[1], Geoffrey Ji[1], and Markus Greiner[1] — [1]Department of Physics, Harvard University, Cambridge, Massachusetts 02138, USA — [2]Max-Planck-Institut für Quantenoptik, 85748 Garching, Germany

We report on site-resolved imaging of various fermionic many-body states of ultracold Li-6 in a square optical lattice, including metallic, Mott-insulating and band-insulating phases. The insulating states show a suppression in the single-site occupation variance and a spatially constant filling fraction. A comparison to theory shows that the system is in global thermal equilibrium with fitted global entropies of $1.0\,k_{\mathrm{B}}$. We also report on our most recent progress towards probing magnetically ordered quantum states with the quantum gas microscope.

Q 58.84 Thu 16:30 Empore Lichthof

Cloud Shape of Dipolar Fermi Gases — •Vladimir Veljić[1], Antun Balaž[1], Aristeu R. P. Lima[2], and Axel Pelster[3] — [1]Scientific Computing Laboratory, Institute of Physics Belgrade, University of Belgrade, Serbia — [2]UNILAB, Brazil — [3]Physics Department and Research Center OPTIMAS, Technical UIniversity of Kaiserslautern, Germany

In a recent time-of-flight (TOF) expansion experiment for ultracold polarized fermionic erbium atoms it was shown that the Fermi surface has an ellipsoidal shape [1]. It was also observed that the Fermi surface follows a rotation of the dipoles, which is induced by changing the direction of the external magnetic field, keeping the major axis always parallel to the direction of maximal attraction of the dipole-dipole interaction. Here we present a theory for determining the cloud shape in both real and momentum space by extending the work of Ref. [2], where the magnetic field is oriented along one of the harmonic trap axes, to an arbitrary orientation of the magnetic field. In order to analyze the cloud shape within TOF dynamics, we solve analytically the corresponding Boltzmann-Vlasov equation by using a suitable rescaling of the equilibrium distribution [3]. The resulting ordinary differential equations of motion for the scaling parameters are solved numerically in the collisionless regime at zero temperature and turn out to agree with the observations in the Innsbruck experiment [1].

[1] K. Aikawa, et al., Science **345**, 1484 (2014).
[2] F. Wächtler, A. R. P. Lima, and A. Pelster, `arXiv:1311.5100`.
[3] P. Pedri, et al., Phys. Rev. A **68**, 043608 (2003).

Q 58.85 Thu 16:30 Empore Lichthof

Development of a digital phase lock for optical lattices — •Dominik Vogel, Nick Fläschner, Matthias Tarnowski, Benno Rem, Christof Weitenberg, and Klaus Sengstock — Universität Hamburg, Germany

Non-separable optical lattices feature new physics as for example Dirac cones and Berry phases in the case of the hexagonal lattice, which is formed by three interfering beams. Usually, the lattice beams pass through optical fibers for optimal beam profiles and therefore pick up independent phases, which translate the lattice potential and thus couple acoustic noise to the ensemble of ultra cold atoms, leading to heating.

In this poster, we present a digital phase locked loop that fixes those phases by controlling the laser frequencies via AOMs. The loop features a 800 kS/s bipolar analog to digital converter, a real time processor and a DDS frequency source. Our setup enables a total feeback signal delay under 2 micro seconds, while providing the high linewidth quality of a DDS-source, which is superior to conventional analog phase locks. In closed loop, we achieve a significant reduction of the phase noise, which is expected to increase the atomic life time in the optical lattice and thus provides access to new temperature regimes.

Q 58.86 Thu 16:30 Empore Lichthof

Towards quantum gas microscopy of ultracold potassium atoms — •Tobias Wintermantel, Emil Pavlov, Alda Arias, Stephan Helmrich, and Shannon Whitlock — Physikalisches Institut, Universität Heidelberg, Im Neuenheimer Feld 226, 69120 Heidelberg

Ultracold quantum gases in optical lattices are a versatile model system for engineering many-body quantum systems. Additionally, the advent of single-atom-resolution imaging techniques enables one to extract an unprecedented degree of information on the spatial correlations.

We are constructing a new experiment featuring fermionic or bosonic potassium atoms in optical lattices with reduced dimensional confinement. A special aspect will be the ability to introduce and control long-range interactions between the atoms via optical dressing of Rydberg states. A high-resolution imaging setup for probing these quantum gases, mainly consisting of an in-vacuum high-NA objective lens and a high quantum efficiency EMCCD camera, is currently under construction. The expected imaging quality depends, on the one hand, on the constraints of the imaging system (numerical aperture, aberrations and detector noise) and on the other hand, on physical constraints such as the number of photons which can be scattered before the atoms are heated and lost out of the microtraps. We present our progress in quantifying these effects for imaging Rydberg-dressed quantum fluids.

Q 58.87 Thu 16:30 Empore Lichthof

Density dependent synthetic magnetism — •Sebastian Greschner[1], Daniel Huerga[2], Gaoyong Sun[1], Dario Poletti[3], and Luis Santos[1] — [1]Institut für Theoretische Physik, Leibniz Universität Hannover, Germany — [2]Institut fur Theoretische Physik III, Stuttgart — [3]Engineering Product Development, Singapore University of Technology and Design

Raman-assisted hopping can allow for the creation of density-dependent synthetic magnetism for ultracold neutral gases in optical lattices. In 1D the density-dependent Peierls phases can be mapped the anyon Hubbard model which exhibits a rich groundstate physics including unconventional two-component superfluid phases and statistically driven phase transitions [1]. In 2D square lattices we observe a non-trivial interplay between density modulations and effective magnetic fluxes as well as intriguing dynamical properties [2].

[1] S. Greschner and L. Santos, Phys. Rev. Lett. 115, 053002, 2015
[2] S. Greschner, D. Huerga, G. Sun, D. Poletti, and L. Santos, Phys. Rev. B 92, 115120, 2015

Q 58.88 Thu 16:30 Empore Lichthof

Heteronuclear Spin-Changing-Collisions in Li-Na mixtures — •Arno Trautmann, Fabián Olivares, Marcell Gall, Fred Jendrzejewski, and Markus K. Oberthaler — Kirchhoff-Institut für Physik, Im Neuenheimer Feld 227, 69120 Heidelberg

Q 61: Quantum Gases: Fermions II

Time: Friday 11:00–13:15 Location: e001

Q 61.1 Fri 11:00 e001

Realizing state-dependent optical lattices for ultracold fermions by periodic driving — •Frederik Görg[1], Gregor Jotzu[1], Michael Messer[1], Daniel Greif[1,2], Rémi Desbuquois[1], and Tilman Esslinger[1] — [1]Institute for Quantum Electronics, ETH Zurich, 8093 Zurich, Switzerland — [2]Department of Physics, Harvard University, Cambridge, Massachusetts 02138, USA

Ultracold atoms in optical lattices offer the possibility to engineer specific Hamiltonians with widely tunable properties. Recently, time-modulated optical lattices have been used to dynamically control the atomic tunnelling and to realize effective Floquet lattice Hamiltonians with a non-trivial topological band structure. While previous implementations relied on the physical motion of the lattice potential, this effect can also be realized by a periodic modulation of a magnetic field gradient. As the coupling of an atom to this magnetic field gradient depends on its magnetic moment and therefore its internal state, the effective Hamiltonian is spin-dependent.

We realize a state-dependent lattice for fermionic potassium atoms and characterize the different band structures for each internal state by measuring the expansion rate of an atomic cloud in the lattice and the effective mass through dipole oscillations. Furthermore, we study the heating caused by the periodic driving in an interacting fermionic spin mixture and how it can be suppressed. This method of creating spin-dependent optical lattices can be used to create novel situations, such as systems where one fermionic spin state is pinned to the lattice, while the other remains itinerant.

Q 61.2 Fri 11:15 e001

Experimental reconstruction of the Berry curvature in a topological Bloch band — •Nick Fläschner, Benno Rem, Matthias Tarnowski, Dominik Vogel, Dirk-Sören Lühmann, Klaus Sengstock, and Christof Weitenberg — Institut für Laserphysik, Universität Hamburg, Luruper Chaussee 149, 22761 Hamburg, Germany

Topological properties lie at the heart of many fascinating phenomena in solid state systems such as quantum Hall systems or Chern insulators. The topology can be captured by the distribution of Berry curvature, which describes the geometry of the eigenstates across the Brillouin zone. Employing fermionic ultracold atoms in a hexagonal optical lattice, we generate topological bands using resonant driving and show a full momentum-resolved measurement of the ensuing Berry curvature. Our results pave the way to explore intriguing phases of matter with interactions in topological band structures.

Q 61.3 Fri 11:30 e001

Detecting the BCS order parameter in the dephasing of collective oscillations after a sudden ramp of the lattice depth in a honeycomb lattice — •Marlon Nuske[1], Eite Tiesinga[2], and Ludwig Mathey[1] — [1]Zentrum für Optische Quantentechnologien and Institut für Laserphysik, Universität Hamburg, 22761 Hamburg, Germany — [2]Joint Quantum Institute and Center for Quantum Information and Computer Science, National Institute of Standards and Technology and University of Maryland, Gaithersburg, Maryland 20899, USA

We obtain the excact time evolution for a mean-field Bardeen-Cooper-Schrieffer (BCS) state after a sudden quench to a large lattice depth, where the dynamics is dominated by interactions between atoms. The quench initiates collective oscillations with frequency $U_f/(2\pi)$ of the momentum occupation numbers and imprints a phase oscillating with the same frequency on the order parameter. Finite hopping after the quench leads to dephasing of the different momentum modes and a subsequent damping of the oscillations. Even for finite temperatures this occurs for a mean-field BCS state, but not for a non-interacting Fermi gas. Measuring the dephasing of collective oscillations of occupation numbers may therefore be used as a signature to detect the BCS order parameter Δ. Finally, we investigate the time evolution of the density-density correlations.

Q 61.4 Fri 11:45 e001

Floquet-Boltzmann equation for periodically driven Fermi systems — •Maximilian Genske and Achim Rosch — Institut für Theoretische Physik, Universität zu Köln, D-50937 Cologne, Germany

Periodically driven quantum systems can be used to realize quantum pumps, ratchets, artificial gauge fields and novel topological states of matter. Starting from the Keldysh approach, we develop a formalism, the Floquet-Boltzmann equation, to describe the dynamics and the scattering of quasiparticles in such systems. The theory builds on a separation of time-scales. Rapid, periodic oscillations occurring on a time scale $T_0 = 2\pi/\Omega$, are treated using the Floquet formalism and quasiparticles are defined as eigenstates of a non-interacting Floquet Hamiltonian. The dynamics on much longer time scales, however, is modeled by a Boltzmann equation which describes the semiclassical dynamics of the Floquet-quasiparticles and their scattering processes. As the energy is conserved only modulo $\hbar\Omega$, the interacting system heats up in the long-time limit. As a first application of this approach, we compute the heating rate for a cold-atom system, where a periodical shaking of the lattice was used to realize the Haldane model [G. Jotzu *et al.*, Nature **515**, 237 (2014)].

Q 61.5 Fri 12:00 e001

Dynamics of Trapped Dipolar Fermi Gases: From Collisionless to Hydrodynamic Regime — •Vladimir Veljić[1], Antun Balaž[1], and Axel Pelster[2] — [1]Scientific Computing Laboratory, Institute of Physics Belgrade, University of Belgrade, Serbia — [2]Physics Department and Research Center OPTIMAS, Technical UIniversity of Kaiserslautern, Germany

A recent time-of-flight expansion experiment has now unambiguously detected a Fermi surface deformation in a dipolar quantum gas of fermionic erbium atoms in the collisionless regime [1]. Here we follow Ref. [2] and perform a systematic study of a time-of-flight expansion for trapped dipolar Fermi gases ranging from the collisionless to the hydrodynamic regime at zero temperature. To this end we solve analytically the underlying Boltzmann-Vlasov equation in the vicinity of equilibrium by using a suitable rescaling of the equilibrium distribution [3], where the collision integral is simplified within a relaxation time approximation. We also analyze the quench dynamics, which is induced by a sudden rotation of the polarization of the atomic magnetic moments and show that it can be understood in terms of a superposition of the low-lying collective modes. All presented analytical and numerical calculations are relevant for understanding quantitatively ongoing experiments with ultracold fermionic dipolar atoms.

[1] K. Aikawa, et al., Science **345**, 1484 (2014).
[2] F. Wächtler, A. R. P. Lima, and A. Pelster, `arXiv:1311.5100`.
[3] P. Pedri, D. Guery-Odelin, and S. Stringari, Phys. Rev. A **68**, 043608 (2003).

Q 61.6 Fri 12:15 e001

Emergence of orthogonality in the Fermi impurity problem — •Andrea Bergschneider, Michael Dehabe, Jan Hendrik Becher, Vincent M. Klinkhamer, Simon Murmann, Gerhard Zürn, and Selim Jochim — Physikalisches Institut der Universität Heidelberg, Im Neuenheimer Feld 226, 69120 Heidelberg, Germany

In quasi-one-dimensional systems, the ground-state wave function of an impurity particle interacting with a Fermi sea is orthogonal to the wave function of the non-interacting system. In this case the squared overlap between the interacting and the non-interacting systems, which is defined as the quasiparticle residue, is zero.

Here, we report on measurements of the residue of a single fermionic impurity particle interacting with an increasing number of majority particles. To probe the system, we flip the spin of the impurity particle by driving a radio frequency (RF) transition. In a previous experiment we used RF spectroscopy to measure the interaction energy in this system while increasing the number of majority particles one atom at a time and thereby observed the crossover from few to many-body physics [1]. Now, we measure how the wave function overlap between initial and final states changes both as a function of interaction strength and the number of majority particles. Our goal is to extend these measurements into the crossover region between few and many-body physics by increasing the number of majority particles and thereby observe the emergence of the orthogonality catastrophe.

[1] Wenz et al. Science 342, 457 (2013)

Q 61.7 Fri 12:30 e001

Many-body localization in the presence of photon scattering — •Henrik Lueschen[1,2], Pranjal Bordia[1,2], Sean

The 19th Symposium on Condensed Matter Physics - SFKM 2015, Belgrade - Serbia
Poster: 25

Collective Modes of Dipolar Fermi Gas from Collisionless to Hydrodynamic Regime

Vladimir Veljić[a], Antun Balaž[a] and Axel Pelster[b]

[a]*Scientific Computing Laboratory, Institute of Physics Belgrade, University of Belgrade, Pregrevica 118, 11080 Belgrade, Serbia*
[b]*Department of Physics and Research Center OPTIMAS, Technical University of Kaiserslautern, Erwin-Schrödinger Straße, Gebäude 46, 67663 Kaiserslautern, Germany*

Abstract. We study the low-lying collective excitations of a Fermi gas at zero temperature confined to a triaxial harmonic trap, featuring the anisotropic long-range dipole-dipole interaction. In order to analyze the collective modes of this system, we follow Ref. [1] and solve analytically the underlying Boltzmann-Vlasov equation by using the relaxation-time approximation and by performing a suitable rescaling of the equilibrium distribution [2]. The resulting ordinary differential equations for the dynamics of the scaling parameters are linearized around equilibrium in order to determine both eigenvectors and eigenfrequencies of the collective modes. Due to the smallness of the dipolar interaction strength, the collisionless regime corresponds to the case of a noninteracting Fermi gas, i.e., the three low-lying modes represent one-dimensional cloud elongations along only one of the respective trap directions [3, 4]. In contrast to that, we get in the hydrodynamic regime the usual breathing, quadrupole, and radial quadrupole mode, where the cloud elongations are truly three- and two-dimensional, respectivley [5, 6]. We investigate in detail how the eigenvectors change when decreasing the relaxation time all the way from the collisionless to the hydrodynamic regime. We also analyze the quench dynamics, which is induced by a sudden rotation of the polarization of the atomic magnetic moments by 90°, and show that it can be understood by a superposition of the low-lying collective modes. These analytical and numerical calculations are relevant for understanding quantitatively the current Innsbruck experiment with ultracold fermionic erbium atoms, which interact via their magnetic dipole moments [7].

REFERENCES

1. F. Wächtler, A. R. P. Lima, and A. Pelster, arXiv:1311.5100 (2013).
2. P. Pedri, D. Guery-Odelin, and S. Stringari, *Phys. Rev. A* **68**, 043608 (2003).
3. T. Sogo, L. He, T. Miyakawa, S. Yi, H. Lu, and H. Pu, *New J. Phys.* **11**, 055017 (2009).
4. J.-N. Zhang, R.-Z. Qiu, L. He, and S. Yi, *Phys. Rev. A* **83**, 053628 (2011).
5. A. R. P. Lima and A. Pelster, *Phys. Rev. A* **84**, 041604(R) (2011).
6. A. R. P. Lima and A. Pelster, *Phys. Rev. A* **86**, 063609 (2012).
7. K. Aikawa, S. Baier, A. Frisch, M. Mark, C. Ravensbergen, and F. Ferlaino, *Science* **345**, 1484 (2014).

Quench Dynamics for Trapped Dipolar Fermi Gases

V. Veljić[1], A. Balaž[1] and A. Pelster[2]
[1]*Scientific Computing Laboratory, Institute of Physics Belgrade, University of Belgrade, Pregrevica 118, 11080 Belgrade, Serbia*
[2]*Physics Department and Research center OPTIMAS, Technical University of Kaiserslautern, 67663 Kaiserslautern, Germany*
e-mail: vveljic@ipb.ac.rs

A recent time-of-flight expansion experiment for polarized fermionic erbium atoms managed to detect a Fermi surface deformation which is due to the dipolar interaction [1]. Here we perform a systematic study of quench dynamics of trapped dipolar Fermi gases at zero temperature, which are induced by a sudden change of the magnetic field, which enforces the polarization of the magnetic moments of the erbium atoms. As this modifies the equilibrium configuration, oscillations of the fermionic erbium cloud emerge around the new equilibrium, which are characteristic for the presence of the dipole-dipole interaction. In order to analyze the emergent dynamics we follow Ref. [2] and solve analytically the underlying Boltzmann-Vlasov equation wihtin the relaxation approximation in the vicinity of the new equilibrium configuration by using a suitable rescaling of the equilibrium distribution [3]. The resulting ordinary differential equations of motion for the scaling parameters are solved numerically for experimentally relevant parameters all the way from the collisionless to the hydrodynamic regime. A comparison with a corresponding linear stability analysis reveals that the resulting quench dynamics can be understood in terms of the low-lying collective modes due to the smallness of the dipolar interaction strength. All our theoretical and numerical calculations can be tested in current experiments with ultracold dipolar fermionic atoms.

REFERENCES
[1] K. Aikawa et al., Science 345, 1484 (2014).
[2] F. Wächtler, A. R. P. Lima, A. Pelster, arXiv: 1311.5100 (2013).
[3] P. Pedri, D. Guery-Odelin, S. Stringari, Phys. Rev. A 68, 043608 (2003).

Trapped Bose-Einstein Condensates with Strong Disorder

V. Lončar[1], A. Balaž[1] and A. Pelster[2]
[1]*Scientific Computing Laboratory, Institute of Physics Belgrade, University of Belgrade, Pregrevica 118, 11080 Belgrade, Serbia*
[2]*Physics Department and Research center OPTIMAS, Technical University of Kaiserslautern, 67663 Kaiserslautern, Germany*
e-mail: vloncar@ipb.ac.rs

We work out a non-perturbative approach towards the dirty boson problem at zero temperature that is based on a Gaussian approximation for correlation functions of the disorder problem and the condensate wave function solving the Gross-Pitaevskii problem. For harmonically trapped Bose-Einstein condensates we apply, in addition, the

density of these defects lead to a characteristic exponential momentum distribution as well as stability of the condensate towards exterior pertubations. Experimental and numerical results are compared to analytical predictions drawn from our model of randomly distributed defects. Complete thermalization of the system is observed through measurements of the momentum distribution, exhibiting a transition from the random defect to a modifed Yang-Yang model.

Q 15.36 Mon 17:00 C/Foyer

Universal dynamics and non-thermal fixed points in spinor Bose-Einstein condensates — •Anselm Klenner[1,2,3], Markus Karl[1,2,3], and Thomas Gasenzer[1,2,3] — [1]Kirchhoff-Institut für Physik, Ruprecht-Karls-Universität Heidelberg, Im Neuenheimer Feld 227, 69120 Heidelberg, Germany — [2]Institut für Theoretische Physik, Ruprecht-Karls-Universität Heidelberg, Philosophenweg 16, 69120 Heidelberg, Germany — [3]ExtreMe Matter Institute EMMI, GSI Helmholtzzentrum für Schwerionenforschung GmbH, Planckstraße 1, 64291 Darmstadt, Germany

Using numerical simulations we investigate second order phase transitions of spin-1 spinor Bose-Einstein condensates. For the simulations we use the truncated Wigner method which is a statistical approach and uses classical field equations. The spinor condensates provide us with a rich variety of phases and topological defects such as domain walls, spin textures and spin vortices. The types of defects which are created depend on the properties of the critical point. In these simulations we can reach states with quasi-stationary, non-equilibrium momentum distributions, which indicate the vicinity of a non-thermal fixed point. Spinor Bose gases provide ideal means to study such universal critical dynamics far from equilibrium, which is expected to be relevant for a wide range of phenomena far beyond ultracold gases.

Q 15.37 Mon 17:00 C/Foyer

Dynamical universal properties of one-dimensional split condensates — •Sebastian Erne[1,2,4], Valentin Kasper[1], Jürgen Berges[1], Thomas Gasenzer[1,2,3], and Jörg Schmiedmayer[4] — [1]Institut für Theoretische Physik, Ruprecht-Karls-Universität Heidelberg, Philosophenweg 16, 69120 Heidelberg, Germany — [2]ExtreMe Matter Institute EMMI, GSI Helmholtzzentrum für Schwerionenforschung GmbH, Planckstraße 1, 64291 Darmstadt, Germany — [3]Kirchhoff-Institut für Physik, INF 227, 69120 Heidelberg, Germany — [4]Vienna Center for Quantum Science and Technology (VCQ), Atominstitut, TU Wien, Vienna, Austria

The recent measurement of higher-order phase correlation functions enables a precise examination of non-Gaussian correlations in the relative phase of two one-dimensional quasicondensates. This shows the necessity of refined non-pertubative theoretical descriptions of split condensates. For these systems the early time evolution of squeezed states is well described by a quadratic theory. In this work we investigate how the linear coupling between two one-dimensional Bose gases controls the non-Gaussian contributions. The subsequent quench of this control parameter can proceed in two directions: Increasing or decreasing the non-gaussianity of the systems as compared to the initial state. Finally we report on universal properties of the dynamics of higher-order correlation functions.

Q 15.38 Mon 17:00 C/Foyer

Nonthermal fixed points and superfluid turbulence in 2D ultracold Bose gases — •Fabian Brock[1,2], Simon Sailer[1,2], Markus Karls[1,2], and Thomas Gasenzer[1,2] — [1]Kirchhoff-Institut für Physik, Im Neuenheimer Feld 227, 69120 Heidelberg — [2]Institut für Theoretische Physik, Ruprecht-Karls-Universität Heidelberg, Philosophenweg 16, 69120 Heidelberg

The behavior of turbulent one-component Bose-Einstein condensates is studied by simulations of the driven-dissipative Gross-Pitaevskii equation and free expansion dynamics. The aspect ratio during free expansion is studied using the GPE and a hydrodynamic model based on Eulers equations. By comparison to non-turbulent systems, this gives insight into the influence of vorticity on the expansion dynamics. The results aim to help the study of superfluid turbulence in experiment by measuring the gas after some given expansion time and drawing inferences on its initial state. In the driven-dissipative case, non-thermal fixed points far away from equilibrium are studied. Power laws in the occupation number are numerically determined by vortex statistics and compared to analytical results.

Q 15.39 Mon 17:00 C/Foyer

Towards a degenerate quasi 2D gas of fermions near the BEC-BCS crossover — •Thomas Paintner, Daniel Hoffmann, Stefan Häusler, Wladimir Schoch, Wolfgang Limmer, Benjamin Deissler, and Johannes Hecker-Denschlag — Universität Ulm, Institut für Quantenmaterie, Deutschland

Here, we present the creation of a two-dimensional gas of ultracold fermions near the BEC-BCS crossover.

We prepared a sample of ultracold ^{6}Li atoms in the lowest two hyperfine states in a strong single beam optical dipole trap. For implementing a quasi 2D degenerate gas we focus a blue detuned TEM_{01} beam on our atoms [1].

To create the TEM_{01}, we illuminate a π-phase plate with a high power laser at 532nm. In the far field a TEM_{01} profile is created. We can change the size of the TEM_{01} mode by changing the laser beam waist. Strong enough confinement of the atoms in the TEM_{01} laser field will freeze out the atomic motion in this direction, leading to a quasi 2D gas.

Reducing the dimension of the system is another major step towards the realization of an all optical 2D honeycomb lattice.

[1] Opt.Express 13, 2843-2851 (2005)

Q 15.40 Mon 17:00 C/Foyer

Time-of-Flight Expansion for Trapped Dipolar Fermi Gases: From Collisionless to Hydrodynamic Regime — •Vladimir Veljić[1], Antun Balaž[1], and Axel Pelster[2] — [1]Scientific Computing Laboratory, Institute of Physics Belgrade, University of Belgrade, Serbia — [2]Physics Department and Research Center OPTIMAS, Technical University of Kaiserslautern, Germany

Some time ago it was predicted that the momentum distribution of a Fermi gas is deformed from spherical to cyclindrical provided a dipole-dipole interaction is present. A recent time-of-flight (TOF) expansion experiment has now unambiguously detected such a Fermi surface deformation in a dipolar quantum gas of fermionic erbium atoms in the collisionless regime [1]. Here we follow Ref. [2] and perform a systematic study of TOF expansions for trapped dipolar Fermi gases ranging from the collisionless to the hydrodynamic regime at zero temperature. To this end we solve analytically the underlying Boltzmann-Vlasov equation in the vicinity of equilibrium by using a suitable rescaling of the equilibrium distribution, where the collision integral is simplified within a relaxation-time approximation. The resulting ordinary differential equations for the scaling parameters are then solved numerically for experimentally realistic parameters for increasing relaxation times. Our analysis is, thus, useful for future TOF experiments in order to determine the value of the underlying relaxation time from expansion data.

[1] K. Aikawa et al., Science **345**, 1484 (2014)

[2] F. Wächtler, A. R. P. Lima, and A. Pelster, `arXiv:1311.5100`

Q 15.41 Mon 17:00 C/Foyer

Bogoliubov Theory of Dipolar Bose Gas in Weak Random Potential — •Mahmoud Ghabour[1] and Axel Pelster[2] — [1]Physics Department, Freie Universität Berlin, Germany — [2]Physics Department and Research Center OPTIMAS, Technische Universität Kaiserslautern, Germany

We consider a dilute homogeneous Bose gas with both an isotropic short-range contact interaction and an anisotropic long-range dipole-dipole interaction in a weak random potential at low temperature in three dimensions. Within the realm of Bogoliubov theory we analyze how both condensate and superfluid density are depleted due to quantum and thermal fluctuations as well as disorder fluctuations. Afterwards, we calculate with this the resulting velocities of first and second sound within an anisotropic extension of the Landau-Khalatinikov two-fluid model.

[1] K. Huang and H. F. Meng, Phys. Rev. Lett. **69**, 644 (1992)

[2] C. Krumnow and A. Pelster, Phys. Rev. A **84**, 021608(R) (2011)

[3] B. Nikolic, A. Balaz, and A. Pelster, Phys. Rev. A **88**, 013624 (2013)

[4] M. Ghabour and A. Pelster, `arXiv:1410.3070`

Q 15.42 Mon 17:00 C/Foyer

Analytical and Numerical Study of Bose-Einstein Condensate with Localized Impurity — •Javed Akram[1] and Axel Pelster[2] — [1]Physics Department, Freie Universität Berlin Germany — [2]Physics Department and Research Center OPTIMAS, Technische Universität Kaiserslautern Germany

Motivated by the recent experimental work of Refs. [1, 2], we investigate a localized ^{133}Cs impurity in the center of a trapped ^{87}Rb

Bose Gases Tu-009

ZNG – Theory for Dipolar Quantum Gases

Vladimir Veljić[1], Antun Balaž[1], Axel Pelster[2]

1. *Scientific Computing Laboratory, Institute of Physics Belgrade, University of Belgrade, Serbia*
2. *Department of Physics and Research Center Optimas, Technical University of Kaiserslautern, Germany*

We study harmonically trapped three-dimensional ultracold Bose and Fermi gases in the presence of the short-range isotropic contact and the long-range anisotropic dipole-dipole interaction (DDI). The Hartree-Fock mean-field dynamics of such quantum systems can be described within the framework of the Zaremba-Nikuni-Griffin (ZNG) theory. Usually, the underlying Boltzmann-Vlasov (BV) equation is solved by the relaxation-time approximation for the collision integral, where the relaxation time is treated as a phenomenological parameter. We develop a formalism to determine the relaxation time microscopically for ultracold quantum gases at finite temperature, which allows us to include collision effects self-consistently in the BV formalism.

Bose Gases Tu-010

Dynamics of spinor condensates in a microwave dressing field

Lichao Zhao[1], Jie Jiang[1], Tao Tang[1], Micah Webb[1], Yingmei Liu[1]

1. *Department of Physics, Oklahoma State University*

We experimentally study dynamics in a sodium antiferromagnetic spinor condensate as a result of spin-dependent interactions c and microwave dressing field interactions characterized by the net quadratic Zeeman effect q_{net}. In contrast to magnetic fields, microwave dressing fields enable us to access both negative and positive values of q_{net}. We find an experimental signature to determine the sign of q_{net}, and observe harmonic spin population oscillations at every q_{net} except near each separatrix in phase space where spin oscillation period diverges. Our data in the negative q_{net} region exactly resembles what is predicted to occur in a ferromagnetic spinor condensate in the positive q_{net} region. This observation agrees with an important prediction derived from the mean-field theory: spin dynamics in spin-1 condensates substantially depends on the sign of q_{net}/c. This work may be the first to use only one atomic species to reveal mean-field spin dynamics, especially the remarkably different relationship between each separatrix and the magnetization, of spin-1 antiferromagnetic and ferromagnetic spinor condensates.

Република Србија
Универзитет у Београду
Физички факултет
Д.Бр.2013/8003
Датум: 29.10.2018. године

На основу члана 161 Закона о општем управном поступку и службене евиденције издаје се

УВЕРЕЊЕ

Вељић (Радиша) Владимир, бр. индекса 2013/8003, рођен 30.12.1987. године, Брус, Република Србија, уписан школске 2018/2019. године, у статусу: самофинансирање; тип студија: докторске академске студије; студијски програм: Физика.

Према Статуту факултета студије трају (број година): три.
Рок за завршетак студија: у двоструком трајању студија.

Ово се уверење може употребити за регулисање војне обавезе, издавање визе, права на дечији додатак, породичне пензије, инвалидског додатка, добијања здравствене књижице, легитимације за повлашћену вожњу и стипендије.

Овлашћено лице факултета

УНИВЕРЗИТЕТ У БЕОГРАДУ

Адреса: Студентски трг 1, 11000 Београд, Република Србија
Тел.: 011 3207400; Факс: 011 2638818; E-mail: officebu@rect.bg.ac.rs

ВЕЋЕ НАУЧНИХ ОБЛАСТИ ПРИРОДНО-МАТЕМАТИЧКИХ НАУКА

Београд, 5.2.2018.
02-04 Број 61206-39/2-18
СЋ

На основу чл. 148. Закона о високом образовању (“Службени гласник РС“, број 88/17) , члана 47. став 5. тачка. 3. Статута Универзитета у Београду ("Гласник Универзитета у Београду", број 186/15-пречишћени текст и 189/16) и чл. 14. – 21. Правилника о већима научних области на Универзитету у Београду (“Гласник Универзитета у Београду”, број 134/07, 150/09, 158/11, 164/11 и 165/11, 180/14, 195/16, 196/16 и 197/17), а на захтев Физичког факултета, број: 626/4 од 20.12.2017. године, Веће научних области природно-математичких наука, на седници одржаној 5.2.2018. године, донело је

О Д Л У К У

ДАЈЕ СЕ САГЛАСНОСТ на предлог теме докторске дисертације ВЛАДИМИРА ВЕЉИЋА, под називом: " Quantum kinetic theory for ultracold dipolar fermi gases" (Квантна кинетичка теорија за ултрахладне диполне Ферми гасове)".

ПРЕДСЕДНИК ВЕЋА

Проф. др Воја Радовановић

Доставити:
- Факултету
- архиви Универзитета